LBNL-39388
UC-413
Preprint

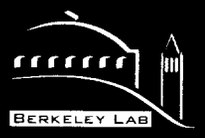

ERNEST ORLANDO LAWRENCE
BERKELEY NATIONAL LABORATORY

Reducibility and Thermal Scaling in Nuclear Multifragmentation

L.G. Moretto, R. Ghetti, L. Phair, K. Tso,
and G.J. Wozniak
Nuclear Science Division

September 1996
Submitted to
Physics Reports

LBNL-39388
UC-413

Reducibility and Thermal Scaling in Nuclear Multifragmentation

L.G. Moretto, R. Ghetti, L. Phair,
K. Tso, and G.J. Wozniak

Nuclear Science Division
Ernest Orlando Lawrence Berkeley National Laboratory
University of California
Berkeley, California 94720

September 1996

This work was supported in part by the Director, Office of Energy Research, Office of High Energy and Nuclear Physics, Nuclear Physics Division, of the U.S. Department of Energy under Contract No. DE-AC03-76SF00098, and the National Science Foundation under Grant Nos. PHY-8913815, PHY-90117077, and PHY-9214992.

Reducibility and Thermal Scaling in Nuclear Multifragmentation

L.G. Moretto, R. Ghetti, L. Phair, K. Tso, and G.J. Wozniak

Nuclear Science Division, Lawrence Berkeley National Laboratory, Berkeley, CA 94720

Abstract

Recent studies have revealed the existence of a number of reducibility and thermal scaling properties in nuclear multifragmentation. The probability of emitting n-fragments is found to be *reducible* to the probability of emitting a single fragment through the binomial expression. The resulting one fragment probability shows *thermal scaling* by producing linear Arrhenius plots.

Similarly, the charge distributions associated with n-fragment emission are *reducible* to the one-fragment charge distribution. *Thermal scaling* is also observed. The reducibility equation contains a constant whose value, zero or positive, can be related to a univariant (two phases) or bivariant (one phase) regime.

The light fragment particle-particle angular correlations also show *reducibility* to the single-particle angular distributions as well as *thermal scaling*. A mass scaling associated with the angular correlations suggests emission from several small sources ($A \approx 20$).

The limits of applicability of scaling and reducibility are discussed as well as their implications for the mechanism of multifragmentation.

Contents

Preprint submitted to Elsevier Science *3 September 1996*

1 Preface

This work is not a review of multifragmentation. With this apotropaic statement we direct the interested reader to more proper reviews and articles [1–5]. This is a story of the research on multifragmentation that took place in our group over the last couple of years. It is summarily prefaced by previous relevant work, which sets the stage for the new; it is accompanied by occasional forays into allied directions; but, by and large, it is a rather focused description of our attempt to make sense of a very chaotic and forbidding process.

What came out of this effort should not be taken as definitive: it is not so even in our eyes. Possibly of some interest to the reader is the approach that we have taken. Confronted with the tangled thicket of the experimental evidence, we have refrained from dealing with it through some all embracing, but also all concealing numerical simulation, whose output risks being more obscure and mystifying than the process itself. Instead we have chosen to stand back and contemplate the phenomenon, searching for hidden simplicities and sparks of understanding.

Kindly, Nature has obliged, and has let us glimpse clear signals of thermal behavior. More fascinatingly, she has shown us how the complexity of multifragment production could be reduced to the simplicity of single fragment emission. These two aspects, which make up the title of this paper, allow for a natural and beautiful connection to the simpler and more solidly established physics at lower energy.

The story that follows was told by one of us to a dear friend, Rolf Siemssen, during a long evening in Beijing, when nothing seemed better than the joy of telling and the eagerness of listening.

To Rolf, who encouraged us to write the story just as he heard it, and who triggered the invitation for this article, we gratefully dedicate this work.

2 Prologue

Multifragmentation, which occurs at the extreme limit of nuclear stability, attests to the twilight of nuclei, and perhaps of nuclear physics as well. In the decades gone by, more respectful, but no less capable hands than ours, teased out of nuclei their hidden harmonies. With a keenness that would have met with Plato's approval, the symmetries embodied in nuclei were brought to light in the regularities of shell model structures and of collective motion. With a savvy worthy of Roman architects and engineers, nuclei were sectioned and rebuilt, and with alchemical fervor heated and distilled.

But the dark side of our nature could not be prevented from bashing nuclei and nuclear physics with barbarian relish. Now that the barbarians have gone in search of new empires to conquer and new beauty to smash, we are left with the dust and smoke of what once was Nuclear Physics, and with the many little pieces of mindlessly shattered nuclei.

A eulogy would seem to be in order. And if we would not presume to lament the lofty death of Nuclear Physics, in the possibly vain hope of a belated resurrection, we can at least celebrate the fall (to pieces) of nuclei, and show the beauty that attends their demise.

In truth, there was a somewhat ghoulish expectation on the theorists' part, that nuclei would fall apart, undermined by instabilities brought about either by a compression-rarefaction sequence or by their stretching into cylinders, disks, doughnuts or even bubbles.

But nuclei chose for their demise a beauty all their own, and left us with the job of discovering it. This is the story of that discovery.

2.1 The Category of Multifragmentation

Faced with the task of studying multifragmentation in nuclei, one may be led to question the relevance of this sort of endeavor. Is it just a matter of sweeping the pieces away as valueless remnants of a worthy construct, or is there in the mess of pieces anything of comparable worth as the original artifact? If we would hesitate to shatter a Ming vase, at some stage of our maturation we certainly have relished occasionally the shattering of less worthy objects, and may even have been puzzled by the variable number and broad range of pieces that ensued.

This clastic activity has recently been ennobled by its appearance in top physics journals [6], leading one to wonder whether this shattering fashion has any more to do with intellectual pursuits than with frustration at ever-declining research budgets.

What can be interesting in the way an object fragments? A partial answer is in the order that often is found imbedded into the disorder of the ensuing pieces. Another is the obvious applicative relevance of the size distributions of the pieces. Polymer degradation [7], size distributions in a mill's output [8], shrapnel sizes in shell fragmentation, crumbling of asteroids under mutual impact [9], etc., provide a wonderful laundry list for an interdisciplinary conference.

Yet, general as such a phenomenon may appear, it certainly details itself into a variety of media and processes. So, an attempt to characterize it seems here in order.

A simple classification in terms of media structure may be useful. So we may speak of

continuous multifragmentation when the underlying unit of the medium (microscopic or not) is not of the essence. This may be the case of fragile bodies shattering [10] through impact like dropped glass panes, or the breaking up of fluids under the effect of a variety (volume, surface) of instabilities, such as spinodal phase separations [11], or the falling apart of a column of liquid (Rayleigh instabilities [12]) or of a thin sheet of liquid (sheet instabilities) [13]. Similarly, we may speak of *discrete* multifragmentation when the underlying unit is of the essence. Examples of this are the degradation of chains and multidimensional lattices, like one, two or three dimensional polymers [7]. An additional classification may be made in terms of dimensionality. While it is obvious that dimensionality may play a role in the clusterization of discrete systems (one bond broken is sufficient to produce fragments in one dimension but not in two or three), it seems to also play a role in continuous media. The size distributions in the shattering of a clay plate contain two power law dependences – one for larger fragments (two dimensions) and another for small fragments (three dimensions) [6].

But above all, the primary mechanism of multifragmentation may be of interest. The process can be dynamical like the shattering of glass and the fragmentation of shells, or statistical like the clusterization of a fluid near the critical point. The mechanism could as well be labelled statistical, though not in terms of equilibrium distributions, but in that the rate of emission is a sequential statistical production of (molecular) aggregates from an emitting body. Within this framework it becomes important to distinguish between the thermal or statistical nature of the elementary process and the constraints imposed by geometrical or dimensional aspects or by conservation laws.

Where does nuclear multifragmentation fall within this scheme? Conventional nuclear reactions involve typically two pieces in the exit channel. In some cases the fragmentation is dynamical, like in direct reactions. In others, it is statistical. In the latter case, more than two pieces can often result from the well understood sequential emission of nucleons or little clusters like α particles. Low energy fission and complex fragments emission are well documented cases of statistical binary decay [14]. The increase in excitation energy leads naturally to the further decay of the original binary fragments, giving rise to sequential binary multifragmentation. While the documentation of this generalized process is at hand in some cases [3,14], what goes on in full fledged multifragmentation is still under heavy debate (see references [1–5] and references therein). The issues of dynamics versus statistics, and, if statistics, sequential versus simultaneous, are delightful and invigorating, engaging all practitioners of the field. A variety of ideas has come from the very diverse fields in which multifragmentation of one sort or another occurs. We do not know yet how common or unique nuclear multifragmentation may be. In what follows we have endeavored to describe very general aspects of reducibility and thermal scaling, which seem to work well in nuclear multifragmentation and which may well apply to other processes of multifragmentation. In the hope that this subject may draw the attention of non-nuclear scientists, we have tried to make this paper easy (if not clear) reading, at least in the first part. The tedium of necessary technical details is relegated to the second part, for the experts'

use.

Part A

3 Brief Discourse on the Method

Confronted with the ever-changing singularities of world phenomena, we tend to allay the resulting existential anxiety by reducing these phenomena to something already known, or at least better known. The cry "eureka" of understanding is often a cry of relief for one less threatening mystery, rather than exuberant joy of discovery. Be that as it may, there are two golden ways to understanding.

The first is truly a royal way: it is called apodictic, or a priori. Leibnitz, a mathematician as well as a philosopher, dreamed of applying mathematical rigor to logic, so that two philosophers confronted with a disagreement would say to each other: "Calculemus." Let us calculate.

This works wonderfully for the understanding of "simple" systems. Often nothing more than calculation is needed to explain the machinery of the sky in terms of gravity, or atomic spectra in terms of quantum mechanics.

Complex systems, however, are altogether another matter. For instance, a QED computer that behaves like a dog does not give us the comfort of understanding dog behavior.

Nuclear physics is somewhere in between the two extremes of simple and complex systems. Nobody denies the usefulness of "ab initio" calculations in nuclear physics. However, much progress has been made by identifying qualitative structures, such as mean fields, compound nuclei, transition states, etc., related to the "emergent" properties of complex systems, which would be "invisible" to the eye of an a priori calculation.

Another way is then to be looked for. We may call it heuristic, or inferential. It does not have rigorous rules like the apodictic way, and it may end up being anecdotal, qualitative, and at times, possibly misleading. Nevertheless, it is ideally suited to many situations, and, on top of that, it is quite exciting.

It works more or less like this. Suppose one has some expectation that the system might behave in a certain way. This behavior could then be searched for in the data themselves, by, for instance, plotting the data in a particularly revealing way. The signature, if it reveals itself, may provide us with a qualitative answer, without relying on models or simulations. For instance, as we shall see later on, we could identify a

signature telling us that the system is behaving thermally, without applying any specific quantitative knowledge in the investigation.

Similarly, suppose we expect a set of degrees of freedom to play an important role. We may then compare a least biased distribution in these variables with the corresponding experimental distribution. If we are lucky we may find that: a) the system behaves according to our expectation; or b) the experimental distributions "surprise" us by manifesting a "dynamical" constraint. In the former case, all is fine; in the latter, things are even better, because we have distilled much of the interesting physics into the dynamical constraint.

Many examples of this will follow, such as probabilities that combine according to a binomial rather than a Poissonian distribution; charge distributions that are, or are not, constrained by charge conservation; and angular correlations that are "almost", but not quite, arising from the folding of uncorrelated angular distributions. A "leitmotif" of our approach is the search for reducibility on the one hand, and thermal scaling on the other. We believe that this search has carried us far, further than we had reason to expect from the inherently noisy process under study.

Realistically, our conclusions are provisional at best, and possibly wrong at worst. More quantitative approaches are definitely in order. Nevertheless this approach has led us to identify the symmetries and regularities embodied in multifragmentation, and let us wonder about further hidden beauties.

4 Evidence for the Reducible and Statistical Nature of Multifragmentation Emission Probabilities

4.1 Decoupling of entrance and exit channel in compound nucleus decay and the role of phase space in the exit channel

In "low energy" nuclear physics, the words "statistical decay" and "compound nucleus" are uttered almost in a single breath. Compound nucleus reactions are characterized and defined by two aspects:

1) The entrance and exit channels are decoupled.

2) The decay probabilities are proportional to a suitably defined exit channel phase space.

The cross section for a given exit channel a can then be written as:

$$\sigma_a = \sigma_0 P_a \tag{1}$$

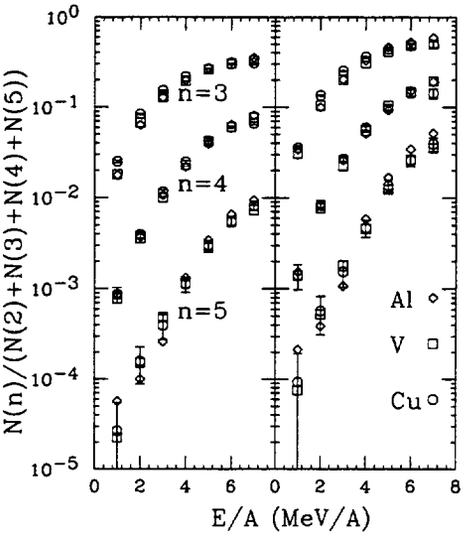

Fig. 1. (left) Uncorrected relative probabilities for the ternary, quaternary, and quinary decays as a function of the source excitation energy for the 60 MeV/nucleon ^{197}Au+^{27}Al, ^{51}V, and ^{nat}Cu reactions [15]. (right) Efficiency corrected relative probabilities. Statistical errors are shown for the Cu target when they exceed the size of the symbols.

where the quantity σ_0 is the entrance channel compound nucleus formation cross section, equal for all the possible exit channels, while P_a is the relative decay probability of the channel a, which is of the form:

$$P_a = \frac{\Gamma_a}{\sum_{a'} \Gamma_{a'}} \tag{2}$$

where $\Gamma_{a'}$ are the decay widths associated with the various exit channels. The essential feature of a statistical decay width is the proportionality of each of the decay widths to its exit channel phase space:

$$\Gamma_a \propto \rho_a. \tag{3}$$

For instance, in fission:

$$\Gamma_f = \frac{T}{2\pi\rho(E)} \rho_s(E - B_f) \tag{4}$$

where $\rho(E)$ is the compound nucleus level density at an excitation energy E, $\rho_s(E - B_f)$ is the saddle point level density, B_f is the fission barrier and T is the saddle point temperature.

The product form of Eq. (1) expresses the decoupling, while the proportionality $P_a \propto \rho_a$ represents the statistical aspect. Notice that σ_0 need not be the "complete fusion" cross section. It may be the "incomplete fusion" cross section as well. It is in fact the cross section for the formation of what we may call the statistically decaying *intermediate source.*

4.2 Evidence for decoupling in multifragmentation

In multifragmentation reactions there is ample evidence for the formation of an intermediate source, which decouples the entrance and exit channels. In Fig. 1 the probabilities for the emission of three, four, etc., complex fragments are shown as a function of the excitation energy of the source [15]. A fragment here is defined as any particle with $Z > 5$. The excitation energy is calculated by kinematically reconstructing the parallel velocity of the fast forward-moving source V_s, defined as [16]:

$$V_s = \frac{\sum_i m_i V_i \cos\theta_i}{\sum_i m_i} \tag{5}$$

where m_i, V_i, and θ_i represent the masses, velocities, and polar angles of the intermediate mass fragments (IMFs) emitted in a given event from these reverse kinematics reactions. An estimate of the upper limit of the excitation energy per nucleon (ϵ^*) is given by [17]:

$$\epsilon^* = \frac{E}{A} = \left(\frac{E}{A}\right)_{\text{beam}} \left(1 - \frac{V_s}{V_{\text{beam}}}\right) \frac{V_s}{V_{\text{beam}}}, \tag{6}$$

where $(E/A)_{\text{beam}}$ and V_{beam} are the energy per nucleon and velocity, respectively, of the beam.

The relative probabilities of Fig. 1 appear to be independent of the target for the same projectile. One can satisfactorily overlap the same "excitation functions" for the reactions Au + Al, V, Cu, (see Fig. 1) provided they are plotted versus the excitation energy determined from the source velocity as shown above [15].

This target independence, or universality, should not be confused with a property of multifragmentation. It is just an example of the decoupling between the entrance channel which leads to the source formation, and the exit channels which result from the source decay. Similar universal features have been observed elsewhere in multifragmentation [17–20]. Like here, they are most likely related to the source formation processes rather than to the source decay.

In the specific cases under consideration in this article, namely in asymmetric heavy ion reactions at energies below 100 MeV/A, the source formation step is incomplete fusion. A schematic picture of the incomplete fusion mechanism is given in Fig. 2. In the example of Fig. 1, the Au projectile picks up a variable amount of mass from the target (the smaller partner appears to always be the donor). For a given amount of mass picked up, there results a source of a *given* mass, momentum, excitation energy and angular momentum.

In this simplified picture, apart from small Q value effects, it does not matter from which target the Au projectile picks up mass. The same amount of mass, picked up

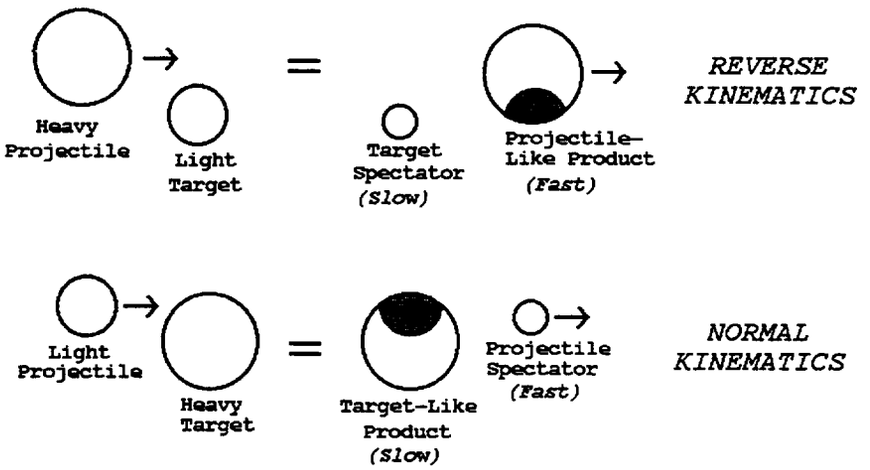

Fig. 2. Schematic illustration of the incomplete fusion model.

from Al, Cu, etc., leads to the formation of the same source, with the same excitation energy. This source then proceeds to decay.

4.3 Thermal scaling in compound nucleus decay

The decoupling between entrance and exit channels is a necessary, but not sufficient, condition for statistical decay. The test for statistical decay must hinge on the proportionality of the decay probability to the level density. At this stage we would like to verify this feature *not* through the use of complex and possibly obscure evaporation codes but rather through a suitable way of plotting the data, which should reveal it in a direct visual way. We illustrate this point with a few low energy examples.

The fission cross section can be written as:

$$\sigma_f = \sigma_0 \frac{\Gamma_f}{\Gamma_T}, \tag{7}$$

where

$$\Gamma_f = \frac{T\rho_s(E - B_f - E_r^s)}{2\pi\rho(E - E_r^{gs})}. \tag{8}$$

Γ_f and Γ_T are the fission and total decay widths, ρ_s is the saddle point level density, ρ is the compound nucleus level density, E is the excitation energy of the compound nucleus, and E_r^s and E_r^{gs} are the saddle and ground state rotational energies. For nuclei with $B_f \gg B_n$ (the barrier for neutron emission), $\Gamma_T \approx \Gamma_n$. Eq. (7) can be rewritten as:

$$\Gamma_n \frac{\sigma_f}{\sigma_0} \frac{2\pi\rho(E - E_r^{gs})}{T} = \rho_s(E - B_f - E_r^s) \approx e^{2\sqrt{a_f(E - B_f - E_r^s)}} \tag{9}$$

where we have assumed a rather simplified form of the Fermi gas level density, and therefore:

$$\frac{1}{2\sqrt{a_n}} \ln\left[\Gamma_n \frac{\sigma_f}{\sigma_0} 2\pi \frac{\rho(E - E_r^{gs})}{T}\right] = \frac{\ln R_f}{2\sqrt{a_n}} = \sqrt{\frac{a_f}{a_n}(E - B_f - E_r^s)}. \tag{10}$$

The neutron width can be approximated by:

$$\Gamma_n \approx KT_n^2 \frac{\rho(E - B_n - E_r^{gs})}{2\pi\rho(E - E_r^{gs})}, \tag{11}$$

where B_n is the last neutron binding energy, T_n is the the temperature after neutron emission, and $K = 2m_n R^2 g/\hbar^2$ with spin degeneracy g=2.

For fission excitation functions in the Pb region, strong shell effects make the approximation

$$\rho(E - B_n - E_r^{gs}) \propto e^{2\sqrt{a_n(E - B_n - E_r^{gs})}} \tag{12}$$

a very poor one. However, for excitation energies higher than 15-20 MeV, the level density assumes its asymptotic form [21]:

$$\rho(E - B_n - E_r^{gs}) \propto \exp\left(2\sqrt{a_n(E - B_n - E_r^{gs} - \Delta_{\text{shell}}}\right), \tag{13}$$

where Δ_{shell} is the ground state shell effect of the daughter nucleus after neutron emission. Assuming this asymptotic expression for the level density after neutron emission, the fission excitation functions can be fit with Eq. (7) using Δ_{shell} as a free parameter in the expression for $\Gamma_T \approx \Gamma_n$ [22].

Thus, a plot of the left hand side of Eq. (10) (which can be constructed from measured fission cross sections and known non fission channels (mostly neutron emission)) versus $\sqrt{E - B_f - E_r^s}$ should be linear (actually a 45° line for $a_f = a_n$). That this is so can be seen in Fig. 3, where a large number of fission excitation functions scale exactly to the same straight line. Such a superb scaling extends from the fission barrier up

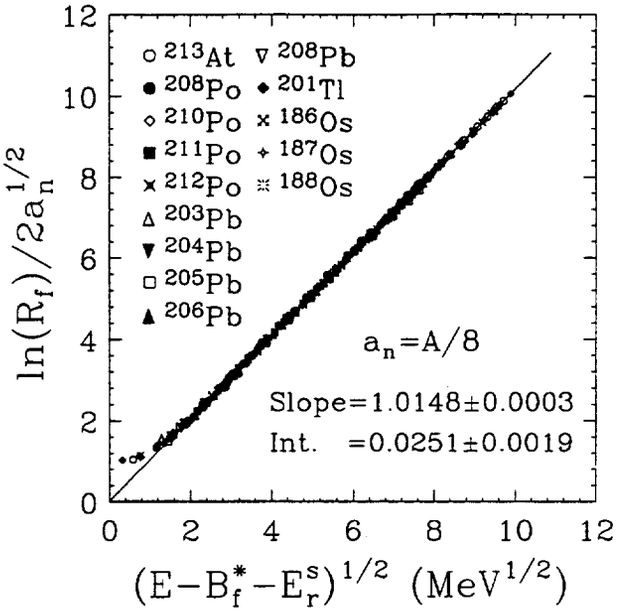

Fig. 3. The quantity $\ln R_f$ divided by $2\sqrt{a_n}$ versus the square root of the intrinsic excitation energy over the saddle for fission of the compound nuclei ^{186,187,188}Os, ^{201}Tl, ^{203,204,205,206,208}Pb, ^{208,210,211,212}Po and ^{213}At [22]. The straight line is a linear fit to all but the lowest two or three data points.

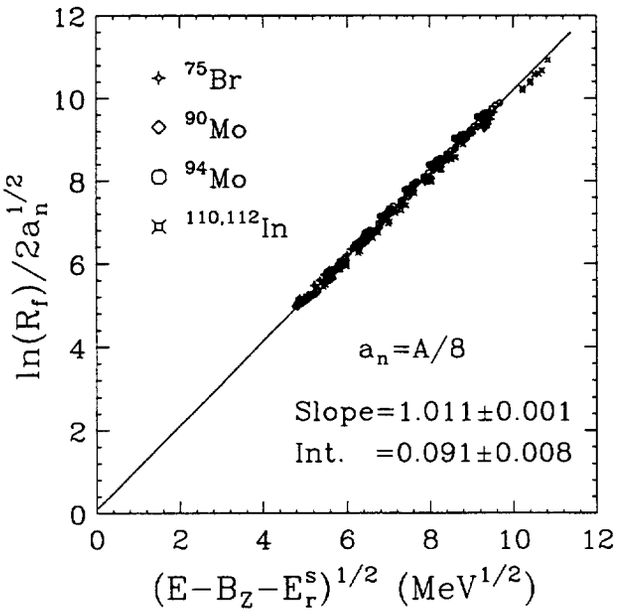

Fig. 4. The logarithm of the reduced complex fragment emission rate R_f divided by $2\sqrt{a_n}$ versus the square root of the intrinsic excitation energy for four compound nuclei: ^{75}Br, ^{90}Mo, ^{94}Mo and ^{110,112}In [23]. The solid line is a linear fit to the data. The error bars are smaller than the size of the symbols.

to more than 140 MeV in excitation energy and leaves little doubt on the statistical nature of the channel, and on the form of the nuclear level density as well.

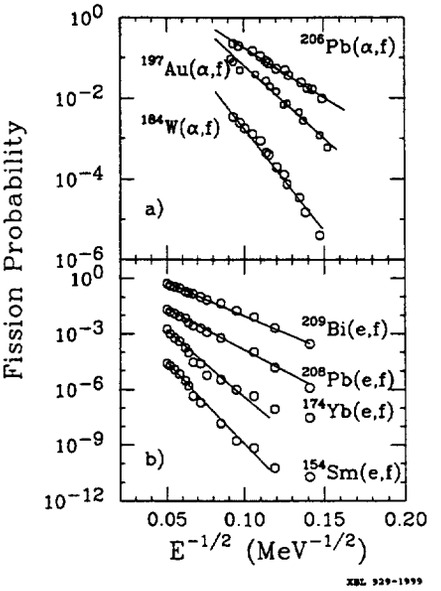

Fig. 5. a) The fission probability plotted as a function of $1/\sqrt{E}$ for the α induced reactions ^{206}Pb(α, f), ^{197}Au(α, f) and ^{184}W(α, f) and b) for the electron induced reactions ^{209}Bi(e, f), ^{208}Pb(e, f), ^{174}Yb(e, f) and ^{154}Sm(e, f). The data are taken from Ref. [24]. The lines are to guide the eye.

The identical scaling holds for the compound nucleus emission of complex fragments. In Fig. 4 a total of 71 excitation functions are shown for the emission of individual fragments with atomic numbers varying from Z=4 to Z=25 from four different compound nuclei [23]. The complete identity of Fig. 3 and Fig. 4 vouches for the total generality of the statistical decay, irrespective of the emitted particle.

4.4 Arrhenius plots

A high energy version of the "thermal" scaling can be readily obtained starting from Eq. (4):

$$\Gamma_f = \frac{T\rho_s(E - B_f)}{2\pi\rho(E)} \approx \frac{T\rho_s(E)}{2\pi\rho(E)} e^{-B_f/T} \sim \frac{T}{2\pi} e^{-B_f/T} \tag{14}$$

where the Boltzmann factor arises as the first order term in the Taylor expansion of $\ln \rho_s(E - B_f)$. Thus,

$$\ln \frac{\Gamma_f}{\Gamma_T} \approx \text{const.} - \frac{(B_f - B_n)}{T} \sim \text{const.} - \frac{b}{\sqrt{E}}, \tag{15}$$

since for a Fermi gas $T = \sqrt{E/a}$. Consequently, a plot of the log of the fission probabilities versus $1/\sqrt{E}$ should be linear. In the top panel of Fig. 5 examples are given for three different fission excitation functions [24]. All three plots show a striking

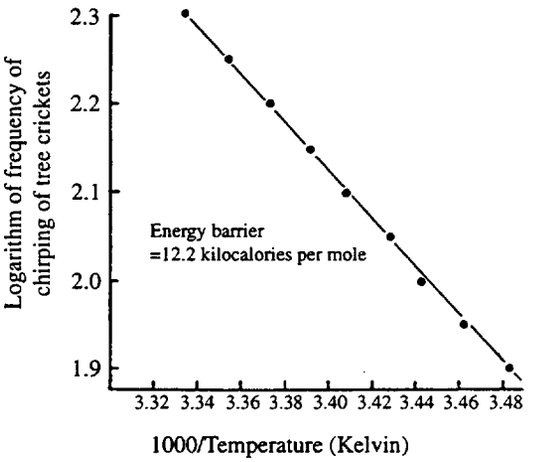

Fig. 6. Arrhenius plot for the chirping of tree crickets [25].

linearity with markedly different slopes. As shown by Eq. (15), the slopes are simply related to the corresponding fission barriers. For the three cases shown here, these barriers are widely different, and result in widely different slopes. Such a plot is well known to chemists as the Arrhenius plot for reaction rates.

Linear Arrhenius plots are general features of natural processes whose rates are thermally controlled. In Fig. 6 the temperature dependence of the cricket chirping frequency is shown as an example [25].

An application of this method to e^--induced fission is shown in the bottom panel of Fig. 5. The remarkably linear Arrhenius plots show that the increase in fission cross sections with energy is not due to an increase in the reaction cross section, as previously believed, but to the natural increase of the statistical fission probability with energy [24].

4.5 Arrhenius plots in multifragmentation

Comforted by these results, we can try to apply this method to the excitation functions for the production of 1, 2, 3, ...n-fragments in multifragmentation.

One possibility, which has been considered before [26,27], is to assume that the rate of r-fragment events is controlled by a corresponding r-fragment saddle point with an associated barrier B_r. Setting aside possible worries about the existence of such a saddle point configuration, let us write down the expected rate:

$$P_r \propto e^{-B_r/T}. \tag{16}$$

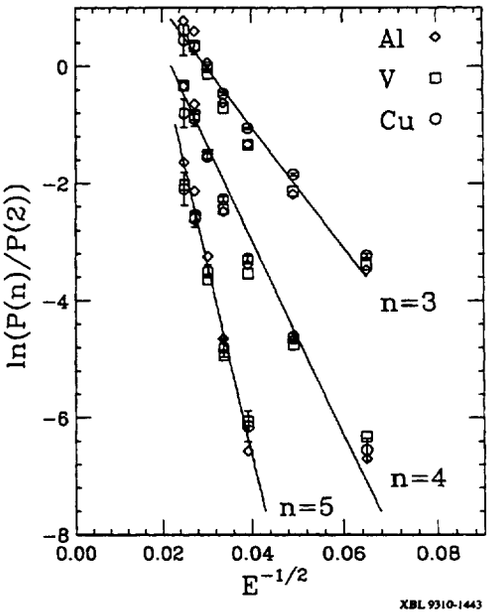

Fig. 7. The natural logarithm of the ratio of the efficiency corrected threefold, fourfold and fivefold probabilities to the twofold probability (symbols) as a function of $1/\sqrt{E}$ for the reactions ^{197}Au+^{27}Al, ^{51}V, and ^{nat}Cu at E/A=60 MeV [15]. The lines are best fits to the data. Statistical error bars are shown for the Cu target when they exceed the size of the symbols.

Taking the log of both sides, we obtain:

$$\ln P_r = a - \frac{B_r}{T} = a - \frac{K_r}{\sqrt{E}}. \tag{17}$$

Thus a plot of $\ln P_r$ versus $1/\sqrt{E}$ should be linear. This is shown in Fig. 7 with the data of Fig. 1.

In Fig. 8 a similar plot is shown for the reaction ^{129}Xe+^{197}Au [28]. However, rather than the kinematically reconstructed excitation energy, the transverse energy E_t has been used. E_t is defined as:

$$E_t = \sum_{i=1}^{N_c} E_i \sin^2 \theta_i, \tag{18}$$

where the kinetic energy of each particle E_i, weighted by the sine squared of its polar angle, is summed over the number N_C of all charged particles associated with the event. The transverse energy is Galilean invariant, and for a thermalized source is equal to 2/3 of the total excitation energy if the neutrons are included as well.

We compare E_t with the excitation energy per nucleon ϵ^* inferred from the kinematically reconstructed source velocity [16,17] for the reaction ^{129}Xe+^{51}V at E/A=50 MeV in Fig. 9. We observe a linear correlation between these two "excitation energy" global observables. From this point on, we shall frequently use E_t as a quantity

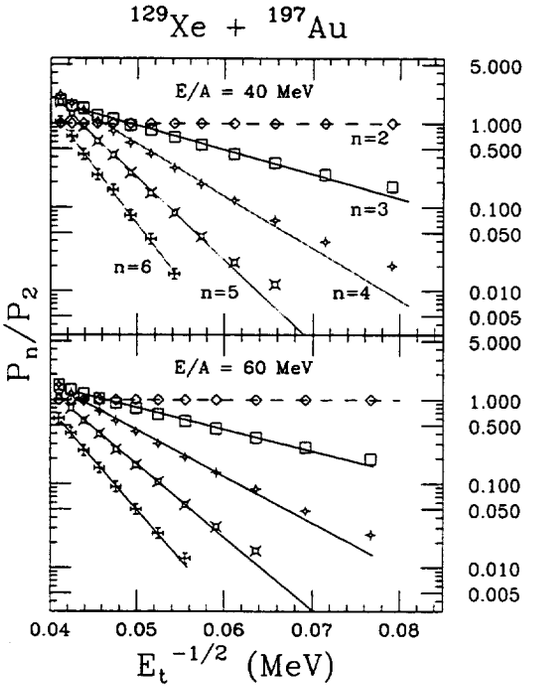

Fig. 8. The natural logarithm of the ratio of the 2, 3, 4, 5 and 6-fold to the 2-fold probability (symbols) as a function of $1/\sqrt{E_t}$ for the reaction ^{129}Xe+^{197}Au at bombarding energies of E/A=40 MeV (top panel) and 60 MeV (bottom panel) [28]. The lines are linear fits to the data.

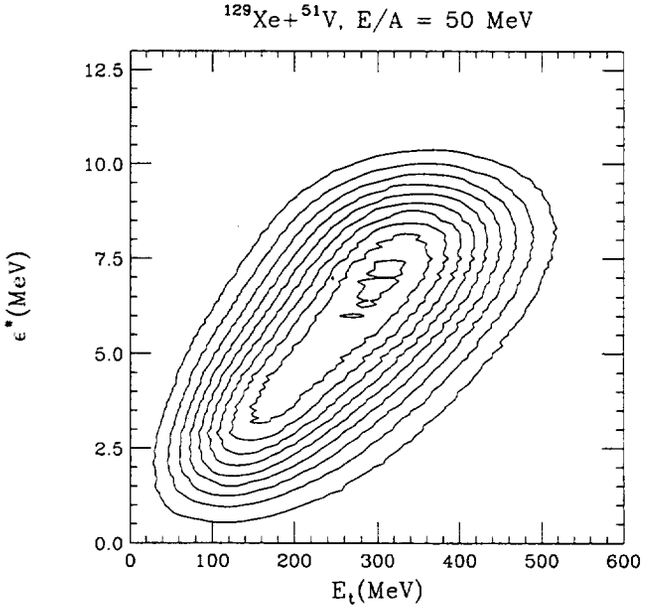

Fig. 9. Linear contour plot of the correlation between the excitation energy per nucleon ϵ^* (as determined from the kinematically reconstructed source velocity, see Eq. (6)) and the transverse energy E_t.

hopefully proportional to the excitation energy of the source.

The resemblance between Fig. 5 (portraying fissioning nuclei with different barriers), Figs. 7, 8 and Fig. 6 is striking. In Figs. 7 and 8 the Arrhenius plots are linear and there is a pleasing dependence of the slopes on the number of fragments n. This is consistent with the expectation that barriers should increase with increasing values of n.

The above comparisons would seem to settle the question about the statistical nature of multifragmentation, without recourse to a single simulation or model calculation. However, does the above comparison prove that there exist multifragment saddle points? Unfortunately not. To see this, let us consider an n-fragment event as produced by the (sequential) combination of n-independently emitted fragments. If the emission probability of each fragment is small, we can write:

$$P_n \propto p_1 p_2 p_3 ... \propto K(n) e^{-B_1/T_1} e^{-B_2/T_2} e^{-B_3/T_3} ... etc. \tag{19}$$

where B_1, B_2, etc. are the barriers for the individual fragments, T_1, T_2, etc. are the corresponding temperatures, and $K(n)$ is a combinatorial factor we will worry about later. If the energy is very high, the fragments might be emitted in succession with $T_1 \approx T_2 \approx T_3 \approx T$. Therefore,

$$P_n \propto K(n) e^{-(B_1+B_2+B_3+...)/T} = K(n) e^{-nB/T} \propto p^n, \tag{20}$$

where $B = (B_1 + B_2 + ...)/n$. Thus, linear Arrhenius plots do not readily distinguish between sequential and prompt statistical emission.

4.6 The problem of reducibility

Having established that there is a thermal signature in the E_t dependence of P_n, we may wonder whether, as suggested by Eq. (20), the various probabilities P_n result from the combination of an elementary probability p. In other words we would like to see whether the various P_n can be reduced to a single value of p. Carrying Eq. (20) one step further, one could attempt to extract the probability for a single fragment emission from the ratio:

$$\frac{P_n}{P_{n-1}} = \frac{K(n)}{K(n-1)} p. \tag{21}$$

Let us try this procedure on the nice set of data in Fig. 10. The probability P_n of emitting n IMFs ($3 \leq Z \leq 20$) has been measured as a function of the transverse energy E_t for the reaction ^{36}Ar+^{197}Au at E/A=80 MeV [29]. P_n is defined as:

$$P_n = \frac{N(n)}{\sum_{n=0}^{\infty} N(n)}, \tag{22}$$

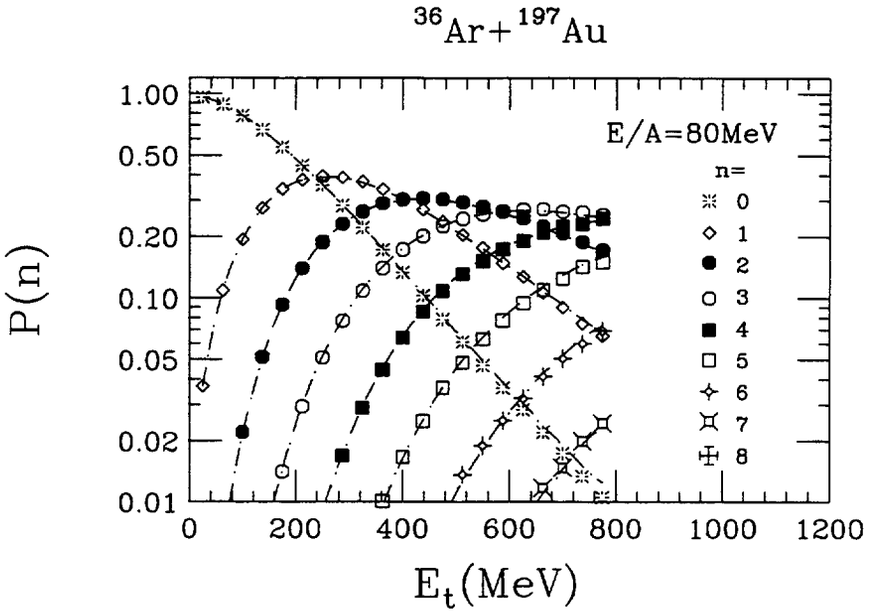

Fig. 10. The experimental (symbols) and the calculated (lines) probability to emit n IMFs as a function of E_t for the reaction ^{36}Ar+^{197}Au at E/A=80 MeV [29]. For number of fragments n=0-8, $P(n)$ is calculated assuming a binomial distribution (see Eq. (23)) with p determined directly from the mean and the variance (dotted lines) and with p extracted from the fit to the Arrhenius plot (dashed lines). The two different binomial calculations are nearly indistinguishable.

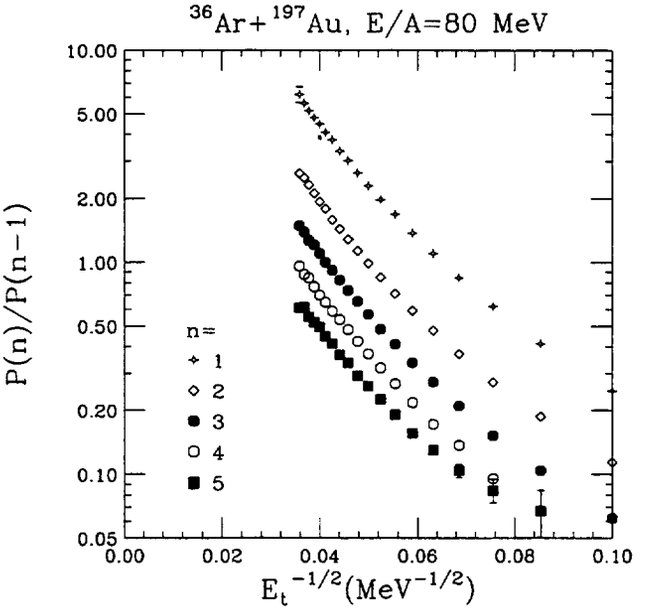

Fig. 11. The ratio of P_n/P_{n-1} as a function of $1/\sqrt{E_t}$

where $N(n)$ is the number of events with n IMFs for a given value of E_t.

The logarithm of the ratio in Eq. (21) is plotted as a function of $1/\sqrt{E_t}$ in Fig. 11. The pleasing linearity of each curve $\ln P_n/P_{n-1}$ versus $1/\sqrt{E_t}$, is disturbed by the

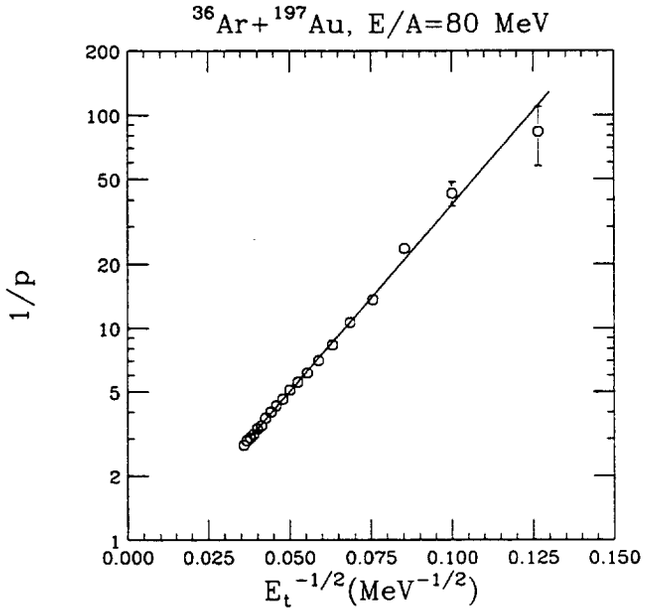

Fig. 12. The inverse of the single fragment emission probability p as a function of $1/\sqrt{E_t}$ for the reaction ^{36}Ar+^{197}Au at E/A=80 MeV.

fact that, while the resulting lines are indeed straight, they do not coalesce. They are parallel, but staggered with n. Of course, this staggering must have something to do with the factor $K(n)$ in Eqs. (19) and (21). A natural guess is that the n dependence of P_n at each E_t is Poissonian. However, the Poissonian distribution turns out to be unsatisfactory. On the other hand, the more general binomial distribution, surprisingly, works quite well:

$$P_n^m = \frac{m!}{n!(m-n)!} p^n (1-p)^{m-n}. \tag{23}$$

There is no obvious a priori reason why it should work. There is also the unpleasant fact of the new parameter m, which appears with unexplained origin. Nonetheless, let us see how it works.

4.7 Binomial reducibility and thermal scaling

In adopting this procedure we have two goals: 1) to verify the *binomial reducibility* of P_n to p; 2) to check if the elementary probability p gives a linear Arrhenius plot (thermal scaling) [29,30].

A quick and dirty way of implementing this procedure is to assume that the experimental distributions are indeed binomial. Then, the parameters p and m can be extracted from the mean and variance of n. For a binomial distribution, we have:

$$\langle n \rangle = mp \tag{24}$$

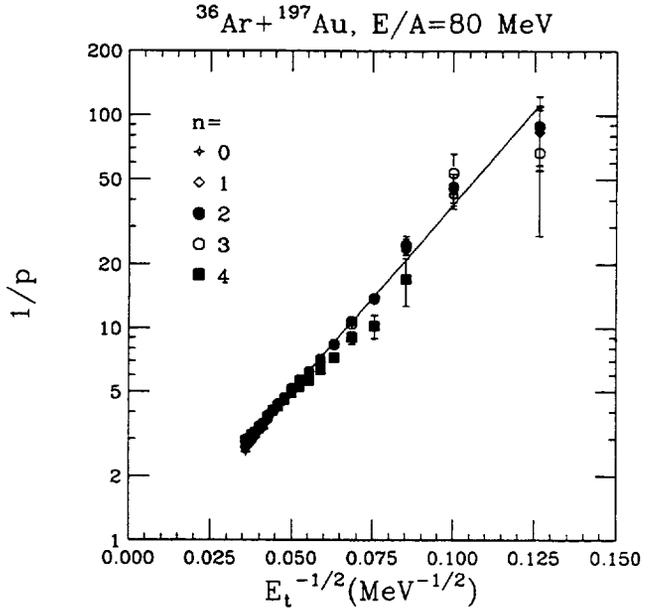

Fig. 13. 1/p extracted "differentially" using Eq. (26). The solid line is the fit to the data in Fig. 12.

and

$$\sigma_n^2 = \langle n \rangle (1 - p). \tag{25}$$

In Fig. 12 we show the results of this analysis. The extracted values of p give a beautifully linear Arrhenius plot. (Note that we are plotting $1/p$ rather than p, for reasons explained in Sec. 4.8.3.) The reconstructed values of P_n from the derived values of p and m are shown by the dotted lines in Fig. 10. The agreement with the data is very pleasing. Indeed, the distributions must be binomial. Of course, part of the beauty is spoiled by the realization that we determine a pair of m, p values at each value of E_t. However, one can fit the Arrhenius plot with a straight line. Two parameters now suffice to determine any value of p. Even with only two parameters, the reproduction of P_n is just as good as before, and evidenced by the dashed curves in Fig. 10 which fall nearly on top of the calculations using the reconstructed values of P_n from $\langle n \rangle$ and σ_n^2 (dotted curves).

We can further test the binomiality of the distributions by extracting p from any pair of excitation functions:

$$\frac{1}{p} = \frac{P_n^m}{P_{n+1}^m} \frac{m-n}{n+1} + 1. \tag{26}$$

The values of p extracted "differentially" by this procedure collapse to a straight line for $n \leq 4$ as demonstrated in Fig. 13. These values of p also agree quite well with those extracted from the mean and variance of the IMF distribution (as in Fig. 12). (The solid line in Fig. 13 is the fit from Fig. 12.)

How general are these features? We can test them on a broad set of reactions like the

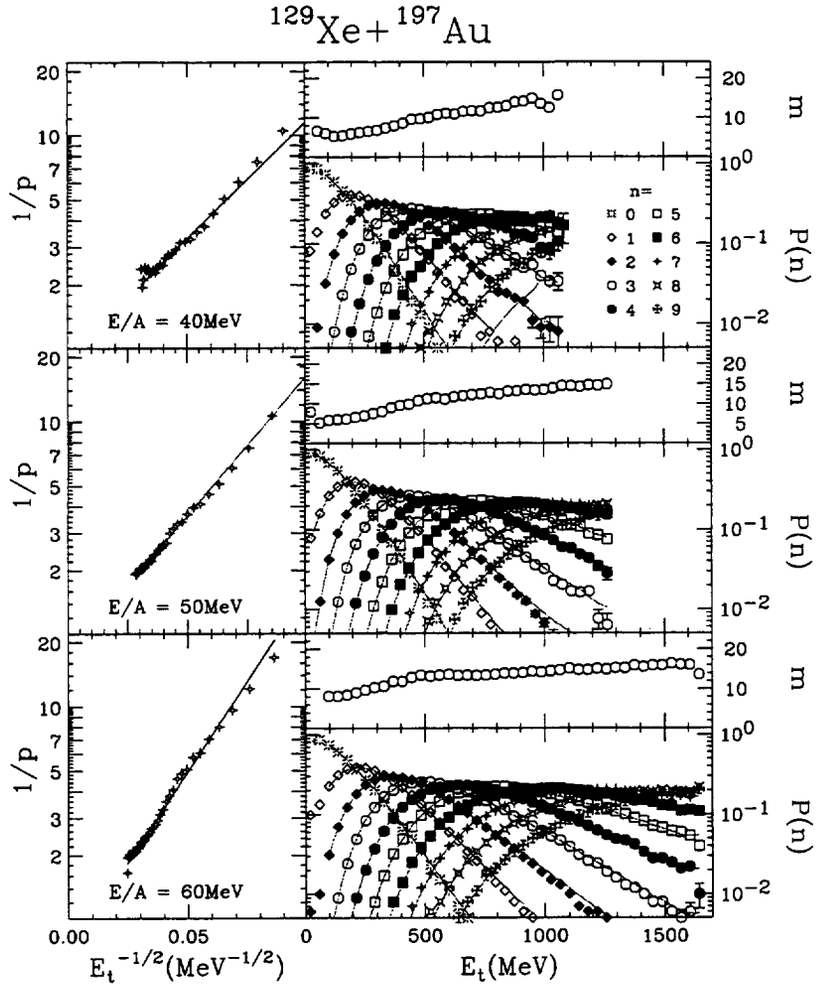

Fig. 14. ^{129}Xe+^{197}Au reactions: The reciprocal of the single fragment emission probability $1/p$ is shown as a function of $1/\sqrt{E_t}$ (left column). The solid line is a linear fit to $\ln 1/p$. The probability $P(n)$ of emitting n IMFs and the parameter m are shown as a function of the transverse energy E_t in the right column. The solid curves are calculated assuming a binomial distribution with the extracted values of p and m. The three rows correspond to different bombarding energies: E/A=40 MeV (top); E/A=50 MeV (middle); and E/A=60 MeV (bottom).

^{129}Xe-induced reactions on ^{nat}Cu, ^{89}Y, ^{165}Ho, and ^{197}Au targets at E/A= 40, 50 and 60 MeV [30] as well as ^{36}Ar+^{197}Au at E/A=50, 80 and 110 MeV. Consider first the reactions of ^{129}Xe+^{197}Au at three bombarding energies. The excitation functions P_n are plotted in the right column of Fig. 14 for n=0 to n=9, together with the solid curves generated from the binomial distribution (Eq. (23)). The input values for p and m in Eq. (23) are extracted from the experimental mean and the variance of the IMF multiplicity distributions by using the binomial relations listed in equations (24) and (25). Excellent agreement between the experimental n-fragment emission probabilities (symbols) and the binomial calculations (curves) for the entire E_t range is observed for values of n up to 9 at all three bombarding energies. This remarkable agreement means that the probability P_n is indeed binomial and can be reduced to

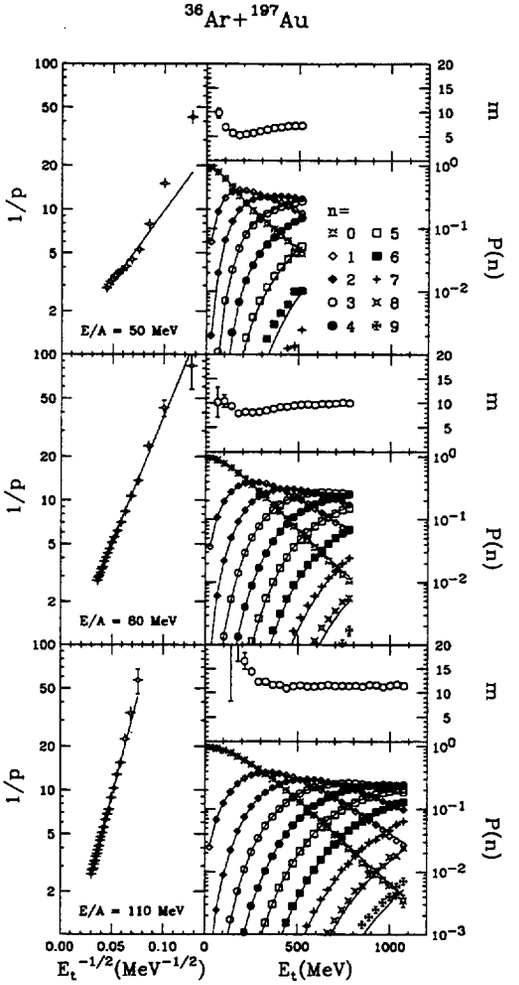

Fig. 15. ^{36}Ar+^{197}Au reactions: The reciprocal of the single fragment emission probability $1/p$ is shown as a function of $1/\sqrt{E_t}$ (left column). The solid line is a linear fit to $\ln 1/p$. The probability $P(n)$ of emitting n IMFs and the parameter m are shown as a function of the transverse energy E_t in the right column. The solid curves are calculated assuming a binomial distribution with the extracted values of p and m. The three rows correspond to different bombarding energies: E/A=50 MeV (top); E/A=80 MeV (middle); and E/A=110 MeV (bottom).

an elementary probability p.

To investigate the temperature dependence of the elementary probability, $1/p$ is plotted (using a log scale) as a function of $1/\sqrt{E_t}$ in the left column of Fig. 14 [30]. A linear dependence is observed for all three bombarding energies, similar to the pattern observed previously for the ^{36}Ar+ ^{197}Au reactions at E/A=80 [29]. The solid lines are linear fits to the data. The linearity of these plots clearly illustrates the "thermal" nature of p over the measured E_t range.

Similar results are obtained for the more asymmetric system ^{36}Ar+^{197}Au at bombarding energies of E/A=50, 80, and 110 MeV (see Fig. 15).

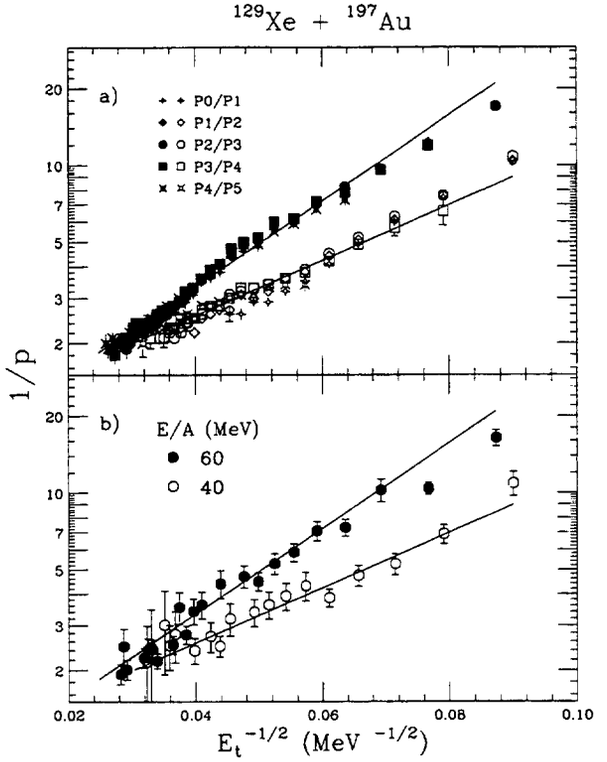

Fig. 16. ^{129}Xe+^{197}Au reactions: $1/p$ extracted "differentially" (a) using Eq. (26) and "independently" (b) using Eq. (27) are shown as a function of $1/\sqrt{E_t}$. The different symbols represent the probabilities p extracted from the indicated values of $P(n)$. The lines are linear fits to $\ln(1/p)$ which is calculated from $\langle n \rangle$ and σ^2 of the IMF multiplicity distributions. The solid and blank symbols correspond to bombarding energies of E/A=60 MeV and E/A=40 MeV, respectively.

Again we can extract p "differentially" from the ratio of any pair of excitation functions P_n/P_{n+1} as given by Eq. (26). The values of p obtained "differentially" can be compared with those calculated "integrally" from the $\langle n \rangle$ and σ_n^2 of the IMF multiplicity distributions. Fig. 16a shows that the differentially determined values of p up to n=4 collapse onto the straight lines taken from Fig. 14. For n >4 data (not shown), good agreement is observed at large transverse energies E_t >400 MeV, although scattering about the fitted line occurs at small transverse energies due to poor statistics.

There is also an independent method (neither $\langle n \rangle$ nor σ_n^2 is used) to extract p by using the ratios of two consecutive pairs of excitation functions P_n/P_{n+1} and P_{n+1}/P_{n+2}. The resulting expression for $1/p$ is:

$$\frac{1}{p} = \frac{P_n P_{n+1}}{(n+1)P_{n+1}^2 - (n+2)P_n P_{n+2}} + 1. \tag{27}$$

To minimize statistical uncertainties, n is taken to correspond to the most probable n-fold at a given transverse energy. The extracted values of p (symbols) for bombarding energies at E/A=40 and 60 MeV agree reasonably well with those obtained integrally

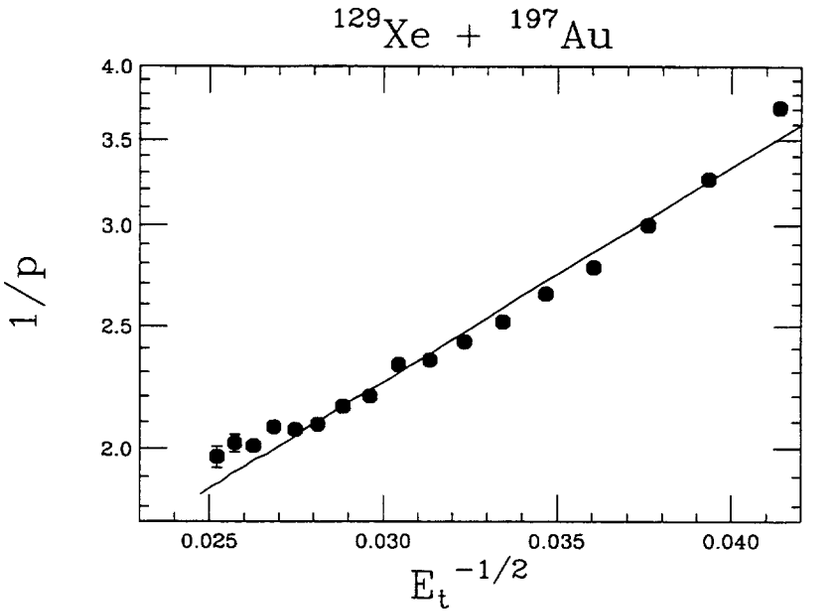

Fig. 17. Extracted values of $1/p$ as a function of $1/\sqrt{E_t}$ shown for the ^{129}Xe+^{197}Au reaction at E/A=60 MeV. The linear fit is the same as in Fig. 14. Data with E_t less than 700 MeV are not shown.

(line) in Fig. 16b. The observed consistency among the three different methods of extracting p confirms the binomial nature of P_n and the thermal dependence of p.

Concerning the linearity of the Arrhenius plot, our eyes may be mostly impressed by the tail of the data points toward small transverse energies, but the Arrhenius plot remains linear even if one excludes these data, as shown in Fig. 17, where only data with E_t larger than 700 MeV are plotted (the straight line is the fit from Fig. 14). In fact, the fitting procedure, unlike our eyes, is dominated by the large amount of data available at large transverse energies. The good agreement between the fit and the data shown in the above Arrhenius plots clearly demonstrates the linearity over the entire range of measured E_t.

At this point we investigate the target dependence. Fig. 18 shows the excitation functions for ^{129}Xe-induced reactions on ^{nat}Cu, ^{89}Y, and ^{165}Ho targets at E/A=40 MeV. Interestingly, the excitation functions are almost identical for all three targets over the entire range of the transverse energy. A most remarkable result is that the Arrhenius plots for different targets collapse onto a universal line independent of the target mass as shown in the right column of Fig. 18. Target independence was also observed in the excitation functions for emission of n IMFs [17,31] (see for instance Figs. 1 and 7) and in the dependence of the average IMF multiplicity on the total charged particle multiplicity [18]. We observe a similar independence when the average IMF multiplicity is plotted as a function of E_t.

For the ^{nat}Cu and ^{89}Y targets, the target is lighter than the ^{129}Xe projectile, and the observed target independence finds its natural explanation within the incomplete

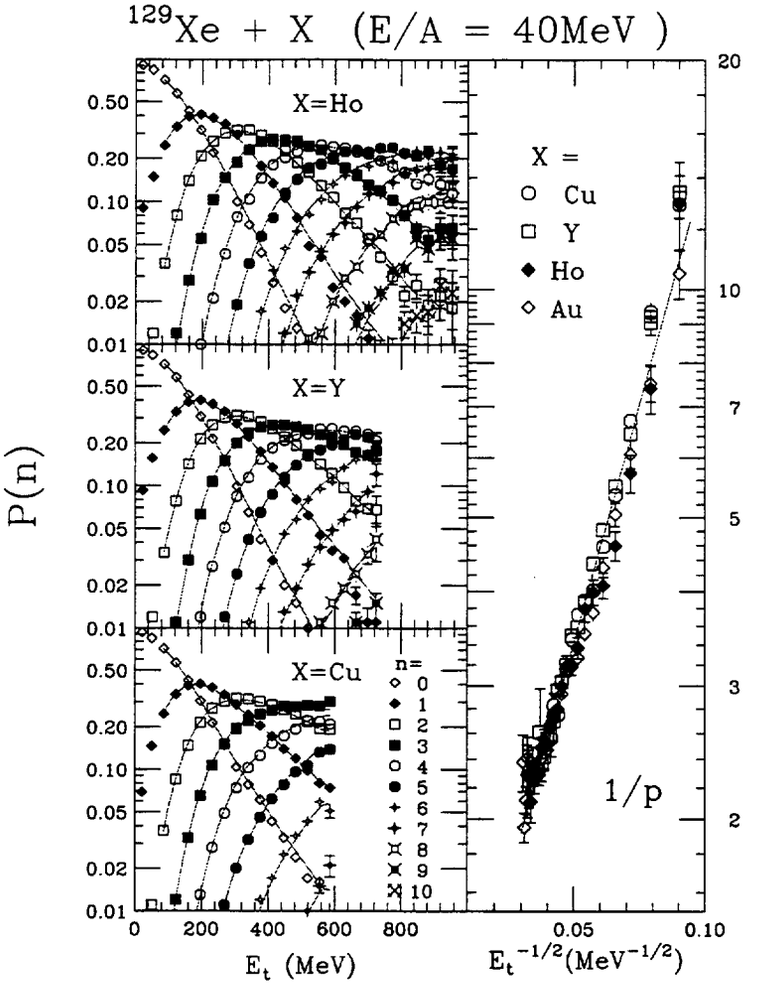

Fig. 18. (Left column): The probability P(n) for emitting n IMFs is shown as a function of E_t for ^{129}Xe-induced reactions (E/A=40 MeV) on different targets: ^{nat}Cu (bottom), ^{89}Y (middle), ^{165}Ho (top). The solid curves are binomial calculations of $P(n)$ using extracted values of p and m. (Right column): The reciprocal of the single fragment emission probability $1/p$ is shown as function of $1/\sqrt{E_t}$ for different targets (^{nat}Cu, ^{89}Y, ^{165}Ho, ^{197}Au). The line is a linear fit to the data.

fusion model [32,33] as discussed before regarding the data shown in Figs. 1 and 7. Neglecting Q-values and recoil effects, the characterization of the incomplete fusion source depends solely on the mass removed from the lighter target and incorporated by the heavier projectile. The actual size of the target nucleus is unimportant. However, for the heavier ^{165}Ho and ^{197}Au targets, the observed target independence seems to imply a similar mass transfer to the ^{129}Xe projectile. This picture is contrary to the conventional incomplete fusion mechanism and remains an unresolved puzzle.

The extracted values of p from the Arrhenius plot in Fig. 18 are used to generate the binomial distributions (curves) shown in the left column of Fig. 18. The excellent agreement between data and binomial calculations for the IMF multiplicity distributions demonstrates the binomial nature of P_n and its reducibility to p independent

of the specific target. In addition, ^{129}Xe-induced reactions at the two higher bombarding energies (E/A= 50 and 60 MeV) show a similar target independence and the Arrhenius plots are found to become steeper with increasing bombarding energies.

4.8 General considerations and questions

Confronted with this large body of experimental evidence and with the solidly established empirical features of binomial reducibility and thermal scaling, we cannot avoid the urge to speculate on their meaning and origin.

Reducibility suggests that fragments are emitted nearly independent of each other, with essentially the same probability within an event. This seems to conflict with the well-established fragment-fragment interaction, as observed in angular correlations. This clash is, however, only apparent. The observed (Coulomb) perturbations involve only a few angular degrees of freedom. The decay probability is proportional to the overall channel level density, which is dominated by the overwhelmingly more abundant internal degrees of freedom.

The binomial composition of the elementary probability implies that the system is given m chances to emit a fragment with constant probability p. Thermal scaling implies that the elementary probability p is of the form: $p = \exp(-B/T)$ where B is the barrier for fragment emission. Several questions arise at this point.

4.8.1 Why a single barrier?

The more directly interpretable physical parameter contained in this analysis is the binary decay barrier B which is proportional to the slope of the Arrhenius plot. One may wonder why only a single binary barrier seems to be needed, while different fragments with presumably different barriers are present. Let us consider a barrier distribution as a function of mass asymmetry x of the form $B = B_0 + ax^s$, where B_0 is the lowest barrier in the range considered (IMF: $Z_{\rm th} \leq Z \leq 20$). Then,

$$p = \int e^{-B_0/T} e^{-ax^s/T} dx \approx \left(\frac{T}{a}\right)^{1/s} e^{-B_0/T}. \tag{28}$$

Thus the simple form of Eq. (20) is retained with a small and renormalizable pre-exponential modification. An average binary barrier suffices, since the average value of p is dominated by the lightest fragment ($Z_{\rm th}$) with the lowest barrier in the range considered.

To explore the dependence of the barrier upon $Z_{\rm th}$, we have performed the same analysis by progressively increasing $Z_{\rm th}$. The excitation functions and their corresponding Arrhenius plots with different values of $Z_{\rm th}$ (3 to 7) are shown in Fig. 19

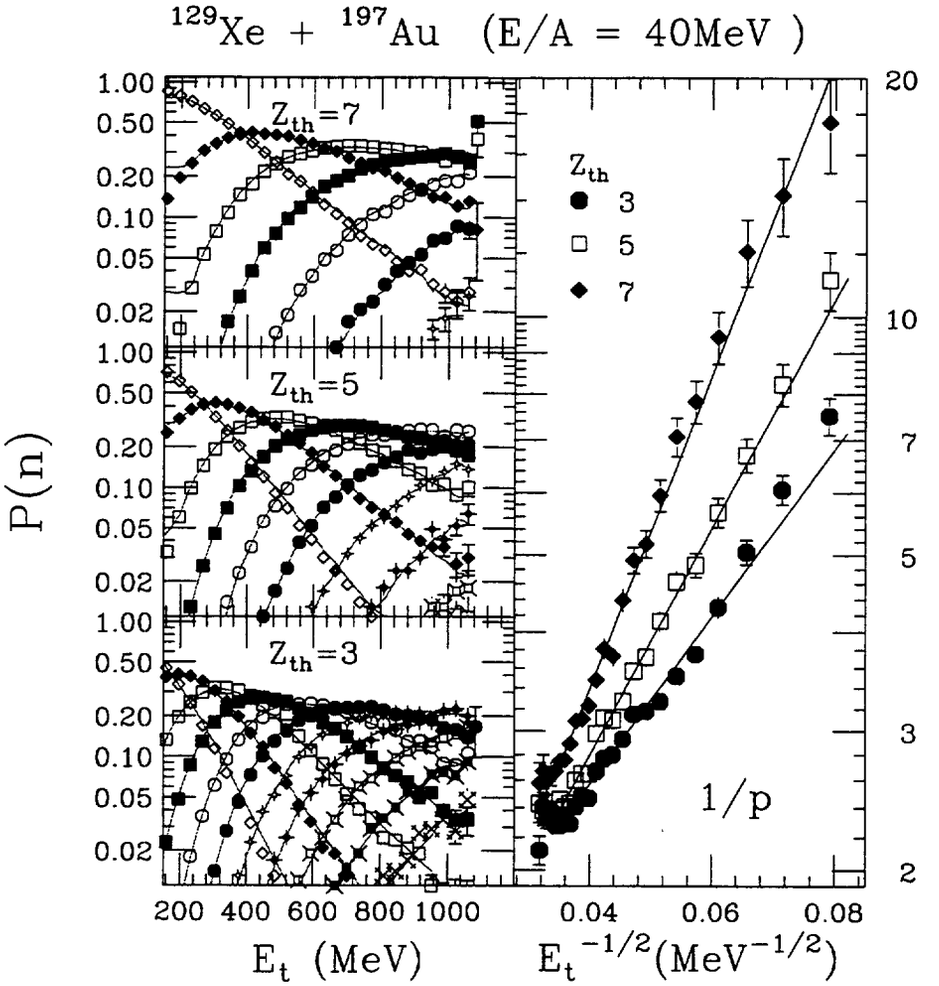

Fig. 19. (Left column): The probability $P(n)$ for emitting n IMFs is shown as a function of E_t for ^{129}Xe+^{197}Au reaction at E/A=40 MeV with different values of lower threshold in the definition of IMF $Z_{\rm th}$=3 (bottom), $Z_{\rm th}$=5 (middle) and $Z_{\rm th}$=7 (top). (Right column): The corresponding values of $1/p$ are shown as a function of $1/\sqrt{E_t}$. The solid lines are linear fits to the data.

for the ^{129}Xe+^{197}Au reaction at E/A=40 MeV. The remarkable result is that these excitation functions, though dramatically changed, retain their binomial reducibility, and their associated Arrhenius plots remain linear. The slopes of the Arrhenius plots become progressively steeper with increasing values of $Z_{\rm th}$, with the exception of the cluster of data points at large transverse energies. The sensitivity of these slopes to $Z_{\rm th}$ is consistent with the expected increase of the emission barriers $B(Z)$ with Z. We consider this a powerful indication of the physical meaning of p.

4.8.2 Why binomial rather than Poisson?

At this stage one might stand back and contemplate the pleasing simplification introduced into multifragmentation by reducibility and thermal scaling. A closer inspection, however, reveals the inescapable fact that *binomial* reducibility, far from being

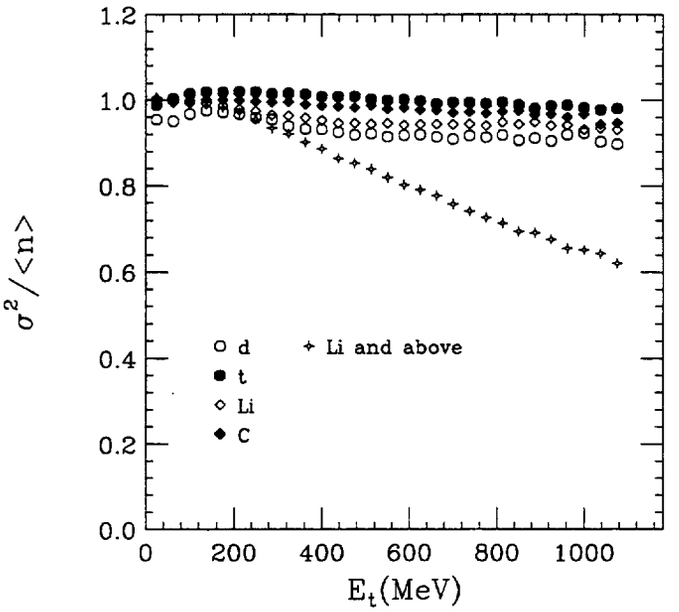

Fig. 20. The ratio of the variance to the mean number of d, t, Li and C (solid and open symbols) emitted from the reaction ^{36}Ar+^{197}Au at E/A=110 MeV. The star symbols show the same ratio for all IMFs ($3 \leq Z \leq 20$).

a satisfying property, is instead an outright embarrassment.

Reducibility is a fine concept, but why binomial, rather than Poisson reducibility? After all, Poissonian reducibility would have worked just as well, without the additional parameter m and its problematic interpretation.

The possibility of problems arising at the level of the experiment itself, or at the data sorting stage, that might somehow narrow the natural width of the distributions, unwittingly transforming a Poissonian into a binomial, have to be ruled out. We shall dwell at length on these problems later on in part B.

Some understanding of these matters is gained by looking at the multiplicity distributions for an *individual* isotope of a given A, or fragment of a given Z.

Let us recall that for a Poisson distribution the ratio of the variance to the mean is one, while for a binomial it is less than one (see Eqs. (24, 25)). In Fig. 20 the ratio of the variance to the mean is shown as a function of E_t for the particles d, t, Li, and C. These ratios remain close to one, with only minimal sagging at the highest values of E_t. This behavior is in contrast with the results obtained when all particles with $Z \geq Z_{\rm th}$ are included (shown by the star symbols). In this case the ratio can be as small as 0.6, thus precluding a Poisson description. However, the distributions constructed from individual Z or A are, for all intents and purposes, Poissonian! The Poissonian fits shown in Fig. 21 are quite satisfactory. Had we begun looking at the data in this way, we would have inferred Poissonian reducibility without any nagging doubts troubling our faith. However, as soon as we bring more fragments at a time

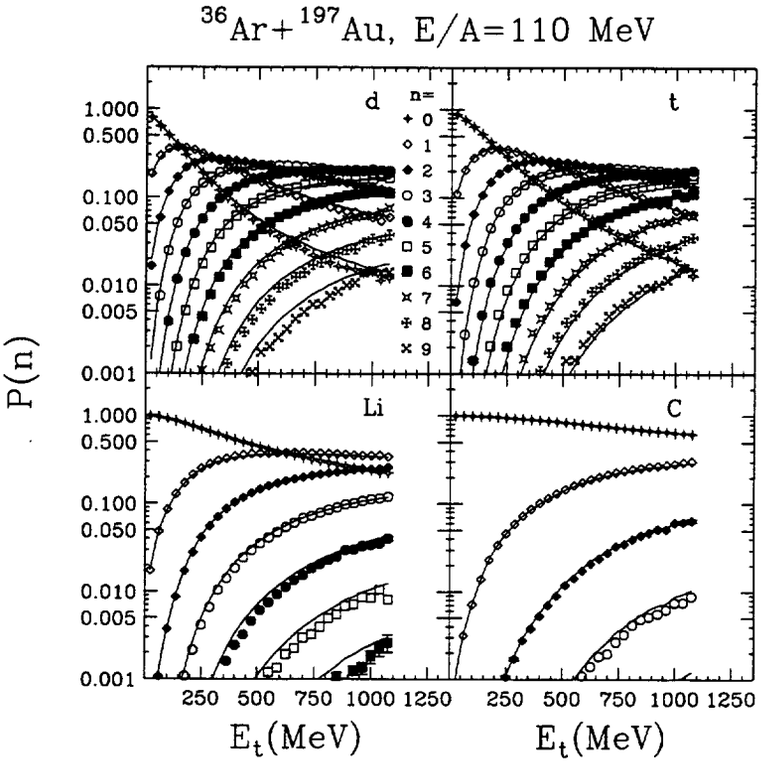

Fig. 21. The excitation functions P_n for d (top left), t (top right), Li (bottom left) and C (bottom right) for the reaction ^{36}Ar+^{197}Au at E/A=110 MeV. The lines are a Poisson fit to the data.

into the fold or fit, the variance to mean ratio starts sagging substantially as E_t increases, and the distributions become invariably binomial. How can we justify this surprising finding? We shall advance two possibilities.

4.8.3 Sequential interpretation

Let us assume that the multifragmentation process is sequential in time. The statistical probability (decay width) for the emission can be written as:

$$\Gamma = \hbar\omega e^{-B/T} \tag{29}$$

and

$$p = \frac{\Gamma}{\hbar\omega} = e^{-B/T} \tag{30}$$

where ω is a characteristic channel frequency, and B is the barrier. The corresponding time constant is:

$$\tau = \tau_0 e^{B/T}, \tag{31}$$

where τ_0=$1/\omega$ can be interpreted as a characteristic channel time constant. Then τ becomes the actual decay time constant. The Boltzmann factor $\exp[-B/T]$ represents

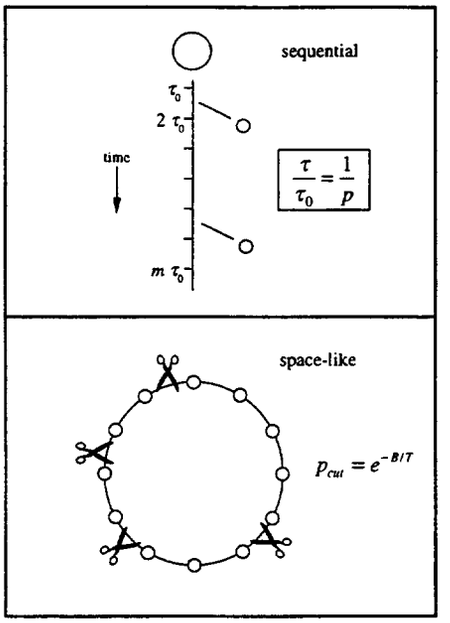

Fig. 22. Schematic diagram of two possible interpretations of binomial reducibility: (top) a sequential picture and (bottom) 1-dimensional percolation.

the probability that a fragment is successfully produced during the time τ_0. The quantity m now becomes the number of natural time intervals during which the system can try to emit a fragment with probability p (shown schematically in top half of Fig. 22). By construction, the probability of observing n fragments is given by the binomial equation. In this picture τ is the mean time between fragments, which decreases rapidly with increasing temperature, according to Eq. (31). The Arrhenius plots shown in Figs. 12, 14, 15 and 18 actually give $1/p = \tau/\tau_0$, which is the "relative" time spacing as a function of $1/T$. If this statistical sequential picture corresponds to reality, it implies that at low temperature the fragments are well separated in time. As the temperature increases, the time separation becomes progressively shorter, tending to τ_0.

The time separation between fragments can be inferred experimentally in more direct ways, for instance from the fragment-fragment Coulomb perturbation. There are good indications that this time separation is becoming smaller with increasing energy [34–37]. It has been claimed that this is a signal for the transition from sequential to simultaneous emission [37]. Yet, from our above discussion, it follows that this time contraction is a natural feature of the sequential statistical picture, without recourse to different mechanisms.

The quantity m defines a time window $\Delta t \approx m\tau_0$ during which the emission is possible. It could indicate a time, determined perhaps by the dynamics, during which the barriers for the emission of the fragment are lowered either by an expansion or by a stretching of the system. This feature is contained for instance in a model by Friedman [38], where the fragments are statistically emitted with high probability when the system has reached maximum expansion.

What prevents the distribution from becoming Poissonian is the finite length of the time interval Δt, which may be dictated by the dynamics of the process. Of course, the distribution can still look Poissonian if we restrict the definition of particles in such a way that the probability p becomes very small.

4.8.4 Space-like interpretation

This second possibility considers the finiteness of the source size rather than that of the decay time as the culprit for binomiality.

For instance, consider a process that is space-like as in one-dimension percolation, or the breaking of a pearl necklace (shown schematically in the bottom half of Fig. 22). There are m links, each of which has the probability $p = \exp[-B/T]$ of being cut. This automatically gives the binomial distribution of Eq. (23). This is suggestive of an m-fragment saddle configuration.

Obviously, a source of charge Z_0 cannot emit more than $m = Z_0/Z$ fragments of charge Z. Thus, no matter how we try to implement fragment emission, charge conservation will make itself felt at the very least by chopping the original Poissonian distributions when all the charge is exhausted.

Some light as to which of the two above possibilities is more plausible is shed by the observed scaling of m with the lower threshold $Z_{\rm th}$. Fig. 23 shows that m and $Z_{\rm th}$ are not independent, but connected by the approximate relationship:

$$mZ_{\rm th} \approx \text{constant}. \tag{32}$$

Sequential emission, as considered above, can explain this scaling in terms of the proportionality of τ_0 and Z which arises assuming the quantal motion of a particle of mass $M \propto Z$ in a square well. This result, unfortunately, depends on the shape of the potential, and is patently different for a harmonic oscillator.

The second possibility gives an immediate and more natural explanation to the m scaling. We could venture that:

$$mZ = Z_0 \tag{33}$$

where Z_0 is the atomic number of the source. This is somewhat difficult to verify, because, for any given value of (sufficiently small) Z, the distribution looks Poisso-

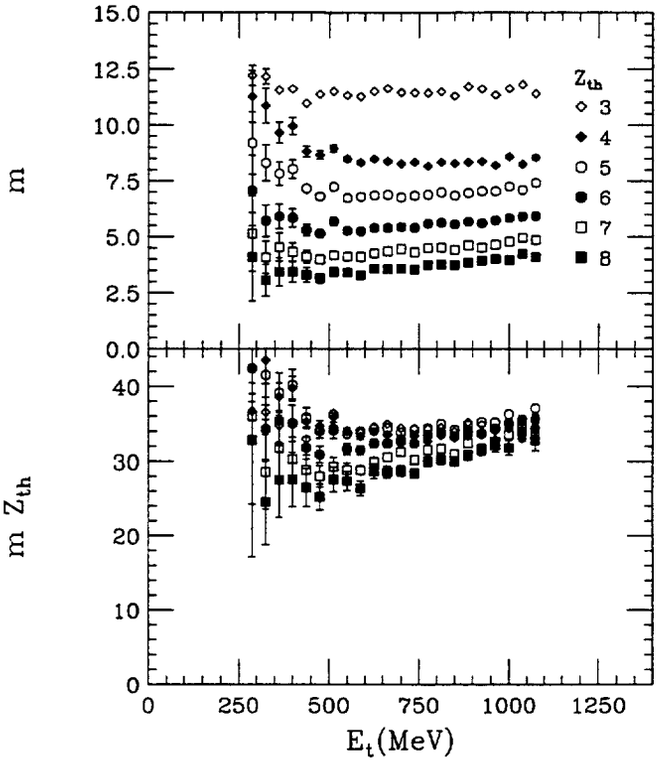

Fig. 23. The empirical scaling of $mZ_{\rm th}$ for different $Z_{\rm th}$ (different symbols) for the reaction ^{36}Ar+^{197}Au at E/A=110 MeV.

nian, as we have remarked before, so that the extraction of m becomes problematic. However, by extending the definition of particle in terms of a lower charge threshold ($Z_{\rm th}$), we can expect:

$$mZ_{\rm th} \propto Z_0 \tag{34}$$

as approximately observed.

5 Reducibility and Thermal Scaling of the Charge Distributions

The aspects of reducibility and thermal scaling observed in the integrated fragment emission probabilities lead naturally to the question: Is the charge distribution itself reducible and thermally scalable? In particular, what is the charge distribution form that satisfies the condition of reducibility and of thermal scaling? Strong hints that reducibility is retained in the Z distribution have been observed when the lower Z cutoff $Z_{\rm th}$ is increased in the IMF definition. The resulting fragment multiplicities are still binomially distributed, and the Arrhenius plots become steeper in accordance with expectation that the barrier B in Eq. (30) increases with Z. This is clearly shown in Fig. 19.

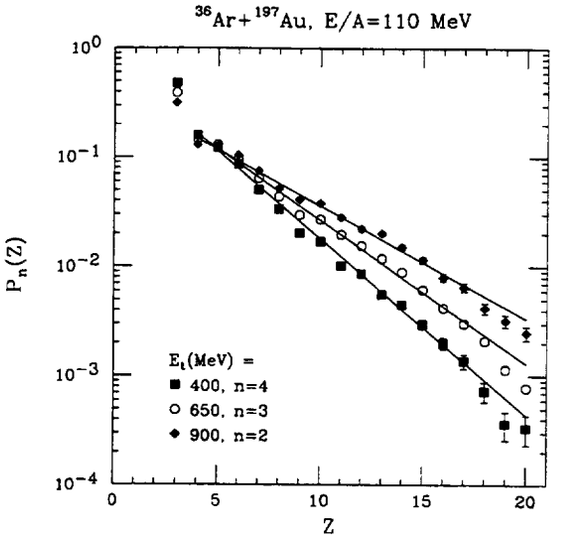

Fig. 24. The n-fold charge distributions $P_n(Z)$ for intermediate mass fragments (IMF: $3 \leq Z \leq 20$) are plotted for the indicated cuts on transverse energy E_t and IMF multiplicity n. The width of the cuts ΔE_t is 37.5 MeV. The solid lines are exponential fits over the range Z=4-20.

In what follows we will show that experimental charge distributions do, in fact, show most interesting reducibility and thermal scaling properties.

Let us first consider the aspect of reducibility as it applies to the charge distributions. In its broadest form, reducibility demands that the probability $p(Z)$, from which an event of n fragments is generated by m trials, is the same at every step of extraction. The consequence of this extreme reducibility is straightforward: the charge distribution for the one-fold events is the same as that for the n-fold events, and equal to the singles distributions, i.e.:

$$P_{(1)}(Z) = P_{(n)}(Z) = P_{\text{singles}}(Z) = p(Z). \tag{35}$$

We now consider the consequences of the thermal dependence of p [29,30] on the charge distributions. If the one-fold = n-fold = singles distributions is thermal, then:

$$P(Z) \propto e^{-\frac{B(Z)}{T}} \tag{36}$$

or $T \ln P(Z) \propto -B(Z)$. This suggests that, under the usual assumption $E_t \propto E^*$ (where E^* is the excitation energy [29]), the function

$$\sqrt{E_t} \ln P(Z) = D(Z) \tag{37}$$

should be independent of E_t and of n.

In the ^{36}Ar+^{197}Au reaction considered here, as in other reactions [18,39], the charge distributions are empirically found to be nearly exponential functions of Z:

$$P_n(Z) \propto e^{-\alpha_n Z} \tag{38}$$

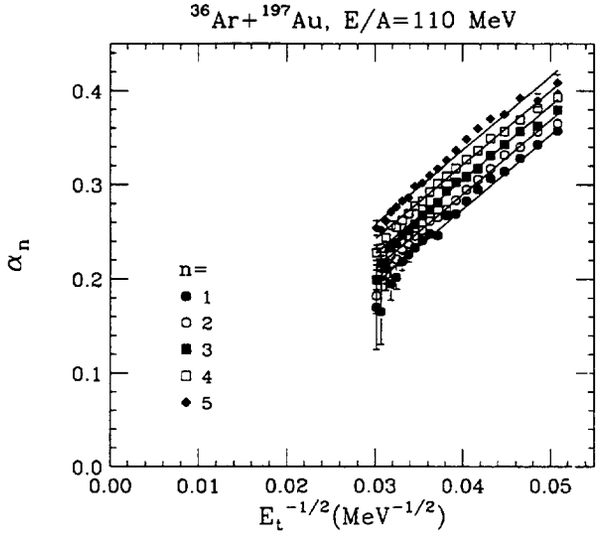

Fig. 25. The exponential fit parameter α_n (from fits to the charge distributions, see Eq. (38)) is plotted as a function of $1/\sqrt{E_t}$. The solid lines are a fit to the values of α_n using Eq. (40).

as shown in Fig. 24. In light of the above considerations, we would expect for α_n the following simple dependence:

$$\alpha_n \propto \frac{1}{T} \propto \frac{1}{\sqrt{E_t}} \tag{39}$$

for all folds n. Thus a plot of α_n versus $1/\sqrt{E_t}$ should give straight lines. This plot is shown in Fig. 25 for ^{36}Ar+^{197}Au at E/A=110 MeV.

The expectation of thermal scaling appears to be met quite satisfactorily. For each value of n the exponent α_n shows the linear dependence on $1/\sqrt{E_t}$ anticipated in Eq. (39). However, the extreme reducibility condition demanded by Eq. (35), namely that $\alpha_1 = \alpha_2 = ... = \alpha_n = \alpha$, is not met. Rather than collapsing on a single straight line, the values of α_n for the different fragment multiplicities are offset one with respect to another by what appears to be a small constant quantity.

In fact, one can fit all of the data remarkably well, assuming for α_n the form:

$$\alpha_n = \frac{K'}{\sqrt{E_t}} + nc. \tag{40}$$

Such a fit is shown in Fig. 25. This implies:

$$\alpha_n = \frac{K}{T} + nc \tag{41}$$

or more generally, for the Z distribution:

$$P_n(Z) \propto e^{-\frac{B(Z)}{T} - ncZ}. \tag{42}$$

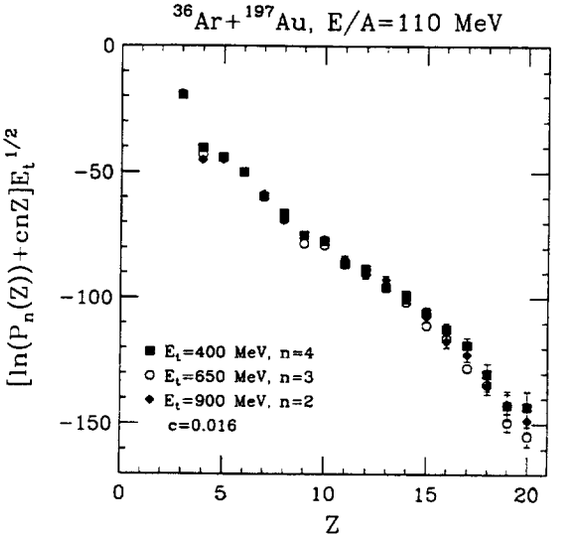

Fig. 26. The "reduced" charge distributions (see Eq. (43)) are plotted for the same cuts on E_t and n as in Fig. 24. The different data sets are normalized at Z=6. The value of c=0.016 is the spacing between the curves shown in Fig. 25.

Thus, we expect a more general reducibility and thermal scaling expression for the charge distribution *of any form* to be:

$$[\ln P_n(Z) + ncZ]\sqrt{E_t} = F(Z) \tag{43}$$

for all values of n and E_t. This equation indicates that it should be possible to reduce the charge distributions associated with any intermediate mass fragment multiplicity and any E_t cut to the charge distribution of the singles. As a demonstration of this reducibility, we have compared $P_n(Z)$ and $F(Z)$ in Figs. 24 and 26. Fig. 24 compares three charge distributions for different cuts on E_t and n; their slopes are clearly different. The corresponding reduced quantities $F(Z)$, on the other hand, collapse to a single curve in Fig. 26.

We stress that the reduced quantity in Eq. (43) is *independent* of the functional form of the charge distribution. However, we have used the fact that the charge distributions are well described by exponential fits in the ^{36}Ar+^{197}Au reaction to summarize the reducibility of an enormous amount of data. Nearly one hundred different charge distributions are represented in Fig. 25. We feel this is more impressive than the reducibility demonstrated directly in Figs. 24 and 26, where for practical purposes we are only able to demonstrate reducibility for a few different charge distributions.

5.1 Origin of c

What is the origin of the regular offset that separates the curves in Fig. 25? The general form of Eq. (42) suggests the presence of an entropy term that does not

depend explicitly on temperature [40,41]. The general expression for the free energy (in terms of enthalpy H, temperature T and entropy S):

$$\Delta G = \Delta H(Z) - T\Delta S(Z) \tag{44}$$

leads to the distribution:

$$P(Z) \propto e^{-\frac{\Delta H(Z)}{T}+\Delta S}. \tag{45}$$

Typically, ΔS is of topological or combinatorial origin. For instance, a factor of this sort would appear in the isomerization of a molecule involving a change of symmetry. In our specific case ΔS may point to an asymptotic combinatorial structure of the multifragmentation process in the high temperature limit.

As an example, we consider the Euler problem of an integer to be written as the sum of a fixed number n of smaller integers, and calculate the resulting integer distribution. Specifically, let us consider an integer Z_0 to be broken into n pieces. Let n_Z be the number of pieces of size Z. The most likely value of n_Z can be obtained by extremization of the function [42]:

$$e^{-I} = e^{\sum[n_Z \ln n_Z - n_Z]+K\sum n_Z Z+\gamma\sum n_Z} \tag{46}$$

where the Lagrange multipliers K and γ are associated with the constraints:

$$\sum n_Z Z = Z_0; \sum n_Z = n. \tag{47}$$

From the extremization we obtain:

$$\frac{\partial I}{\partial n_Z} = \ln n_Z + KZ + \gamma = 0 \tag{48}$$

or

$$n_Z = e^{-KZ-\gamma}. \tag{49}$$

The constraints now read:

$$Z_0 = \sum Z e^{-KZ-\gamma} \sim \frac{e^{-\gamma}}{K^2} \tag{50}$$

$$n = \sum e^{-KZ-\gamma} \sim \frac{e^{-\gamma}}{K} \tag{51}$$

from which:

$$n_Z = \frac{n^2}{Z_0} e^{-\frac{nZ}{Z_0}}. \tag{52}$$

This expression has the correct asymptotic structure for $T \to \infty$ required by Eq. (42). The significance of this form is transparent: First, the overall scale for the fragment

size is set by the total charge Z_0. Second, for a specific multiplicity n, the scale is reduced by a factor n to the value Z_0/n.

Thus the offset introduced in Eq. (42) with increasing the multiplicity n may just be due to this scale reduction. If this is so, the quantity c in Eq. (42) takes the meaning $c = 1/Z_0$. The empirical value from Fig. 25 is $c \approx 0.016$ which corresponds to a value of $Z_0 \approx 60$.

However, our analysis is not directly comparable to the Euler solution (Eq.(52)) since we have restricted ourselves to a limited region ($3 \leq Z \leq 20$) for our study of the IMF multiplicity dependence of the charge distributions. Furthermore, Eq. (52) and the associated dependence of c upon Z_0 are characteristic of a one-dimensional percolation model. We therefore caution that, while c may indeed reflect the size of the emitting source, the strict equality of $c = 1/Z_0$ may not be valid. We return to this problem in Sec. 6.4.

The implications of the experimental evidence presented above are far reaching. On the one hand, the thermal features observed generally in multifragmentation (thermal population of bound and unbound [43–45] excited states and slope parameters of Maxwell-Boltzmann velocity spectra [46]) and specifically in the n-fragment emission probabilities, extend consistently to the charge distributions, and strengthen the hypothesis of phase space dominance in multifragmentation. On the other hand, the reducibility of the n-fold-event charge distributions to that of the singles distribution highlights the near independence of individual fragment emission, limited only by the constraint of charge conservation.

6 Phase Transitions, Phase Coexistence, and Charge Distributions

Since the early studies of complex fragment emission at intermediate energies [47–52], a "liquid vapor phase transition" had been claimed as an explanation for the observed power law dependence of the fragment charge distribution. The basis for such claims was the Fisher droplet theory [53] which was advanced to explain/predict the clusterization of monomers in vapor. According to this theory, the probability of a cluster of size m is given by:

$$P(m) \propto \exp\left[\frac{-(\mu_L - \mu_V)m}{kT}\right] m^{-\tau} \exp\left[-\frac{c_s m^{2/3}}{kT}\right] \tag{53}$$

where μ_L, μ_V are the liquid and vapor chemical potentials, τ is the Fisher critical exponent, and c_s is the surface energy coefficient for the liquid. For $\mu_V > \mu_L$ the liquid phase is stable and large clusters are found. For $\mu_V < \mu_L$ the vapor is stable and small clusters are present. At the critical temperature the liquid-vapor distinction ends, $\mu_L = \mu_V$ and the surface energy coefficient vanishes. The cluster size distribution assumes a characteristic power law dependence.

It was soon realized that power law dependences could be easily generated in more mundane environments. On the other hand, a recent analysis of very detailed experiments has claimed not only the demonstration of a near critical regime, but also the determination of other critical coefficients [54] besides τ. Because a detailed description of this analysis would take us far afield, regretfully we must abandon this subject.

However, another recent announcement claiming the discovery of a 1st order phase transition associated with multifragmentation [55] has created a strong resonance. Because of the greater simplicity inherent to this subject, and because of its relevance to some of our work reported below, we discuss it here in some detail.

This study [55] claims to have determined the "caloric curve" (sic) of a nucleus, namely the dependence of nuclear temperature on excitation energy. The temperature is determined from isotopic ratios (e.g. ^{3}He/^{4}He, ^{6}Li/^{7}Li) [56], while the excitation energy is determined through energy balance. Details about these determinations and their possible pitfalls [57–59] will not be discussed here. The highlight of this measurement is the discovery of a plateau, or region of constant temperature, which, in the authors' view, is indicative of a 1st order phase transition from the liquid to the vapor phase.

Apparently, the "paradigm" the authors have in mind is a standard picture of the diagram of temperature T versus enthalpy H for a one component system at *constant pressure* P. In this diagram, the temperature of the liquid (no vapor is present yet!) rises until the vapor pressure p matches the external pressure P. From this point on, the vapor appears and the temperature remains constant until the liquid has completely evaporated. After the liquid has disappeared, the temperature of the (now overheated) vapor can rise again.

It is not clear whether the experimental curve [55] can be interpreted in terms of equilibrium thermodynamics [60]. If this is the case, however, several problems arise. For instance, the claimed distinction between the initial rise (interpreted as the fusion-evaporation regime) and the plateau (hinted at as the liquid-vapor phase transition) is not tenable, since evaporation *is* the liquid-vapor phase transition and no thermodynamic difference exists between evaporation and boiling.

Furthermore, the "caloric curve" requires for its interpretation an additional relationship between the variables T, P, and V. More to the point, the plateau is a very specific feature of the constant pressure condition, rather than being a general indicator of a phase transition. For instance, a constant-volume liquid-vapor phase transition is *not* characterized by a plateau but by a monotonic rise in temperature. This can be easily proven by means of the Clapeyron equation, which gives dP/dT along the univariance line (liquid-vapor transition) together with the ideal-gas equation for the vapor.

For the nearly ideal vapor phase ($P = nT$), we write:

$$dP = Tdn + ndT \tag{54}$$

where n is the vapor molar density. In order to stay on the univariance line, we need the Clapeyron equation:

$$\frac{dP}{dT} = \frac{\Delta H}{T\Delta V} \tag{55}$$

where ΔH is the molar enthalpy of vaporization and ΔV is the molar change in volume from liquid to gas. From this we obtain:

$$n\,(\Delta H - T)\,dT = T^2 dn. \tag{56}$$

At constant pressure, dn=0, so dT=0. For $dn > 0$, we see immediately that $dT > 0$. Using $dE \approx dn\Delta E$, where ΔE is the molar heat of vaporization at constant volume, we finally obtain:

$$\left.\frac{\partial T}{\partial E}\right|_V \approx \frac{T^2}{n\Delta E^2} = \frac{1}{n\Delta S^2}. \tag{57}$$

The positive value of this derivative shows that the phase transition at constant volume is characterized by a monotonic increase in temperature.

As an example, Fig. 27 shows a standard temperature T versus entropy S diagram for water vapor. The region under the bell is the phase coexistence region. For the constant pressure curves ($\Delta S = \Delta H/T$), the initial rise along the "liquid" curve is associated with pure liquid, the plateau with the liquid-vapor phases, and the final rise with overheated vapor. The constant volume curves ($\Delta S = \Delta E/T$), however, cut across the coexistence region at an angle, without evidence for a plateau.

Thus the reminiscence of the observed "caloric curve" with "the paradigm of a phase transition" may be more pictorial than substantive, and indicators other than the plateau may be needed to substantiate a possible transition from one to two phases. More specifically, *an additional relationship* between the three variables P, T, V (like P=const, or V=const, etc.) *is needed to interpret a T-E diagram unequivocally.*

6.1 Triviality of 1st order phase transitions

The great attention to the alleged discovery of 1st order phase transition in nuclei would suggest that such a phenomenon may be of great significance to our understanding of nuclear systems. Nothing could be further from the truth. In fact, it is easy to show that 1st order phase transitions are completely trivial [61]. Here are the reasons:

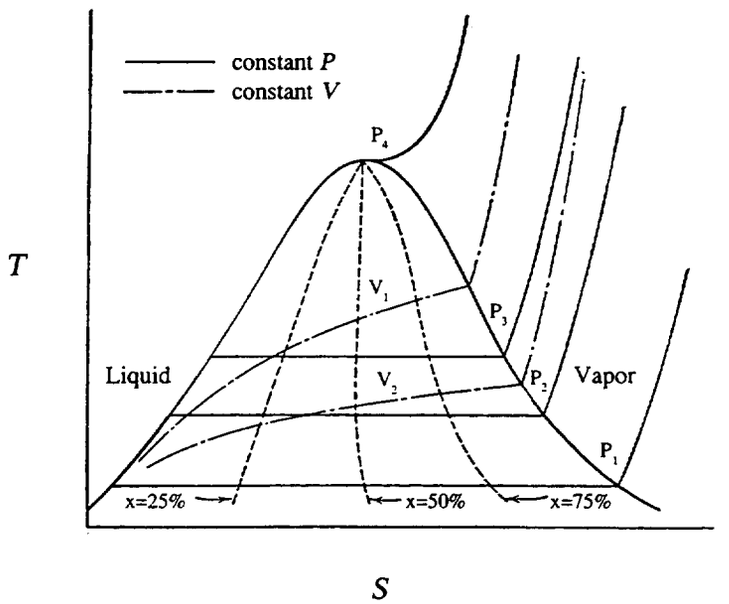

Fig. 27. Temperature-entropy diagram for steam. Curves are shown for constant pressure ($P_4 > P_3 > P_2 > P_1$), constant volume ($V_1 < V_2$) and constant percentage in the gas phase (dashed lines).

1)If there are two or more phases known, or even hypothetically describable, then there will be 1st order phase transitions.

2) The thermodynamics of these transitions is *completely* determined by the thermodynamical properties of each individual isolated phase. These phases do not affect each other, and do not need to be in contact.

As an example, let us consider Fig. 28, where the molar free energy F at constant T is plotted versus the molar volume for the liquid and gas phases. Stability of each phase requires that each of these curves be concave. The very existence of these two concave curves implies that in the region between the points of contact of the common tangent, the free energy is minimized by apportioning the system between the liquid and gas phases. Each phase is defined at the point of tangency, and the segment of the tangent between the two points is the actual free energy of the mixed phase. The slope of the common tangent is the negative of the constant pressure at which the transition takes place. The coexistence region is completely defined by the properties of the liquid at V_L^M and and of the gas at V_G^M. Furthermore, since the liquid is highly incompressible, the point of tangency is near the absolute minimum of F_L. Consequently, it is irrelevant whether the liquid is in contact with the vapor

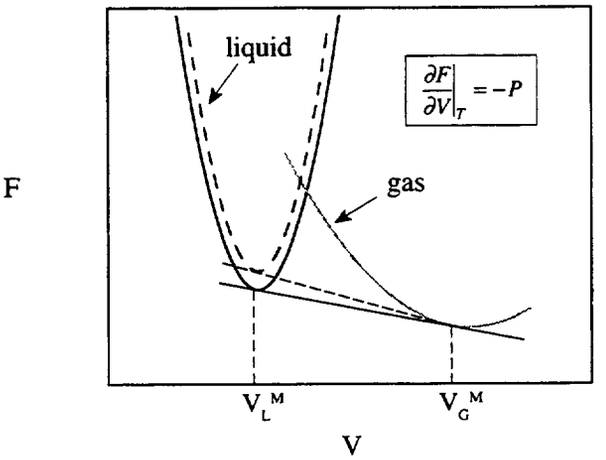

Fig. 28. The free energy as a function of molar volume for a liquid and gas. The dashed lines refer to a drop rather than to bulk liquid.

or not!

This discussion applies to infinite phases. However, it is simple to introduce finite size effects, e.g. surface effects.

The Clapeyron equation is:

$$\frac{dP}{dT} = \frac{\Delta H_m}{T \Delta V_m} \tag{58}$$

where P is the vapor pressure, T is the temperature, ΔH_m is the molar enthalpy of vaporization, and ΔV_m is the corresponding change in molar volume. We can write:

$$\Delta H_m = \Delta H_m^0 - c_s S_m = \Delta H_m^0 - 3\frac{c_s V_m}{r} \tag{59}$$

where c_s is the surface energy coefficient, S_m is the molar surface of the drop of liquid, V_m is the molar volume, and r is the radius of the droplet.

Integrating the Clapeyron equation we obtain:

$$P = P_0 \exp\left[-\frac{\Delta H_m}{T}\right] = P_{\text{inf}} \exp\left[\frac{3c_s V_m}{rT}\right] \tag{60}$$

where P_{inf} is the vapor pressure of the infinite liquid. Since the pressure of a drop is always greater than that of the infinite liquid, the common tangent (dashed line, Fig. 28) becomes steeper, in accordance with the increased free energy of the liquid.

Any good textbook of statistical mechanics contains the demonstration that, in the thermodynamic limit, all ensembles are equivalent, i.e. they give the same thermodynamic functions.

In dealing with phase transitions in finite systems, one may question whether this equivalence is retained. Let us review the connection between, for instance, the Microcanonical and the Canonical Ensemble.

Let $\rho(E)$ be the microcanonical level density. The corresponding canonical partition function is the Laplace transform:

$$Z(\beta) = \sum e^{-\beta E_i} \approx \int \rho(E) e^{-\beta E} dE. \tag{61}$$

The partition function is usually easier to calculate than the level density. However, the latter can be obtained from the former through the inverse Laplace transform:

$$\rho(E) = \frac{1}{2\pi i} \oint Z(\beta) e^{\beta E} d\beta. \tag{62}$$

The integral can be evaluated by the saddle point approximation:

$$\rho(E) = \frac{1}{2\pi i} e^{\ln Z_0 + \beta_0 E} \int e^{-\frac{1}{2} \frac{\partial^2 \ln Z}{\partial \beta^2}\Big|_{\beta_0} (\beta - \beta_0)^2} i d(\beta - \beta_0) = \frac{\exp(\ln Z_0 + \beta_0 E)}{\left(2\pi \frac{\partial^2 \ln Z}{\partial \beta^2}\Big|_{\beta_0}\right)^{1/2}}. \tag{63}$$

We can write Eq. (63) as:

$$S_{\text{Micro}} = \ln \rho(E) = \ln Z_0 + \beta_0 E - \frac{1}{2} \ln \left(2\pi \left. \frac{\partial^2 \ln Z}{\partial \beta^2} \right|_{\beta_0} \right) \tag{64}$$

where β_0 corresponds to the stationary point of the integrand. Furthermore,

$$S_{\text{Micro}} = S_{\text{Can}} - \ln \left(2\pi \left. \frac{\partial^2 \ln Z_0}{\partial \beta^2} \right|_{\beta_0} \right). \tag{65}$$

The first term to the right is of order N while the second is of order $\ln N$.

When N goes to infinity (thermodynamic limit), one can disregard the term of order $\ln N$. For finite N one can easily evaluate the correction term which turns out to be very accurate even for small N. For instance, consider a percolation system with N bonds of which n are broken. The microcanonical level density can be calculated directly:

$$\rho = \frac{N!}{n!(N-n)!}. \tag{66}$$

The inverse Laplace transform yields:

$$\rho = \frac{N^N}{(N-n)^{N-n}n^n} \Big/ \left(2\pi \frac{n(N-n)}{N}\right)^{1/2}. \tag{67}$$

As an example of a finite system, let us take N=6 and n=3. The exact expression yields ρ=20. The saddle point approximation yields ρ=20.6. One can see that with little additional effort one can retain the use of the partition function with little loss of accuracy even for the smallest systems!

Still, in the mind of some physicists there is the bias that a microcanonical approach, or its equivalent through the inverse Laplace transform of the partition function, is more correct than the canonical approach because the former conserves energy, while the latter does not.

In fact the microcanonical distribution is given by:

$$P(E) = \delta\left(E(p,q) - E_0\right). \tag{68}$$

The canonical distribution instead is given by:

$$P(E) = Ke^{-\beta E(p,q)}. \tag{69}$$

In this case, there are energy fluctuations.

So, which is ultimately the "right" ensemble? If it does not matter, as in the the thermodynamic limit, the point is moot. But for finite systems it matters. However, consider the case of a small system which is a part of a larger system. Let us call the total energy E and that of the small system ϵ. Then

$$\begin{aligned} S(E,\epsilon) &= S(E,0) + \left.\frac{\partial S}{\partial \epsilon}\right|_{\epsilon=0} \epsilon + \ldots \\ &= S(E,0) - \frac{\epsilon}{T} + \ldots \end{aligned} \tag{70}$$

Thus,

$$\rho(E,\epsilon) \approx \rho(E,0)e^{-\epsilon/T}. \tag{71}$$

The energy of the small system is canonically distributed, in a real, physical sense. *The canonical, or grand canonical distribution very frequently has a direct physical reality and is not an approximation to a "more correct" microcanonical distribution.* For instance, Na clusters in thermal equilibrium with a carrier gas are canonically distributed in energy.

What is the relevance of the above to phase transitions? There are claims that a microcanonical approach yields "sharper" phase transitions than a canonical approach,

because of its lack of energy fluctuations. However, any thermodynamic property, including phase transitions, is defined in statistical mechanics as an ensemble average. *Thus the resulting properties are not properties of the system alone, but they are properties of the ensemble.* So with reference to phase transitions in particular, arguments like "the Microcanonical Ensemble yields sharper phase transitions compared to the Canonical Ensemble, and because of that it is better" are meaningless. If the *physical* ensemble is canonical, the canonical description is the correct one, irrespective of whether it is sharper or fuzzier than the microcanonical description.

6.3 Sharpness of phases and phase transitions

Let us consider the free energy of the liquid phase in Fig. 28. We can expand about the minimum as follows:

$$F = F_0 + \frac{1}{2}\left.\frac{\partial^2 F}{\partial V^2}\right|_{\widehat{V}} (\Delta V)^2. \tag{72}$$

The probability of volume fluctuations are then:

$$P(V) \propto \exp\left[-\frac{(\Delta V)^2}{2\sigma_V^2}\right] \tag{73}$$

where $1/\sigma_V^2 = \partial^2 F/\partial V^2|_{\widehat{V}}$. Since $F \propto N$, $\sigma_V^2 \propto 1/N$. Therefore important volume (density) fluctuations are to be expected at small N. A cluster, or a nucleus, which are not kept artificially at constant density, are going to fluctuate substantially in density.

At coexistence, the correlated fluctuations between the two phases make the sharpness of the phases and of the phase transition even more washed out.

6.4 A robust indicator of phase coexistence

As we have seen, a "generic" caloric curve of the kind obtained in Ref. [55] is of problematic interpretation because of the difficulty in establishing the additional relation $F(V, T, P)$ associated with the evolution of the system.

Nevertheless, the only meaningful experimental question about 1st order phase transitions is whether the system is present in a single phase, or there is phase coexistence. In thermodynamical language, we want to know whether the system is monovariant (two phases), or bivariant (one phase).

We have found a robust indicator for just these features in the charge distributions observed in multifragmentation.

Let us recall the "charge distribution" arising from the least biased fragmentation into n pieces of an integer Z_0 (Eq. (52)):

$$P(Z) \approx \frac{n^2}{Z_0} e^{-\frac{nZ}{Z_0}} = cn^2 e^{-cnZ}. \tag{74}$$

While this form obviously implies charge conservation, it is not necessary that charge conservation be implemented as suggested by Eq. (74). In fact it is easy to envisage a regime where the quantity c should be zero. Sequential thermal emission is a case in point. Since each fragment does not know how many other fragments will follow its emission, its charge distribution can not reflect the requirement of an unbiased partition of the total charge among n fragments. Let us consider, for instance, a liquid drop evaporating fragments of different size and binding energy. Charge conservation will affect the distribution minimally, unless evaporation consumes the entire system, and even then, not in the sense of an unbiased partition. A simulation in which fragments with different barriers are allowed to be emitted sequentially according to the binomial scheme of Ref. [29] yields indeed c=0 if a residue survives. Details of this simulation will be given in Sec. (8).

On the other hand, in a simultaneous emission controlled by a n-fragment transition state [26,27], fragments would be strongly aware of each other, and would reflect such an awareness through the charge distribution.

The question then arises whether $c = 0$, or $c > 0$, or even better, whether one can identify a transition from a regime for which $c = 0$ to a new regime for which $c > 0$. To answer this question, we have studied the charge distributions as a function of fragment multiplicity n and transverse energy E_t for a number of systems and excitation energies. Specifically, we will present data for the reaction ^{36}Ar+^{197}Au at E/A=80 and 110 MeV and the reaction ^{129}Xe+^{197}Au at E/A=50 and 60 MeV.

Several approaches can be used to extract c from the charge distributions [62]. If the charge distributions are exponential (as is sometimes the case, $P_n(Z) \propto e^{-\alpha_n Z}$), it is sufficient to extract from them the exponential coefficient α_n as we did in Sec. (5). From the n dependence of α_n, the quantity c is readily extracted [40]. A more general approach which does not depend on any specific form for the charge distribution is to construct at each E_t the ratio:

$$\frac{P_n(Z)}{P_{n+1}(Z)} \propto e^{cZ}. \tag{75}$$

A value of c can be extracted for each n by taking the log of this ratio and finding the slope of the resulting graph (see bottom panel of Fig. 29). A weighted average (over all IMF multiplicities n) for c can then be constructed at all E_t. Alternatively, a χ^2 can be constructed in terms of the differences in $F(Z)$ (see Eq. (43)) between any pairs of n values and minimized as a function of c. These procedures yield essentially the same results which are reported in Fig. 30 for the ^{129}Xe+^{197}Au and ^{36}Ar+^{197}Au reactions.

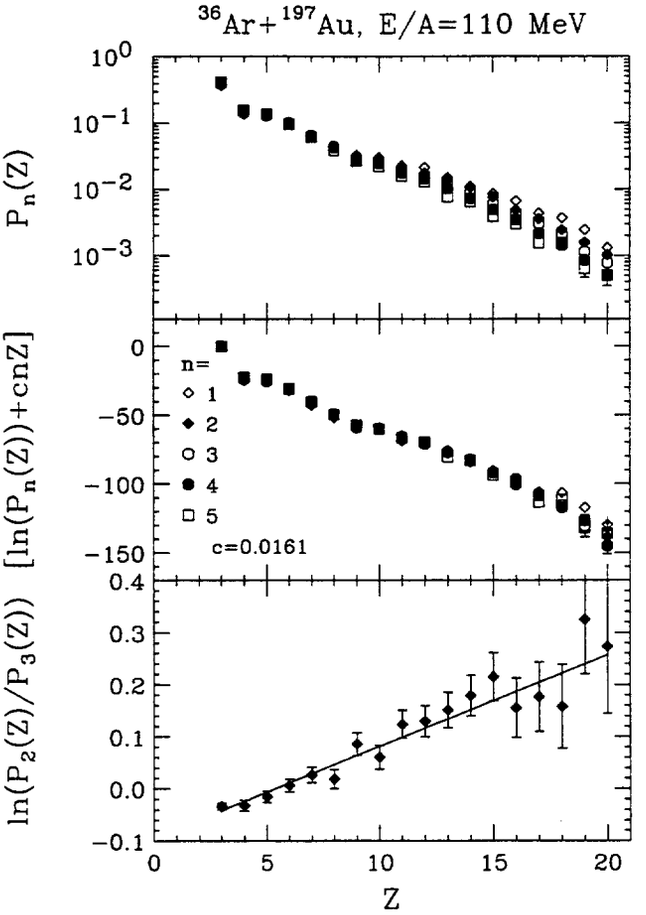

Fig. 29. Top panel: the n gated charge distributions $P_n(Z)$ for the reaction ^{36}Ar+^{197}Au at E/A=110 MeV. The charge distributions were constructed from events with E_t=650±20 MeV and n=1-5. Middle panel: the "reduced" charge distribution [40] for the same data using the indicated value of c. (The data here are normalized at Z=3). Bottom panel: the log of the ratio of $P_2(Z)/P_3(Z)$. The slope corresponds to c for n=2 (see Eq. (75)). The statistical error bars are shown for errors larger than the symbol size.

It is interesting to notice that for all reactions and bombarding energies the quantity c starts at or near zero, increases with increasing E_t for small E_t values, and seems to saturate to a constant value at large E_t.

This behavior can be compared to that of a fluid crossing from the region of liquid-vapor coexistence (univariant system) to the region of overheated and unsaturated vapor (bivariant system, see Fig. 31). In the coexistence region, the properties of the saturated vapor cannot depend on the total mass of fluid. The presence of the liquid phase guarantees mass conservation at all average densities for any given temperature. A change in mean density (volume) merely changes the relative amount of the liquid and vapor, without altering the properties of the saturated vapor. Hence the vapor properties, and, in particular, the cluster size distributions cannot reflect the total mass or even the mean density of the system. In our notation, $c = 0$.

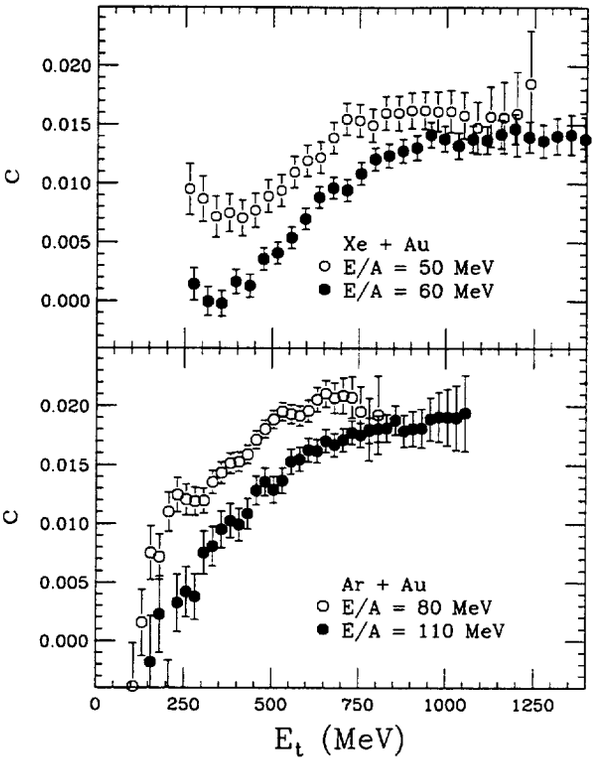

Fig. 30. Plots of the coefficient c versus E_t for the reactions ^{129}Xe+^{197}Au at E/A=50 and 60 MeV (top panel) and ^{36}Ar+^{197}Au at E/A=80 and 110 MeV (bottom panel). The error bars are statistical.

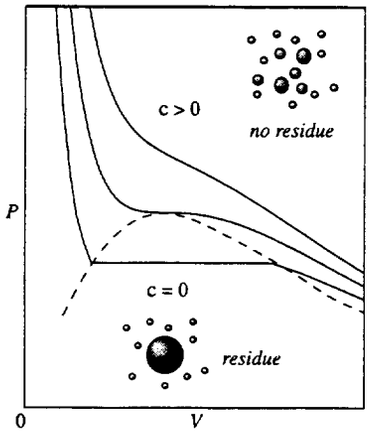

Fig. 31. Liquid-gas phase diagram. The top of the dashed line is the critical point. The area below the dashed line ($c = 0$) is the region where mixtures of the liquid and gas phases coexist.

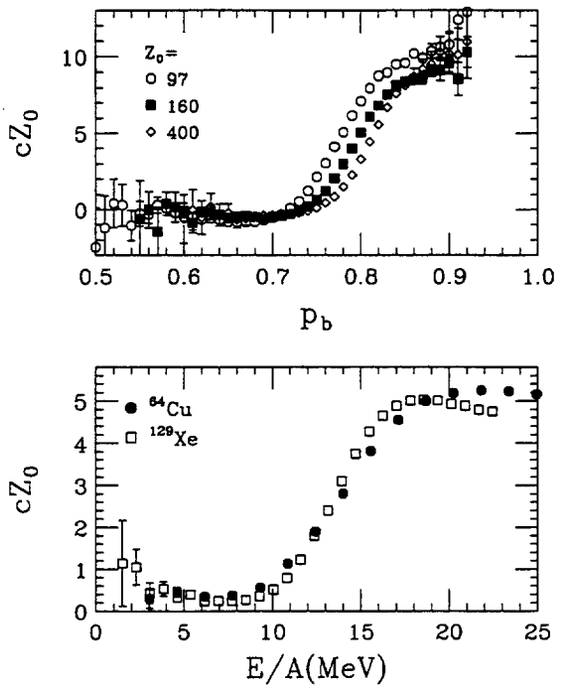

Fig. 32. top: A plot of cZ_0 versus the percentage of broken bonds p_b from a percolation calculation [64] for three systems Z_0=97 (circles), Z_0=160 (squares) and Z_0=400 (diamonds). bottom: A plot of cZ_0 versus excitation energy per nucleon from a binomial evaporation calculation [63] for ^{64}Cu and ^{129}Xe. The statistical error bars are shown for errors larger than the symbol size.

On the other hand, in the region of unsaturated vapor, there is no liquid to insure mass conservation. Thus the vapor itself must take care of this conservation, at least grand canonically. In our notation, $c > 0$. In other words we can associate $c = 0$ with thermodynamic univariance, and $c > 0$ with bivariance.

These considerations lead to the immediate identification: $c \propto (\mu_L - \mu_V)$ in the Fischer model [53], where μ_L and μ_V are the chemical potentials of the liquid and the vapor respectively. Thus, in the coexistence region ($\mu_L = \mu_V$) $c = 0$ while for the overheated vapor ($\mu_V < \mu_L$), $c > 0$.

To test these ideas in finite systems, we have considered a finite percolating system and a system evaporating according to a thermal binomial scheme [29,63]. Percolation calculations [64] were performed for systems of Z_0=97, 160 and 400 as a function of the percentage of bonds broken (p_b). Values of c were extracted (using Eq. (75)) as a function of p_b.

The results are shown in Fig. 32. Guided by the insight gleaned from the approximate solution to Euler's problem (see Eq. (74)) we have scaled the extracted values of c by the source size Z_0 in order to remove this leading dependence and to evidentiate the true finite size effects. For values of p_b smaller than the critical (percolating) value ($p_b^{crit} \approx 0.75$ for an infinite system), we find $c = 0$. This is the region in which a

large (percolating) cluster is present. As p_b goes above its critical value, the value of c increases, and eventually saturates in a way similar to that observed experimentally.

Notice that although the phase transition in the infinite system is second order at $p = p_c$, here the region for which $c = 0$ mimics a first order phase transition.

Before proceeding, let us remind ourselves that charge conservation is *not* a finite-size effect. For instance, the chemical potential, introduced in statistical mechanics to conserve mass, survives the thermodynamic limit and retains its meaning for an infinite system, despite the fact that the extensive thermodynamic quantities go to infinity. In our case, while it is true that c goes to zero or that $1/c$ goes to infinity, it is also true that the product cZ_0 tends to a finite limit nearly independent of Z_0.

Our analysis is not directly comparable to the Euler solution (Eq. (74)) since we have restricted ourselves to a limited region ($3 \leq Z \leq 20$) of the total charge distribution for our study of how the source is partitioned into different IMF multiplicities (see Appendix A). Furthermore, Eq. (74) and the associated dependence of c upon Z_0 are characteristic of a one-dimensional percolation model. Therefore, it is not unexpected that c appears to be proportional, but not equal, to $1/Z_0$ in the three-dimensional percolation calculation reported in Fig. 32.

An evaporation calculation was also carried out for the nuclei ^{64}Cu and ^{129}Xe according to the thermal binomial scheme [29,63]. The only constraint introduced was to prevent at every step the emission of fragments larger than the available source. The resulting charge distributions are well reproduced by Eq. (43). The extracted quantity cZ_0 is plotted in the bottom panel of Fig. 32 as a function of excitation energy per nucleon. In both cases cZ_0 goes from 0 to a positive finite value (equal for both nuclei) as the energy increases. The region where $c = 0$ is readily identified with the region where a large residue survives. On the other hand, when $c > 0$ there is no surviving residue.

These results are in striking agreement with those obtained for percolation. For both kinds of finite systems, the univariant regime ($c = 0$) is associated with the presence of a residue, while the bivariant regime ($c > 0$) with the absence of a residue.

7 Reducibility, Thermal and Mass Scaling in Particle-Particle Angular Correlations

The multifragmentation scenario painted so far is that of a process controlled by a largely independent emission of individual fragments, which, in turn, is dominated by phase space.

We will show that, except at small angles, the particle-particle angular correlations

and their dependence on excitation energy are also interpretable in terms of a nearly independent emission of particles whose angular distributions are controlled by phase space. In other words the angular correlations are also *reducible* and *thermally scalable.*

The evidence presented here illustrates the role in multifragmentation of the angular momentum, a variable not yet explored either experimentally or theoretically in this context.

In pursuit of these ideas, we have explored the azimuthal correlations between emitted particles [65–74] defined by the ratio:

$$\left.\frac{Y(\Delta\phi)}{Y'(\Delta\phi)}\right|_{\theta,E_t} = C\,[1 + R(\Delta\phi)]|_{\theta,E_t}\,. \tag{76}$$

Here, $Y(\Delta\phi)$ is the coincidence yield of two particles emitted with relative azimuthal angle $\Delta\phi$ at a polar angle θ, and selected by a specific cut on the total transverse energy of an event E_t; $Y'(\Delta\phi)$ is the background yield constructed by mixing particle yields from different coincidence events selected by identical cuts on E_t and θ; C is a normalization constant chosen so that the yields of Y and Y' integrated over $\Delta\phi$ are equal. All azimuthal correlation functions were constructed from particles detected at $\theta = 31°$-$50°$. Software energy thresholds of E_{th}/A=3 MeV were applied to all particles [75]. Pairs of particles extending from protons to carbons were considered.

Fig. 33 shows azimuthal correlation functions of different particle pairs (symbols) detected for four windows of E_t (columns) from the reaction ^{36}Ar+^{197}Au at E/A=50 MeV (details of the experiment can be found in Ref. [73]). The azimuthal correlation functions exhibit a slightly distorted V-shape pattern with a clear minimum at $\Delta\phi \approx 90°$. At larger excitation energies (assumed proportional to E_t), the correlations become progressively damped. In addition, the correlations are stronger for the more massive particles.

In an effort to understand the evolution of the correlation functions of Fig. 33, we have considered the exactly solvable problem of thermal particle emission from a rotating source. The classical probability of emitting a particle with reduced mass μ from the surface of a rotating system (of angular momentum I, moment of inertia $\Im$, temperature T and distance R between the two centers of the "daughter" and emitted nuclei) in a direction given by polar angle θ (in the center of mass frame) and azimuthal angle ϕ (measured with respect to the reaction plane perpendicular to $\vec{I}$) is [76]:

$$P(\theta,\phi) \propto \exp\left[-\beta \sin^2\theta \sin^2\phi\right] \tag{77}$$

where

$$\beta = \frac{\hbar^2 I^2}{2\Im T}\frac{\mu R^2}{(\Im + \mu R^2)} = \frac{E_{rot}}{T}\frac{\mu R^2}{(\Im + \mu R^2)} \tag{78}$$

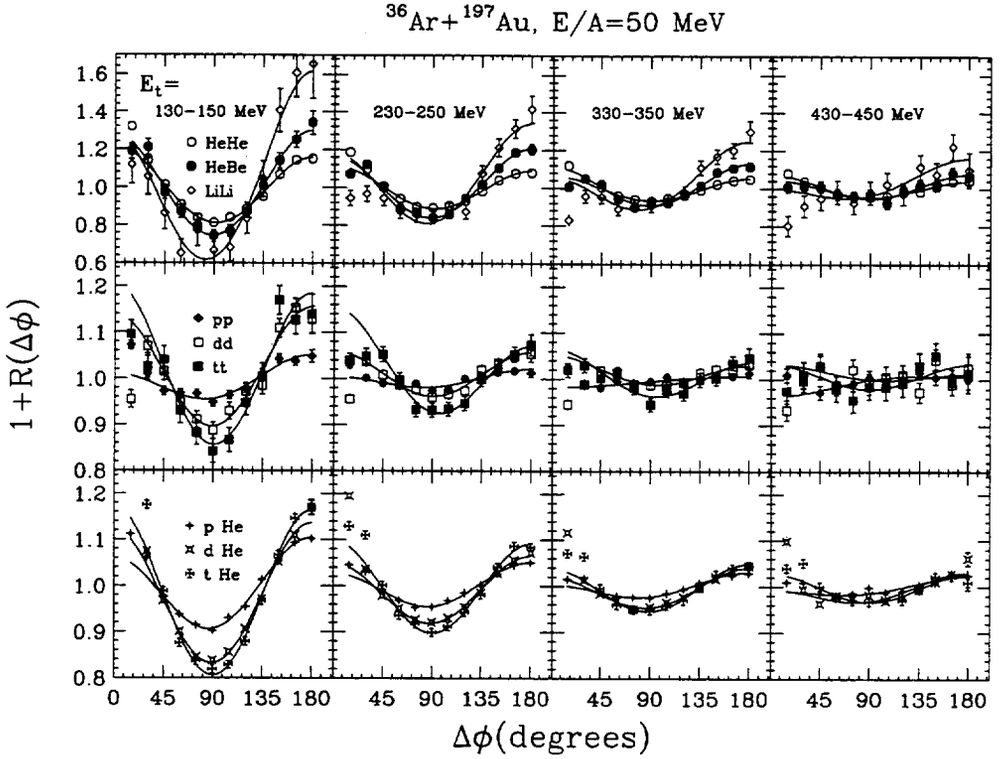

Fig. 33. Evolution of the azimuthal correlation functions of two particles (symbols) emitted at θ_{lab} = 31°-50° for four different cuts on the transverse energy E_t (columns) from the reaction ^{36}Ar+^{197}Au at E/A=50 MeV. The solid lines are fits of the form given in Eq. (87). The error bars are statistical.

and E_{rot} is the rotational energy of the source.

The singles distribution of Eq. (77) comes from an extension of the angular distributions for fission [76]. As in fission, particle emission in the angular momentum frame follows:

$$P(\psi) \propto e^{-\frac{\mathcal{E}_{rot}(K)}{T}}, \tag{79}$$

where $K = I\cos\psi$ is the projection of I on the separation axis of the scission configuration (ψ is the angle between $\vec{K}$ and $\vec{I}$), and

$$\mathcal{E}_{rot} = \frac{I^2 - K^2}{2\Im_\perp} + \frac{K^2}{2\Im_{||}} \tag{80}$$

with $\Im_\perp = \Im_r + \mu R^2$ and $\Im_{||} \approx \Im_r$. A straightforward transformation of Eq. (79) into a frame where the z-axis coincides with the beam direction (so that a particle's direction is specified by polar angle θ and azimuthal angle ϕ) gives Eq. (77).

The use of Eq. (77) requires the prior knowledge of the reaction plane (ϕ in Eq. (77) is measured with respect to the reaction plane). The uncertainties in the reaction plane determination can be rather large [74,77,78]. In order to avoid this uncertainty

[74,78], we use the azimuthal correlation function (Eq. (76)) which is proportional to the joint probability of observing two particles at a fixed relative angle.

If the fragments are emitted independently of one another, the joint probability of observing two particles at a given polar angle θ and different azimuthal angles ϕ and $\phi + \Delta\phi$ is $P(\theta, \phi, \Delta\phi) = P(\theta, \phi)P(\theta, \phi + \Delta\phi)$. The resulting probability distribution must be averaged over the different directions of $\vec{I}$ arising from different orientations of the impact vector. Averaging over the direction of $\vec{I}$ is equivalent to integrating over ϕ:

$$P(\theta, \Delta\phi) \propto \int_0^{2\pi} d\phi e^{-\beta \sin^2\theta \sin^2\phi} e^{-\beta \sin^2\theta \sin^2(\phi+\Delta\phi)}. \tag{81}$$

This integral can be performed exactly, and one finds:

$$P(\theta, \Delta\phi) \propto I_0\left(\beta \sin^2\theta \sqrt{\frac{1+\cos 2\Delta\phi}{2}}\right) \tag{82}$$

where I_0 is the modified Bessel function of zeroth order.

These equations, which hold for like particles, can be generalized to unlike particles:

$$P(\theta, \Delta\phi) \propto I_0\left(\frac{\sqrt{\beta_1^2+\beta_2^2}}{2} \sin^2\theta \sqrt{1+\frac{2\beta_1\beta_2}{\beta_1^2+\beta_2^2}\cos 2\Delta\phi}\right) \tag{83}$$

where β_1 and β_2 are calculated via Eq. (78) for particles of reduced mass μ_1 and μ_2, respectively.

It is useful to consider the Taylor expansion of $I_0(z)$:

$$I_0(z) = 1 + \frac{\frac{1}{4}z^2}{(1!)^2} + \frac{\left(\frac{1}{4}z^2\right)^2}{(2!)^2} + \frac{\left(\frac{1}{4}z^2\right)^3}{(3!)^2} + \ldots \tag{84}$$

For small z we can keep only the first three terms of the expansion and find that the joint probability (for $\beta_1 = \beta_2 = \beta$) is:

$$P(\theta, \Delta\phi) \propto 1 + \frac{D}{1+D/2}\cos 2\Delta\phi + \frac{D^2}{(D+2)^2}\cos^2 2\Delta\phi = \tag{85}$$

$$= 1 + \lambda_2 \cos 2\Delta\phi + \lambda_4 \cos^2 2\Delta\phi \tag{86}$$

where $D = (\beta^2 \sin^4\theta)/8$.

The first two terms of Eq. (85) have the familiar form of $1 + \lambda_2 \cos 2\Delta\phi$ often used to describe rotational features of azimuthal correlations [73,74,79]. Positive values of λ_2 produce the V-shaped signature of the data in Fig. 33. The third term can

be considered a small perturbation to the general shape of the correlation function dominated by λ_2 (for $D \leq 0.5, \lambda_4 \ll \lambda_2$). Generally a term $\lambda_1 \cos\Delta\phi$ is also included in the fit to describe either the kinematic focusing from a recoiling source ($\lambda_1 < 0$) or directed flow effects ($\lambda_1 > 0$) in the azimuthal correlations [74,79].

Fits of the form:

$$P(\theta, \Delta\phi) \propto N\left(1 + \lambda_1 \cos\Delta\phi + \frac{D}{1+D/2}\cos 2\Delta\phi + \frac{D^2}{(D+2)^2}\cos^2 2\Delta\phi\right) \qquad (87)$$

are demonstrated by the solid lines in Fig. 33. Equivalent fits are produced if one uses the Bessel function I_0 instead of its approximation in Eq. (87). The fits have been limited to $\Delta\phi \geq 45°$ in an effort to remove the sensitivity of the fit parameters to strong resonances ($^8\mathrm{Be} \rightarrow 2\alpha$) and to the Coulomb repulsion between the particle pair. Both may strongly affect the correlation in the region of small $\Delta\phi$. The above functional form well describes the shape of the correlations. Extracted values of λ_1 are small, typically a factor of ten smaller than the values of D, and show no strong dependence on E_t [73]. The quality of the fits using Eq. (87) is sufficiently good that the parameters λ_1 and D may be used to characterize the main features of the evolution of the azimuthal correlations with increasing excitation energy.

According to Eq. (78), the parameter D is predicted to have a specific temperature dependence:

$$D \propto \beta^2 \propto \left(\frac{E_{rot}}{T}\right)^2 \mu^2 \qquad (88)$$

which can be explored in this data set. Assuming as usual that the transverse energy E_t is proportional to the excitation energy, one expects $D \propto 1/T^2 \propto 1/E_t$.

A plot of D as a function of $1/E_t$ is given in the left panel of Fig. 34 for identical particles. The correlations are remarkably linear. We are not limited in this analysis to particle pairs of equal mass (see Eq. (83)). The right panel of Fig. 34 shows D as a function of $1/E_t$ for particle pairs of different masses (one member of the pair is a He nucleus). The thermal scaling is evident for all cases.

The simplest explanation for the observed linear behavior is that the fragmenting system attains an average angular momentum which is largely independent of E_t. While this assumption is not intuitive, it is supported by the constant slope Arrhenius plots shown in Sec. 4. The slopes of the Arrhenius plots are proportional to the effective barrier for fragment emission, and are found to be independent of E_t. This may indicate that collective rotation does not change significantly with E_t.

While this is the simplest explanation, the observed linear trends of Fig. 34 could instead come from a more complicated dependence of the rotational energy E_{rot} and of the temperature T on E_t. The observation of a finite intercept (the data do not

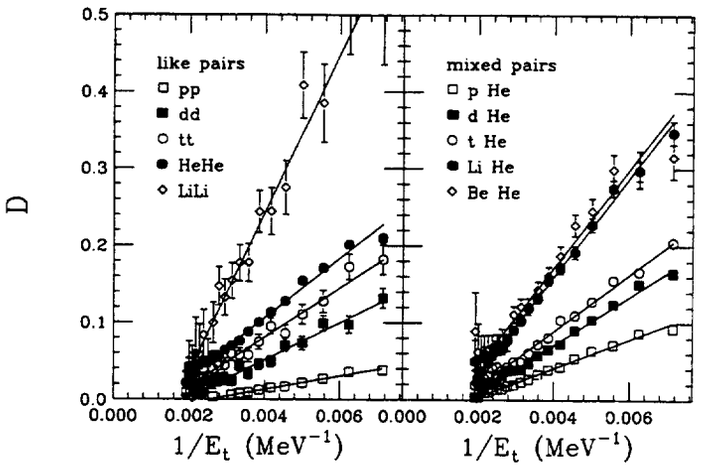

Fig. 34. Mass and "temperature" dependence of D. Left panel: The fit parameter D as a function of $1/E_t(\propto 1/T^2)$ for the indicated identical particle pairs. Solid lines are linear fits to the data. Right panel: Same as left panel but for particle pairs of different masses.

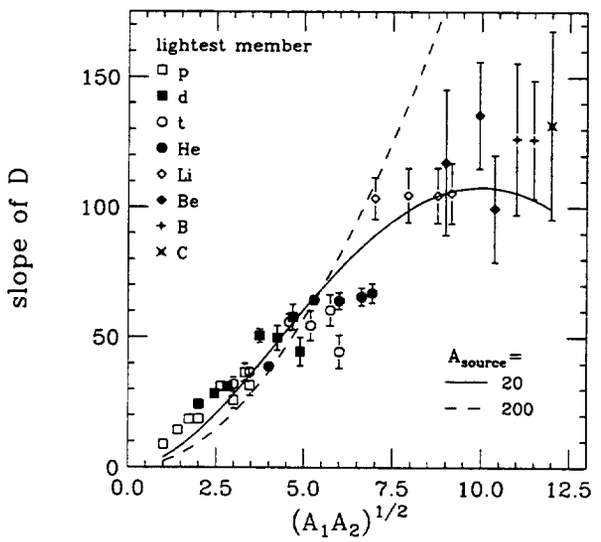

Fig. 35. Slope of D (see Fig. 34) as a function of $\sqrt{A_1 A_2}$ for particles with mass numbers between 1 and 12. The most abundant isotope in the periodic table is assumed for the mass numbers of the indicated elements. The lightest member of the particle pair is indicated by the different symbols. The solid (dashed) line is a prediction of the mass scaling assuming emission from a source of size A_{source}=20 (200).

extrapolate to zero at large E_t) indicates the presence of open questions with regard to this effect.

The strength of the correlation in Fig. 34 increases with increasing mass of the particle pair. This is consistent with previous observations [67–71,73,77,80–83] where the azimuthal anisotropies (as measured in this work by the parameter D) show a strong dependence on the mass of the emitted particles.

According to Eq. (88) one would expect the quantity D to have a μ^2 dependence (for identical particles) on the mass of the emitted particles. For a sufficiently massive source, $\mu^2 \sim A^2$ (see the dashed curve of Fig. 35). Instead, we observe a nearly linear scaling with A. This scaling is demonstrated nicely in Fig. 35 where we have plotted the extracted slopes from Fig. 34 as a function of the geometric mean of the mass numbers of the emitted particles [84]. We have also included data for all mass combinations ranging from protons to carbon nuclei. These data show a nearly linear dependence on $\sqrt{A_1 A_2}$ (as opposed to $\propto A_1 A_2$).

One possible way of resolving this contradiction is to assume that the mass of the emitting source(s) is small, of the order of $A_{source} \approx$ 15-30. In this case μ^2 is approximately linear with the mass of the emitted fragment in the mass range considered here. The solid curve shown in Fig. 35 is calculated assuming A_{source}=20.

It is important to point out that such a tantalizing explanation requires *multiple* sources of size A_{source}, all co-rotating (rigidly) with the same angular velocity. A *single* small source would give rise to strong recoil effects (the correlations would be suppressed at $\Delta\phi = 0°$ and enhanced at $\Delta\phi = 180°$), washing out the V-like signature in the azimuthal correlations [68].

In this regard it is interesting to notice that a variety of instabilities, like the Rayleigh instability relevant to the rupture of neck-like structures [85,86], or the sheet instability associated with disk-like objects [13], or even the spinodal instability [87], predict the early formation of several small fragments. A recent calculation [87] demonstrates that a spinodal breakup would produce several excited primary fragments of nearly equal size (Z=10-20) which then undergo statistical sequential decay. The observed mass scaling (Fig. 35) is consistent with such a prediction and may be a surviving signature of such dynamical processes.

Part B

8 Binomial and Poisson Monte Carlo Simulations

8.1 Motivation

The detailed accuracy and broad applicability of the binomial distribution to the IMF emission probabilities is striking, and gives significant insight into the nature of multifragmentation. Reducibility of the n-fold emission probability means that all the physics controlling P_n is contained in the quantities p and m. This, in turn, implies that multifragmentation itself is empirically reducible to a combination of nearly independent fragment emissions.

As discussed earlier, one possible physical interpretation is sequential decay with constant probability p. In this description, the number of trials in the binomial distribution (m) can be interpreted as the number of chances the system has to emit a fragment. Alternative scenarios can be thought of, such as a chain of m links with probability p that any of the links is broken, or a simultaneous statistical decay as in Ref. [88].

However, before venturing too far into theoretical speculations, it is necessary to clarify a number of issues directly related to binomiality, as well as answer a number of technical questions connected to the experimental observations.

- The linearity of the Arrhenius plot implies the thermal behavior of p (Eq. (30)), and that information on the effective emission barrier can be extracted from its slope. In Sec. 4.8.1 we have argued that a single effective barrier is expected, since the average p is dominated by the lightest fragment with the lowest barrier (see Eq. (28)). How good is this approximation? Can one extract experimental barriers through this procedure?
- Reducibility and thermal scaling are inferred from the reduction of experimental IMF excitation functions. Can the analysis be affected by detection of residue-like spectators misidentified as true reaction products?
- Are the observations of thermal scaling and reducibility affected by the physical constraints of charge and mass conservation, which come into play when the source of fragment emission is small?
- Are multiple sources of fragments consistent with binomiality? What is the meaning of a linear Arrhenius plot when multiple sources are present?

Other general technical issues, connected with these physical problems, include:

- The Arrhenius plot establishes a relationship between the elementary single-fragment emission probability p and the temperature of the source. Experimentally, however, the temperature has to be determined indirectly by measuring quantities related to the excitation energy, such as the transverse energy E_t [89]. Even though a linear correlation has been demonstrated between ϵ^* (as determined from the kinematically-reconstructed source velocity) and E_t, the correlation is not sharp (see Fig. 9). Can the reducibility analysis be biased by the assumption of a linear correlation between E_t and the true excitation energy?
- The measured transverse energy of an event is, by definition (see Eq. (18)), correlated with the number of IMFs in the event. Can the observed binomial features be produced by an auto-correlation between the number of IMFs and the measured transverse energy of the event? Alternatively, can a Poisson distribution be distorted into a binomial distribution, due to event fluctuations associated with the use of the transverse energy?
- Is the Arrhenius plot affected by incomplete detection coverage and reduced geometric efficiency? Are there effects associated with the bias of the particular experimental devices used to collect the data?

To investigate these issues we have implemented two elementary Monte Carlo simulations of multifragment decay, a binomial simulation and a Poisson simulation. The events, simulated within different physical scenarios (such as a small source of fragment emission, multiple sources etc.) and processed in the same fashion as the experimental data, served as a tool to clarify the questions listed above.

8.2 Binomial simulation

We now describe the Monte Carlo algorithm used to generate multifragment events, characterized by reducibility and thermal scaling both in the fragment multiplicity distributions and in the charge distributions, in qualitative agreement with the experimental data.

8.2.1 Event generator

A source of mass A_0, charge Z_0 and excitation energy E^* deexcites by emitting a fixed number (m_o) of particles. The decay chain is implemented through m_o steps (that need not be necessarily interpreted as time-like). The number of "throws" m_o is excitation energy dependent; for simplicity we have assumed:

$$m_o = const \cdot E^*. \tag{89}$$

The result of each step is either the emission of one neutron or the emission of an *inert* charged particle (Z = 1 - 20). Neutrons participate in all m_o steps, while particles of charge Z participate in only $m_Z = m_o/Z$ steps. This choice of $m_Z = m_o/Z$ originates from the experimental observation that the binomial parameter m exhibits a dependence on the lower Z threshold in the IMF definition ($Z_{\rm th}$). The experimental value of m decreases with increasing $Z_{\rm th}$, roughly scaling as $m \cdot Z_{\rm th}$ (see Sec. 4.8.4 and Ref. [90]).

The Monte Carlo algorithm is implemented in the following way. For the i^{th} step, the maximum participating Z is $Z_{max} = m_o/i$ and the emission probabilities are:

$$p_Z(i) = C_N(Z_{max}) \exp(\frac{-b \cdot Z}{T}), \quad Z = 1, Z_{max}(i), \quad i = 1, m_o. \tag{90}$$

The fragment emission barrier $B_Z = (b \cdot Z)$ in Eq. (90) contains a Z dependence suggested by the Coulomb interaction and is kept constant throughout the decay process. The probability for neutron emission is taken as:

$$p_0(i) = C_N(Z_{max}), \quad i = 1, m_o. \tag{91}$$

The normalization constant $C_N(Z_{max})$ is chosen so that:

$$\sum_{Z=0}^{Z_{max}} p_Z(i) = 1. \tag{92}$$

The nuclear temperature T is parametrized as in the Fermi gas model:

$$T = \sqrt{\frac{E^*}{a}}, \quad a = \frac{A_0}{8.5}. \tag{93}$$

A fragment of charge Z is assigned a mass number A determined from the parametrization $A = 2.08Z + 0.0029Z^2$ [91].

Charge and mass are conserved in the simulation. If the fragment extracted in the i^{th} step is larger than the residual source, the i^{th} emission is prohibited. This procedure effectively reduces the number of emissions with respect to the input parameter m_o.

Each fragment is assigned a finite radius appropriate to its size, according to the empirical parametrization: $r = 1.128A^{1/3}(1-0.786A^{-2/3})$ [92]. The fragments are then isotropically distributed in a sphere of dilute nuclear matter (half normal density) and given an initial momentum. Under the assumption of thermal equilibrium, the initial momenta are determined from an equal sharing of the available excitation energy among all emitted particles (including neutrons and light charged particles). The trajectories of the source and of all emitted fragments under their mutual Coulomb interaction are calculated classically.

Angular momentum effects are neglected.

Events, characterized by the total multiplicity (m_o), and single particle observables (mass and atomic number, kinetic energy, polar and azimuthal angles: A,Z,E, θ,ϕ) are produced following the above prescription. From the simulated events, excitation functions and Arrhenius plots are generated.

8.2.2 Analysis of the simulated events

Simulations for sources of ^{197}Au, ^{129}Xe and ^{64}Cu were performed and compared with experimental results from the ^{36}Ar + ^{197}Au [29] and ^{129}Xe-induced [30] reactions. The simulated events were analyzed following the procedures outlined in the first half of this paper. The analysis was performed using the conventional IMF definition $3 \leq Z_{\rm IMF} \leq 20$ (i.e. $Z_{\rm th} = 3$) except when specified otherwise. The binomial parameters p and m were extracted at each value of E^* from the binomial relationships:

$$\langle n \rangle = pm, \qquad \sigma^2 = pm(1-p) \tag{94}$$

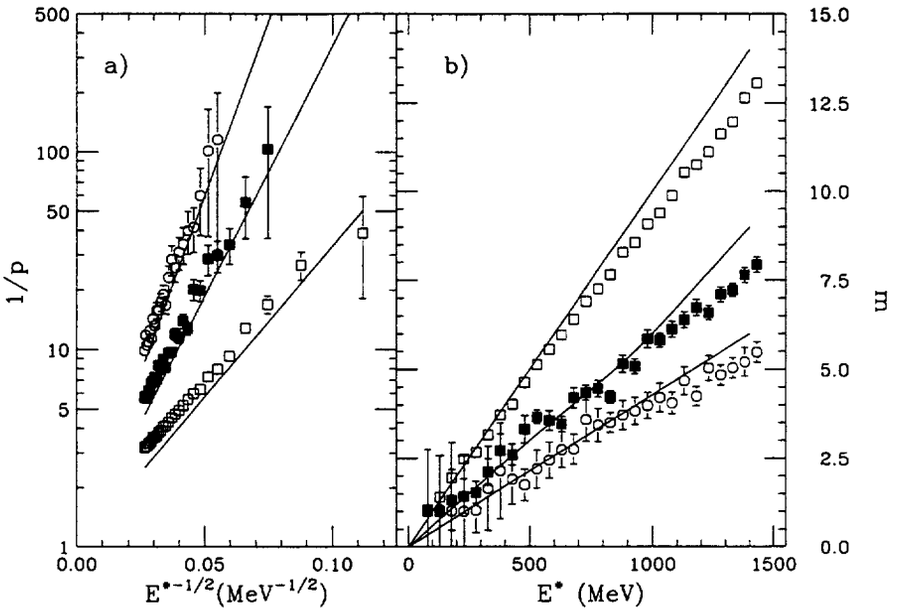

Fig. 36. Simulated binomial decay of a ^{129}Xe source. Results from the analysis of the mean and variance of the IMF excitation functions are shown by the symbols. Panel (a): E^*-Arrhenius plot. Open squares: $Z_{\rm th}$=3. Solid squares: $Z_{\rm th}$=5. Open circles: $Z_{\rm th}$=7. Solid lines: simulation input values of $1/p_Z$ from Eq. (90) for $Z = 3, 5, 7$. Panel (b): number of trials m. Open squares: $Z_{\rm th}$=3. Solid squares: $Z_{\rm th}$=5. Open circles: $Z_{\rm th}$=7. Solid lines: input values of $m_Z = m_{\rm o}/Z$ for $Z = 3, 5, 7$. The source residue was not included in the analysis.

which can be rewritten as:

$$p = 1 - \frac{\sigma^2}{\langle n \rangle}, \qquad m = \frac{\langle n \rangle^2}{\langle n \rangle - \sigma^2} \tag{95}$$

where $\langle n \rangle$ and σ^2 are the mean and the variance of the fragment multiplicities.

For all the simulations discussed here, the extracted values of p and m, when introduced in the binomial expression (Eq. (23)), provide an accurate fit of the n-fold IMF emission probabilities.

8.2.3 Arrhenius plots and barrier extraction

Both for the experiments and the simulations, one may wonder what is the meaning of the extracted elementary probability p, since many different barriers are expected to govern the decay (Eq. (90)). In Sec. 4.8.1 we argued that the average probability p should retain the form $\exp(-B/T)$ with B corresponding to the barrier of the lowest Z in the IMF definition.

We have tested the validity of this assumption by simulating the decay of ^{129}Xe with initial excitation energies in the range of 100 to 1500 MeV and input parameters $B_Z = (3 \cdot Z)$ MeV, $m_{\rm o}(E^*) = 0.03 \cdot E^*$.

The "observed" p and m were extracted from the mean and the variance of the simulated IMF emission probabilities as discussed above. The natural logarithm of $1/p$ was plotted as a function of $1/\sqrt{E^*}$. Since the resulting Arrhenius plot obeys:

$$1/p = e^{-B_{\rm obs}/T}, \tag{96}$$

the "observed" fragment emission barrier $B_{\rm obs} = b' \cdot Z_{\rm th}$ is readily extracted and compared to the simulation input value $B = b \cdot Z_{\rm th}$, thus allowing for an estimate of the systematic error associated with this procedure.

Arrhenius plots were constructed for progressively higher values of $Z_{\rm th}$ and the results are summarized in Fig. 36a. The Arrhenius plots become progressively steeper for $Z_{\rm th}$ increasing from 3 to 7. The resemblance between Fig. 36a and Fig. 19 is remarkable. The slopes of the simulated "data" are in good agreement (about 5%) with the input barriers shown by the solid lines.

Fig. 36b shows that for the number of trials m the "observed" values (symbols) also agree with the input values $m_o/Z_{\rm th}$ (lines).

The favorable comparison between the input parameters, b and $m_o/Z_{\rm th}$, and the corresponding extracted output parameters, b' and m, suggests that, if the excitation energy of the system is known, then one should be able to extract useful information regarding the barriers for fragment emission.

8.2.4 Arrhenius plots and source residues

In the ^{129}Xe source simulation, a source residue is always left at the end of the decay for $E^* \leq 1500$ MeV. In the excitation energy range $800 \leq E^* \leq 1500$ MeV, the residue's atomic number falls within the IMF definition ($3 \leq Z_{\rm IMF} \leq 20$). To produce excitation functions, we are thus presented with two possibilities: count the source residue among the IMFs, or ignore it. The results shown in Fig. 36 were obtained neglecting the source residue. However, since experimentally one is not always able to distinguish between true reaction products and residue-like fragments, we have repeated the analysis of the simulated events considering both alternatives. Fig. 37 compares the results obtained for the two cases. In panels (a),(b) and (c) the source residue is neglected. From the mean and the variance of the n-fold IMF excitation functions (panel (a)), the binomial parameters p and m are extracted and compared to the input values (panels (b) and (c) respectively, as in Fig. 36 for $Z_{\rm th}$=3). Panels (d),(e) and (f) present the same quantities, but now the source residue is counted as one IMF. It is clear that the input is reproduced only when the source residue is excluded from the analysis (panels (b) and (c)) . If the source residue is counted among the IMFs, the ratio of the variance to the mean of the n-fold excitation functions increases, causing the appearance of a pronounced "bump" in the Arrhenius plot (panel (e)) as well as in the extracted values of m (panel (f)). The reason is that the simple binomial counting scheme is spoiled because the last "IMF" (the residue)

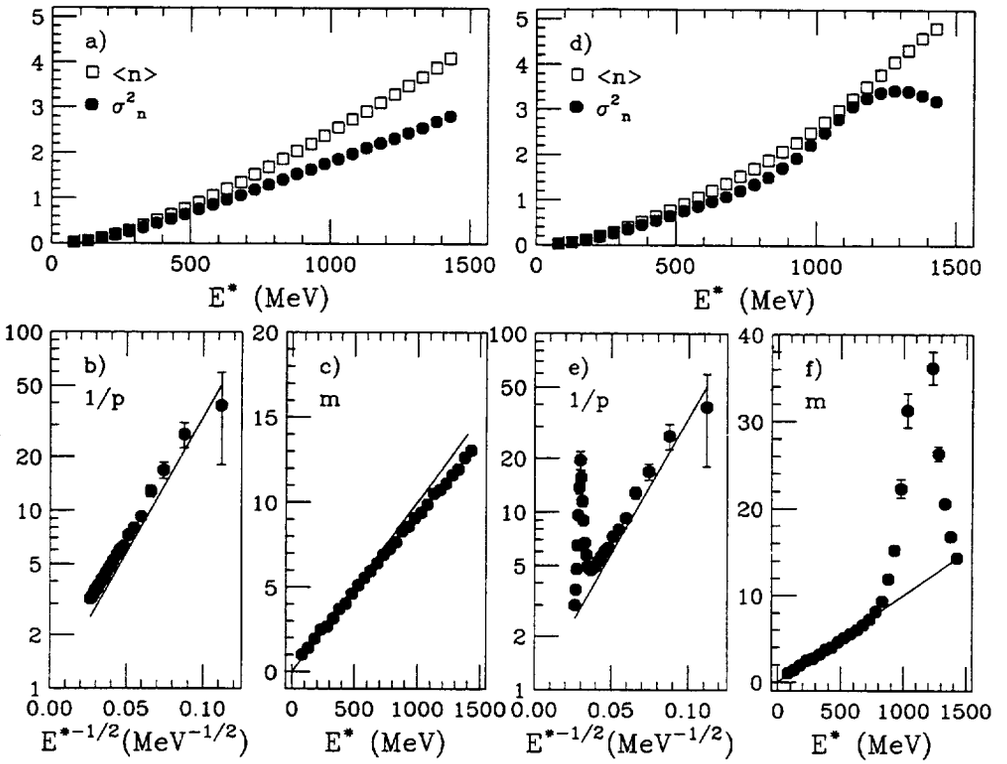

Fig. 37. Simulated binomial decay of a ^{129}Xe source with excitation energies and binomial parameters as in Fig. 36. Panels (a), (b), (c): The source residue is excluded from the analysis. Panel (a): Mean (squares) and variance (circles) of the fragment multiplicities. Panels (b), (c): E^*-Arrhenius plot and number of trials m (same as in Fig. 36 for $Z_{\rm th}$=3). Symbols: extracted values from mean and variance. Solid lines: simulation input values for emission of charge $Z = 3$ fragments. Panels (d), (e), (f): Same as panels (a), (b), (c), but now the source residue is included in the analysis (see text for details).

comes for "free". These results are rather dramatic, and may cast doubts on the possibility of performing a clean analysis of experimental data.

In the data presented in Sec. 4 however, no such effects due to residue contamination were observed for the following reasons: 1) The experimental energy thresholds were sufficiently large to stop the slow moving target-like residue in the direct kinematics reactions. 2) The projectile-like residue was kinematically focused beyond the geometric acceptance of the detection device for some of the reverse kinematics reactions. 3) The IMF definition is restricted to the range $3 \leq Z_{\rm IMF} \leq 20$, to minimize contamination from large target and projectile-like spectators.

8.2.5 Arrhenius plots and small size effects

Fig. 38 presents results from the analysis of a ^{64}Cu source simulation, with total excitation energies in the range 100 to 1500 MeV, and binomial input parameters $B_Z = (3 \cdot Z)$ MeV and $m_o(E^*) = 0.03 \cdot E^*$. A striking feature of this simulation (obtained without counting the source residue as one IMF) is the loss of linearity of

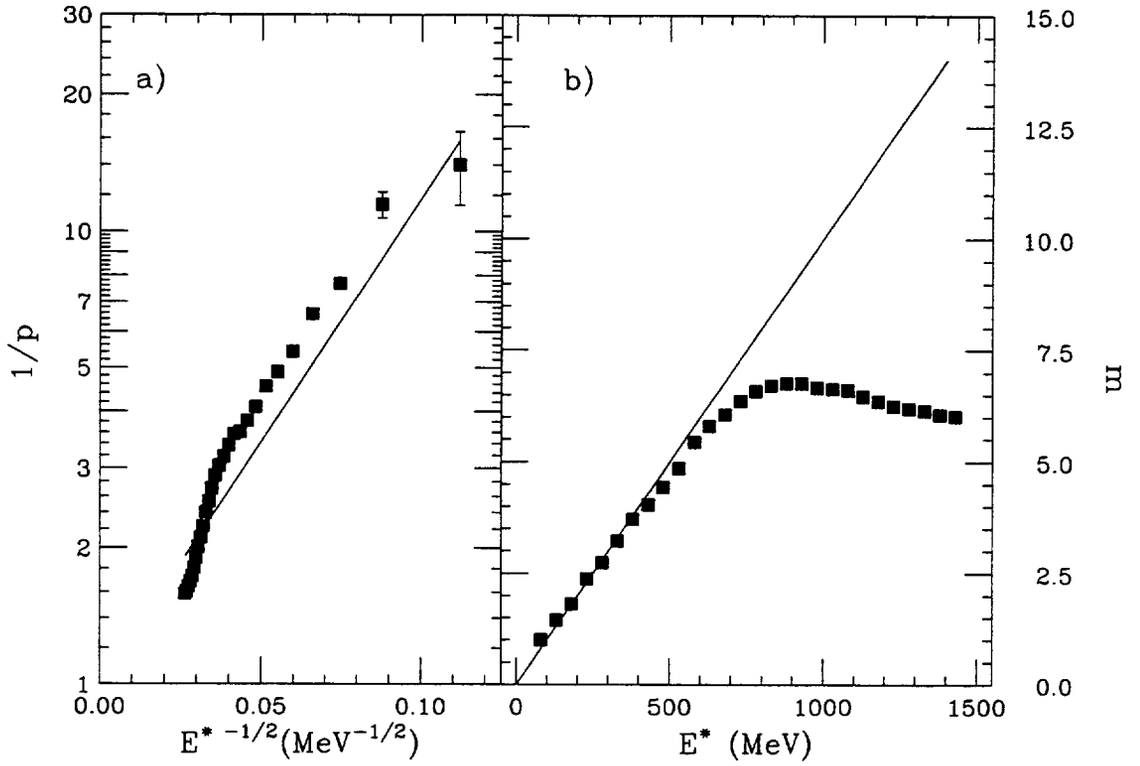

Fig. 38. Simulated binomial decay of a ^{64}Cu source with excitation energies and binomial parameters as in Fig. 36. Panels (a), (b): E^*-Arrhenius plot and number of trials m. Symbols: extracted values from the mean and the variance. Solid lines: simulation input values for emission of charge $Z = 3$ fragments. The source residue was excluded from the analysis.

the Arrhenius plot (panel (a)) in the high excitation energy region ($E^* > 600$ MeV). This anomalous behavior is due to the charge conservation constraint which comes into play when the source of fragment emission is small. Also, the extracted values of m deviate from the linear input, and at high E^* a saturation is observed (panel (b)) again reflecting the constraint of charge (and mass) conservation implemented in the simulation. For a ^{64}Cu source at excitation energies larger than about 600 MeV, it sometimes happens that the fragment extracted in the i^{th} step is larger than the residual source. In this case the i^{th} emission is inhibited, leading to an effectively reduced number of emissions with respect to the input parameter m_o.

8.2.6 Arrhenius plots and multiple sources

The invariant velocity plots for IMF emission in ^{129}Xe-induced reactions [35] reveal that, for peripheral collisions (i.e. at low values of E_t), there appear to be more than one source (for example, target-like, projectile-like and mid-rapidity or neck [93]).

Unexpectedly, the analysis shows that binomial reducibility and thermal scaling continue to hold even at low E_t values. It is therefore interesting to study whether the Arrhenius plot is sensitive to the number of decaying sources.

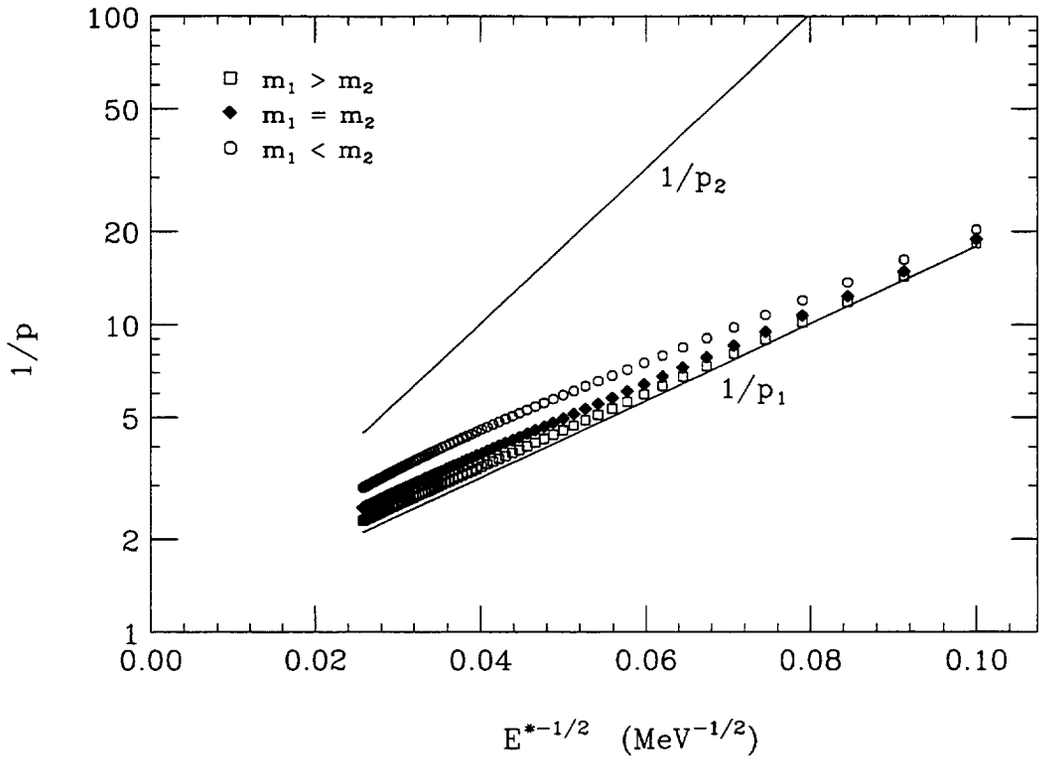

Fig. 39. Arrhenius plots from the simulated binomial decay of two sources. Solid lines: input values of $1/p_1$, $1/p_2$ ($B_1 = (3{\cdot}Z)$ MeV, $B_2 = (4{\cdot}Z)$ MeV, $Z = 3$). Symbols: diamonds: $1/p_{\rm obs}$ from input $1/p_1$, $1/p_2$, $m_1 = m_2 = 20$. Squares: $1/p_{\rm obs}$ from input $1/p_1$, $1/p_2$, $m_1 = 40$, $m_2 = 20$. Circles: $1/p_{\rm obs}$ from input $1/p_1$, $1/p_2$, $m_1 = 20$, $m_2 = 40$.

A linear Arrhenius plot does not exclude the presence of multiple sources. For instance, the decay of two binomial sources *with the same elementary probability* p is equivalent to the decay of one source with the same probability and with number of trials m equal to the sum of the number of trials m_1 and m_2 of the two sources. This is the only case for which the sum of two binomial distributions gives an exact binomial distribution. However, the excitation functions obtained from two sources with different elementary probabilities can be approximated by a binomial distribution dominated by the source with the larger emission probability.

The distributions produced by two sources with binomial parameters (p_1, m_1) and (p_2, m_2) appear as one single distribution with mean and variance:

$$\langle n \rangle_{\rm obs} = p_1 m_1 + p_2 m_2 = p_{\rm obs} m_{\rm obs} \tag{97}$$

$$\sigma^2_{\rm obs} = p_1 m_1 (1 - p_1) + p_2 m_2 (1 - p_2) = p_{\rm obs} m_{\rm obs} (1 - p_{\rm obs}) \tag{98}$$

and can therefore be interpreted as originating from one source with binomial parameters (Eq. (95)):

$$p_{\rm obs} = \frac{m_1 p_1^2 + m_2 p_2^2}{m_1 p_1 + m_2 p_2}, \qquad m_{\rm obs} = \frac{(m_1 p_1 + m_2 p_2)^2}{m_1 p_1^2 + m_2 p_2^2}. \tag{99}$$

In such a situation the Arrhenius plot is a nearly straight line and the barrier extracted from its slope is a good approximation to the true barrier of the dominant source, i.e. of the source with lower barrier (higher p) and/or higher m. The first relationship of Eqs. (99) is plotted in Fig. 39 for combinations of two sources with different binomial input parameters. When one source dominates, reducing the excitation functions to the binomial distribution, and extracting p and m, is still a suitable procedure to characterize the dominant source.

8.2.7 Charge distributions

We have seen in Sec. 5 that the n-fold charge distributions $P_n(Z)$ are reducible to the corresponding 1-fold distribution through the scaling law (Eq. (42)):

$$P_n(Z) = \exp\left(-B_Z/T - ncZ\right) \tag{100}$$

where B_Z is the barrier for the emission of a fragment with charge Z, T is the temperature (assumed proportional to $\sqrt{E_t}$) and c is an empirical quantity characterizing the dependence of the charge distributions on the number of intermediate mass fragments n. The reducibility of the n-fold charge distributions to the 1-fold distribution through Eq. (100), demonstrates the near independence of individual fragment emission, with a limiting constraint manifested through the factor $\exp(-ncZ)$.

Experimentally the quantity c starts from near zero at low E_t values and reaches a saturation value at high E_t as shown in Fig. 30 [62]. As discussed before, the $c = 0$ regime could mean that a source evaporates down to a sizeable remnant, while for $c > 0$ the source vaporizes completely.

Binomial decay simulations, for the decay of ^{129}Xe and ^{64}Cu sources were performed with excitation energies in the range 100-3000 MeV. The input parameters for these simulations were: $B = (3 \cdot Z)$ MeV and $m_o(E^*) = 0.05 \cdot E^*$. The resulting charge distributions follow Eq. (100) so precisely that they can be analyzed just like the experimental data for the extraction of the parameter c.

The dependence of c on E^* already shown in Fig. 32 is shown again in Fig. 40, together with that of the binomial parameter m. The quantity c starts from zero at low E^* and reaches a saturation value at high E^*. The $c = 0$ region in the simulation, corresponds to emission from a source that survives as a charge conserving residue. Since each fragment does not know how many other fragments will follow it, the resulting charge distribution can not reflect charge conservation under the constraint of n fragments. In such a scenario, charge conservation affects the distribution minimally. A large residue serves as a reservoir of mass, charge and excitation energy, weakening the charge correlations between fragments and thereby reducing c.

The transition region, where c increases with excitation energy, corresponds to a source residue whose dimensions are within the IMF definition. In the simulation

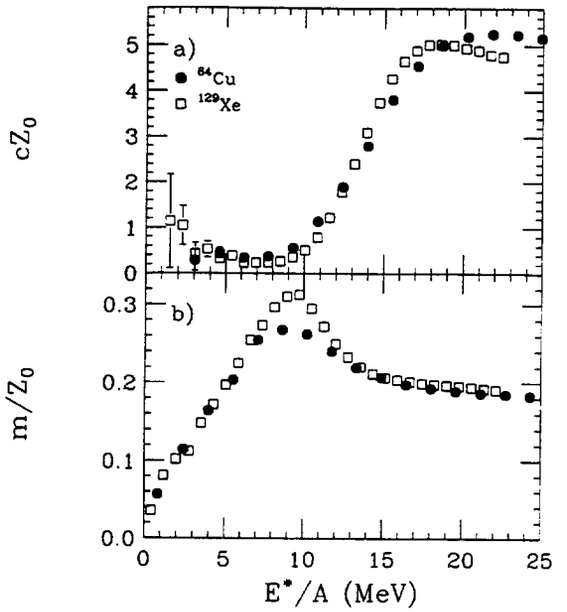

Fig. 40. Simulated binomial decay of ^{129}Xe (Z_0=54) (squares) and ^{64}Cu (Z_0=29) (circles) sources. Plotted as a function of the excitation energy per nucleon: Panel (a): Values of cZ_0. Panel (b): Number of binomial trials (extracted from the mean and the variance of the excitation functions), divided by the total charge of the source, m/Z_0.

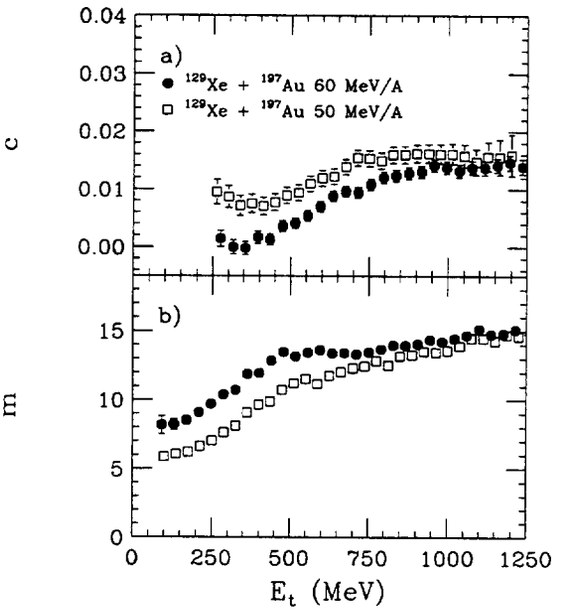

Fig. 41. Experimental data from ^{129}Xe + ^{197}Au reactions at E/A = 50 (squares) and 60 (circles) MeV [30]. Panel (a): Values of c versus E_t [62]. Panel (b): Values of m versus E_t [30].

this is the moment when the small source size effects set in, since heavy IMF decay channels are effectively inhibited in order to conserve charge and mass. The deviation of c from zero, and the deviation of the extracted binomial m from the input m_o/Z, occur together at the same excitation energy, as shown in Fig. 40. A similar correlation

between c and m has also been observed in some experimental data. An example is shown in Fig. 41.

Finally, the $c > 0$ saturated region at high E^* corresponds to complete vaporization of the source.

Of relevance is the scaling of both c and m observed in the simulation. A complete scaling can be achieved for the two different sized sources if one plots the quantities cZ_o and m/Z_o versus E/A. This is in agreement with the considerations made previously in Secs. 4.8.4 and 6.4.

8.3 Poisson distributions, E^*-E_t correlation and E_t auto-correlation

Ideally one would like to verify reducibility at fixed values of the excitation energy E^*. Experimentally, however, this can only be done as a function of E_t, under the assumption that events selected at a given E_t arise mainly from one value of E^*.

Recently Del Zoppo *et al.* have claimed that the use of global observables, which exhibit event-to-event fluctuations, might introduce auto-correlations between pairs of observables that may "simulate specific signatures of a particular physical regime" [94]. Since the measured transverse energy is such a global observable, correlated with the number of detected IMFs of an event, it has been suggested [94,95] that the feature of binomial reducibility might arise from the correlation between the measured transverse energy and the number of detected fragments ($N_{\rm IMF}$).

In Ref. [94] it is empirically observed that the multiplicities $N_{\rm LCP}$ of light charged particles (LCP, $Z \leq 2$), emitted from the reaction ^{132}Xe + ^{158}Gd at a bombarding energy of $E/A = 44$ MeV, are binomially distributed at any given transverse energy. These distributions are assumed to be originally Poissonian, and the observed binomial nature is shown to arise from the auto-correlation between the measured transverse energy and the light charged particle multiplicity. As a point of fact, in the analysis of Ref. [94] the very particles whose multiplicities are studied contribute *exclusively* to the measurement of the transverse energy, and the measured value of the transverse energy is therefore strongly dependent upon the number of detected particles. This auto-correlation leads to narrow distributions of $N_{\rm LCP}$ over the entire range of measured transverse energy. Consequently the variance becomes smaller than the mean $\langle N_{\rm LCP} \rangle$ and this deviation from the Poisson distribution grows with increasing auto-correlation. Eventually the binomial approach becomes appropriate for describing the $N_{\rm LCP}$ distributions.

In this section, we investigate the event fluctuations associated with the use of the transverse energy. In particular we try to study the conditions under which these fluctuations are sufficiently large to distort a Poisson distribution into a binomial distribution. To this end, we have performed simple Poisson simulations for intermediate

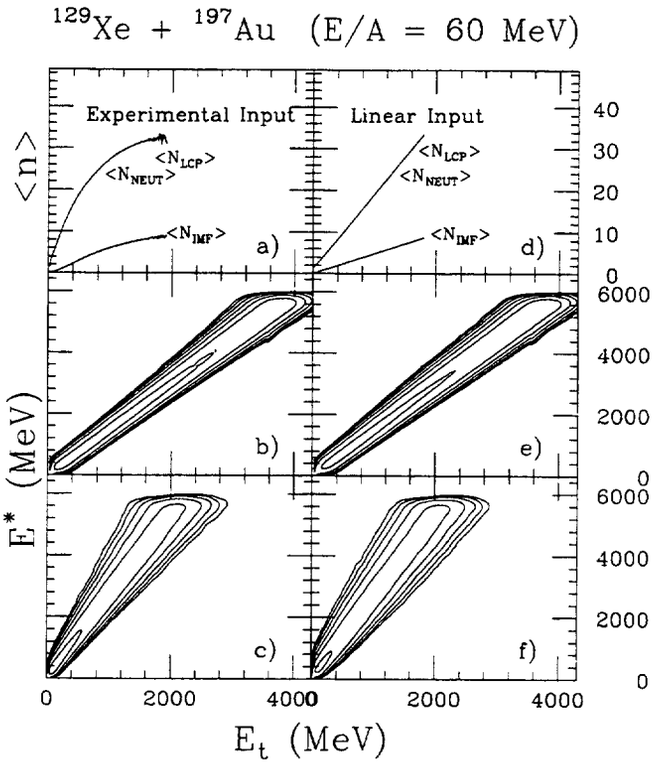

Fig. 42. Panel (a): Experimental input values of $\langle N_{\mathrm{NEUT}}\rangle$, $\langle N_{\mathrm{LCP}}\rangle$, $\langle N_{\mathrm{IMF}}\rangle$ as a function of E_t taken from the data of the reaction ^{129}Xe + ^{197}Au at $E/A = 60$ MeV. Panel (b): Logarithmic contour plot of the correlation between E^* and E_t (calculated including neutrons) observed for the Poisson particle emission simulation. Panel (c): The correlation between E^* and E_t^m (calculated excluding neutrons). Panel (d): The linear input values of $\langle N_{\mathrm{NEUT}}\rangle$, $\langle N_{\mathrm{LCP}}\rangle$, $\langle N_{\mathrm{IMF}}\rangle$ as a function of E_t. Panel (e): The correlation between E^* and E_t . Panel (f): The correlation between E^* and E_t^m .

mass fragment (IMF), light charged particle (LCP) and neutron (NEUT) multiplicities as a function of excitation energy. We have then studied the resulting multiplicity distributions as a function of the transverse energy to assess possible biases to our results from using E_t as a measure of the excitation energy.

8.3.1 Poisson simulation

Poisson distributions of IMF, LCP and NEUT multiplicities were generated as a function of E^* from input values of $\langle N_{\mathrm{IMF}}\rangle(E^*)$, $\langle N_{\mathrm{LCP}}\rangle(E^*)$ and $\langle N_{\mathrm{NEUT}}\rangle(E^*)$, respectively. The inputs for $\langle N_{\mathrm{IMF}}\rangle$ and $\langle N_{\mathrm{LCP}}\rangle$ were taken from the experimental data for ^{129}Xe +^{197} Au at E/A = 60 MeV, and are shown in Fig. 42a. As suggested by thermal models, we assumed $E^* = 3E_t^{\mathrm{exp}}$ where E_t^{exp} is the experimentally measured transverse energy. The proportionality constant is 3 rather than 3/2 in order to account for not detecting neutrons. For simplicity, the input for $\langle N_{\mathrm{NEUT}}\rangle$ was taken equal to $\langle N_{\mathrm{LCP}}\rangle$ with the same excitation energy dependence. The resulting distributions in $\langle N_{\mathrm{IMF}}\rangle$, $\langle N_{\mathrm{LCP}}\rangle$ and $\langle N_{\mathrm{NEUT}}\rangle$ were completely independent, since no charge

or mass conservation was applied. In fact, no charge or mass information was used, and the distributions were identical except that they were generated from different mean values and labelled as IMF, LCP and NEUT respectively. The polar (θ) and the azimuthal (ϕ) angles of these emitted particles were distributed isotropically. The excitation energy was assumed to be thermal, and the kinetic energy of each particle was set equal to $E = E^*/N$ with $N = N_{\rm IMF} + N_{\rm LCP} + N_{\rm NEUT}$. For simplicity, no Coulomb trajectory calculation was implemented, and the transverse energy of each particle was calculated according to its definition, $E_t^i = E_i \sin^2\theta_i$.

8.3.2 E^*-E_t correlation

The average transverse energy for events of a fixed excitation energy can be calculated:

$$\langle E_t \rangle = \left\langle \sum_i^N \frac{E^*}{N} \sin^2\theta_i \right\rangle = E^* \frac{\int \sin^2\theta_i d\cos\theta_i}{\int d\cos\theta_i} = \frac{2}{3}E^*. \tag{101}$$

The above equation clearly shows that the average transverse energy of a class of events depends solely on the excitation energy and is independent of the number of particles emitted. This implies that there is no correlation between the particle multiplicity n and the transverse energy of an event other than their individual dependence on the excitation energy. In this context, n can be $N_{\rm IMF}$, $N_{\rm LCP}$ or $N_{\rm NEUT}$ for fragment, light charged particle and neutron multiplicity respectively.

The simulated correlation between E_t and E^* is plotted in panel (b) of Fig. 42. A linear correlation is observed and the value of $\langle E_t \rangle$ is $2/3E^*$, consistent with the prediction of Eq. (101). This shows that the events with a given E_t come from a rather narrow distribution of E^* with centroid $= 3/2E_t$. Therefore, the resulting multiplicity distribution at a given transverse energy $P_{E_t}(n)$ is an average of multiplicity distributions $P_{E^*}(n)$ weighted by the excitation energy distribution at that transverse energy, $P_{E_t}(E^*)$:

$$P_{E_t}(n) = \int P_{E_t}(E^*) \cdot P_{E^*}(n) dE^*. \tag{102}$$

The question naturally arises whether this folding procedure introduces large event fluctuations. In particular, under what circumstances will the mean and variance information of $P_{E^*}(n)$ be preserved in the resulting multiplicity distribution $P_{E_t}(n)$? A trivial case is considered by assuming the multiplicity distribution $P_{E^*}(n)$ to be energy independent. The resulting multiplicity distribution from the above folding procedure (Eq. (102)) simply preserves the mean and variance information as shown below:

$$P_{E_t}(n) = \int P_{E_t}(E^*) \cdot P_{E^*}(n) dE^* = P(n) \int P_{E_t}(E^*) dE^* = P(n). \tag{103}$$

For more realistic situations, as in statistical decay, the particle emission probability increases with nuclear temperature, and thus introduces an energy dependence into

the multiplicity distribution $P_{E^*}(n)$. In these cases, the fluctuations due to the spread in the excitation energy associated with events of a given transverse energy can no longer be neglected. In fact, the resulting variance ($\sigma^2_{E_t}$) of $P_{E_t}(n)$ strongly depends on the variance $\sigma^2_{E^*E_t}$ of the excitation energy distribution $P_{E_t}(E^*)$.

When the correlation between E_t and E^* is strong, the distribution $P_{E_t}(E^*)$ becomes a δ function and its corresponding variance $\sigma^2_{E^*E_t}$ approaches zero:

$$P_{E_t}(E^*) = \delta(E^* - \frac{3}{2}E_t). \tag{104}$$

In this limit, the resulting multiplicity distribution preserves the mean and variance information, namely:

$$\begin{aligned} P_{E_t}(n) &= P_{E^*=\frac{3}{2}E_t}(n) \\ \langle n \rangle_{E_t} &= \langle n \rangle_{E^*=\frac{3}{2}E_t} \\ \sigma^2_{E_t} &= \sigma^2_{E^*=\frac{3}{2}E_t}. \end{aligned} \tag{105}$$

However, when the correlation between E_t and E^* is weakened, the excitation energy distribution at a given value of E_t becomes broader (i.e. $\sigma^2_{E^*E_t} > 0$). The multiplicity distribution $P_{E_t}(n)$ is now an average over events with a range of E^*, and this introduces event fluctuations. When the excitation energy distribution is symmetric with respect to $E^* = \frac{3}{2}E_t$, the information for the average multiplicity $\langle n \rangle$ is still preserved according to Eq. (105), but the corresponding variance is broadened by this folding procedure, namely:

$$\sigma^2_{E_t} > \sigma^2_{E^*=\frac{3}{2}E_t}. \tag{106}$$

As a result, the ratio $\sigma^2_{E_t}/\langle n \rangle_{E_t}$ becomes larger than the Poisson value of 1. This distortion of a Poisson distribution due to event fluctuations arising from the use of E_t *does not* lead to a binomial distribution, which is characterized by a ratio $\sigma^2_{E_t}/\langle n \rangle_{E_t}$ smaller than unity.

8.3.3 E_t auto-correlation

To verify whether a Poisson distribution is distorted, we rely on several quantities that bear unique properties in the Poisson limit. First of all, the ratio $\sigma^2_{E_t}/\langle n \rangle_{E_t}$ and its deviation from the Poisson value of 1 is examined. Then we study the quantity $g(n)$ defined as follows [96]:

$$g(n) = \frac{(n+1)P(n+1)}{P(n)}, \tag{107}$$

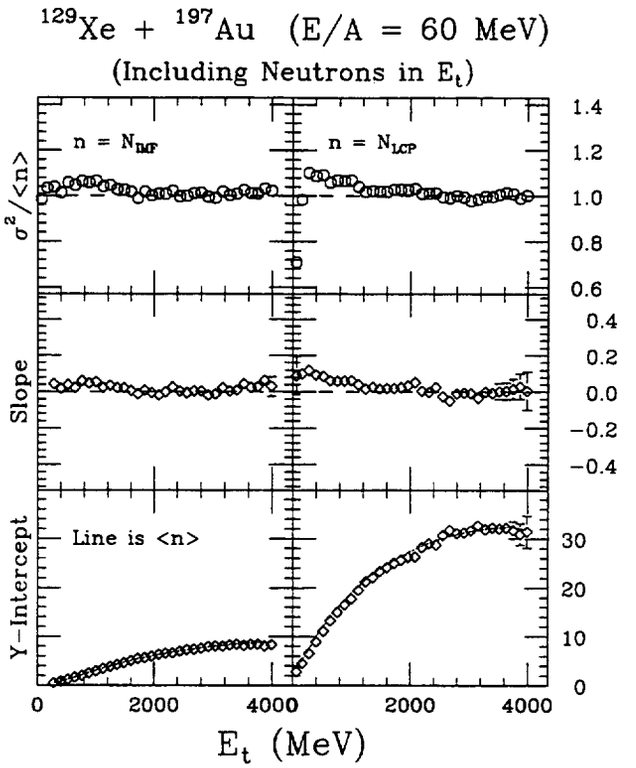

Fig. 43. For the N_{IMF} (left column) and N_{LCP} (right column) distributions generated from the Poisson simulation using the experimental input (Fig. 42a): the ratio $\sigma^2/\langle n\rangle$ of the IMF distributions(top panel), the slope (middle panel) and the y-intercept (bottom panel) of $g(n)$ versus n are shown as a function of E_t. The solid lines in the bottom panels indicate the input values of $\langle N_{\mathrm{IMF}}\rangle$ and $\langle N_{\mathrm{LCP}}\rangle$ as a function of E_t.

where $P(n)$ is the probability to observe an event of particle multiplicity n. In the Poisson limit:

$$g(n)_{Poisson} = \frac{(n+1)\frac{<n>^{n+1}e^{-<n>}}{(n+1)!}}{\frac{<n>^{n}e^{-<n>}}{n!}} = \langle n\rangle\,, \tag{108}$$

$g(n)$ is independent of n, and therefore, the slope of $g(n)$ versus n is 0, and the corresponding y-intercept is equal to the average particle multiplicity $\langle n\rangle$.

We proceed to study specifically the effect of event-to-event fluctuations on the N_{IMF} and N_{LCP} distributions. In Fig. 43, we plot the ratio $\sigma^2/\langle n\rangle$ along with the slope and y-intercept of $g(n)$ versus n as a function of transverse energy for both the N_{IMF} (left column) and N_{LCP} (right column) distributions obtained from the above Poisson simulations. In both cases, the ratios $\sigma^2/\langle n\rangle$ scatter around the value of 1. The plots of $g(n)$ versus n are flat and their y-intercepts agree reasonably well with the solid lines corresponding to the input average particle multiplicities $\langle n\rangle$. These observations indicate that the Poisson nature of the N_{IMF} and N_{LCP} distributions is preserved when one uses E_t as a measure of E^*. This is indeed consistent with the above discussion that E_t is not auto-correlated with N_{IMF} or N_{LCP}. However, if we

look at Fig. 43 more carefully, a small systematic discrepancy is observed between the slopes (symbols) of $g(n)$ versus n and the dashed lines at low E_t. The fact that the ratios $\sigma^2/\langle n\rangle$ are slightly larger than 1 in the same region suggests that this small deviation from the Poisson limit is not caused by auto-correlation, but rather by the random event fluctuations as a result of the folding procedure described by Eq. (102).

The results of these Poisson simulations show that there is no auto-correlation between E_t and $N_{\rm IMF}$ or $N_{\rm LCP}$ under the assumption that the excitation energy is thermal and evenly distributed among the emitted particles. The event fluctuations associated with E_t will at most increase the ratio $\sigma^2/\langle n\rangle$ of the resulting multiplicity distribution $P_{E_t}(n)$. Hence, this distortion of a Poisson distribution does not lead to a binomial distribution.

8.3.4 E_t auto-correlation and detection efficiency

Thus far, we have assumed 100% efficiency to measure E_t. In actual experiments the detection system is not perfect, and the measured transverse energy E_t^m may be different from the true E_t. For instance, neutrons have not been detected in the experiments described in Sec. 4 even though they carry kinetic energy and contribute significantly to the transverse energy of a given event. In this case, the transverse energy of a given event is underestimated ($E_t^m < E_t$).

In an attempt to study the effect of the missing neutrons in the measurement of the transverse energy, we have repeated the above analysis with E_t^m calculated from charged particles only. The simulated correlation between E_t^m and E^* is plotted in panel (c) of Fig. 42, and can be compared with the correlation between E_t and E^* plotted in panel (b) of Fig. 42. A linear correlation between $\langle E_t^m\rangle$ and E^* still exists, but the distribution at a given E_t^m becomes broader.

In Fig. 44, we plot the ratio $\sigma^2/\langle n\rangle$ along with the slope and y-intercept of $g(n)$ versus n as a function of E_t^m for both the $N_{\rm IMF}$ (left column) and $N_{\rm LCP}$ (right column) distributions obtained from the above Poisson simulations. For the $N_{\rm LCP}$ distribution, the ratio $\sigma^2/\langle N_{\rm LCP}\rangle$ scatters around 0.8. The slope of $g(N_{\rm LCP})$ versus $N_{\rm LCP}$ is negative, and the y-intercept is larger than the mean multiplicity $\langle N_{\rm IMF}\rangle$ at all values of E_t^m. In other words, the Poisson nature of $N_{\rm LCP}$ is not preserved at all values of E_t^m.

Since the value of the total charged particle multiplicity ($N_{\rm C}$) and thus of E_t^m arises mainly from LCP, a strong auto-correlation between $N_{\rm LCP}$ and E_t^m is not unexpected in this simulation. In this case, events with a given E_t^m arise from a narrow distribution of $N_{\rm LCP}$, and the distribution $P_{E_t}(n)$ does not follow the folding procedure of Eq. (102). Consequently, the variance becomes less than the mean, and the extraction of the binomial parameters p and m becomes feasible. These extracted quantities p and m are plotted as a function of E_t^m in Fig. 45. The probabilities of emitting n light charged particles, for $N_{\rm LCP}$ ranging from 3 to 30, are also plotted as a function of E_t^m using different symbols, together with the solid lines generated from the bi-

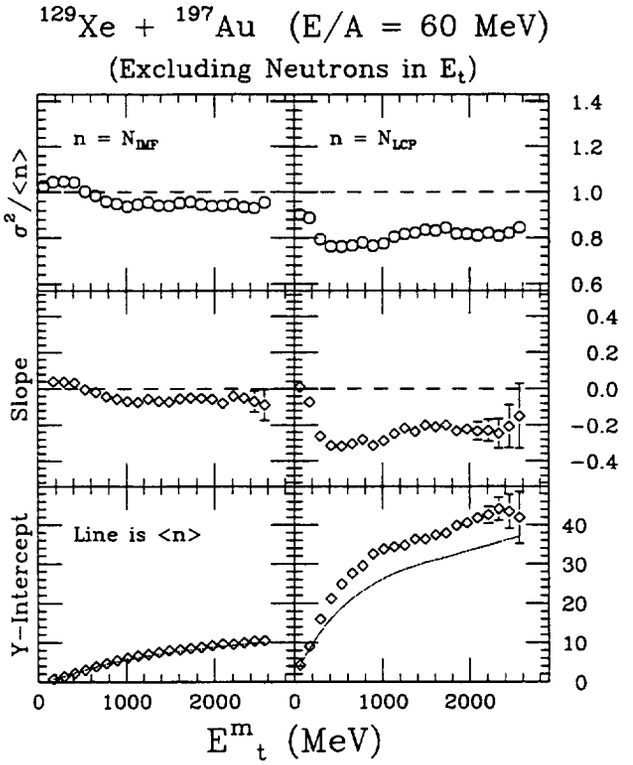

Fig. 44. For the N_{IMF} (left column) and N_{LCP} (right column) distributions generated from the Poisson simulation using the experimental input (Fig. 42a): the ratio $\sigma^2/\langle n \rangle$ of the IMF distributions (top panel), the slope (middle panel) and the y-intercept (bottom panel) of $g(n)$ versus n are shown as a function of E_t^m. The solid lines in the bottom panels indicate the values of $\langle N_{\mathrm{IMF}} \rangle$ and $\langle N_{\mathrm{LCP}} \rangle$ as a function of E_t^m.

nomial equation (Eq. (23)) using the above extracted values of p and m. Excellent agreement between the data (symbols) and the calculations (curves) for the entire range of E_t^m confirms the binomial nature of the distorted distributions. Remarkably, the elementary probability p is nearly constant with E_t^m. This confirms the findings of Ref. [94].

On the other hand, IMFs contribute little to N_{C} and thus to E_t^m, so the auto-correlation between E_t^m and N_{IMF} should be relatively weak as shown also in Fig. 44 left column. The y-intercept of the $g(N_{\mathrm{IMF}})$ versus N_{IMF} plot collapses onto the line corresponding to the mean fragment multiplicity $\langle N_{\mathrm{IMF}} \rangle$ at all values of E_t^m. A small negative slope is observed, and the ratio $\sigma^2/\langle N_{\mathrm{IMF}} \rangle$ is slightly less than unity except at the region of low E_t^m, where the slope and the ratio $\sigma^2/\langle N_{\mathrm{IMF}} \rangle$ are just larger than zero and unity respectively. This suggests that in the region of low E_t^m, the auto-correlation between N_{IMF} and E_t^m is negligible, and the residual event fluctuations slightly increase the variance of the N_{IMF} distributions. At higher E_t^m, the auto-correlation becomes observable, but the distortion from the Poisson distribution is still weak since the average IMF contribution to E_t^m is only 20%.

These results have been obtained from the Poisson distributions generated from a

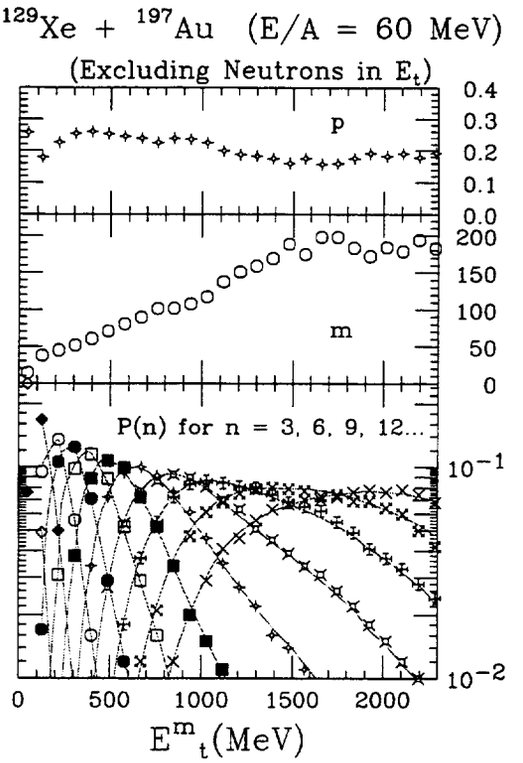

Fig. 45. For the $N_{\rm LCP}$ distribution generated from the Poisson simulation: the values of p (top panel) and m (middle panel) are extracted from the mean and variance as a function of E_t^m . Bottom panel: The probability to emit n light charged particles as a function of E_t^m. The curves are binomial calculations.

specific set of inputs. These inputs (Fig. 42a) appear to be parabolic functions of E^*. In order to study the sensitivity of the multiplicity distributions to different inputs, and for the sake of comparison, Poisson simulations were performed with a new set of inputs that are linear functions of E^*. More specifically, the end points of the experimental inputs of Fig. 42a were joined with straight lines to the origin to produce linear inputs (shown in Fig. 42d). The simulated correlations between the transverse energies ($E_t \& E_t^m$) and the excitation energy (E^*) obtained with the linear inputs are shown in panels (e) and (f) of Fig. 42. In both cases, the correlations are linear, consistent with the prediction of Eq. (101). We have also studied the effects of the fluctuations associated with $E_t \& E_t^m$ on the resulting $N_{\rm LCP}$ distribution, and the results shown in Fig. 46 are similar to those obtained for the experimental inputs. The event fluctuations associated with E_t clearly broaden the $N_{\rm LCP}$ distribution and thus increase the ratio $\sigma^2/\langle N_{\rm LCP}\rangle$. On the other hand, the strong auto-correlation between E_t^m and $N_{\rm LCP}$ distorts the Poisson distribution in the opposite direction by decreasing the ratio $\sigma^2/\langle N_{\rm LCP}\rangle$. Consequently, the relative magnitude of $\sigma^2/\langle N_{\rm LCP}\rangle$ can be used to distinguish the effect of random event fluctuations from that of auto-correlation.

The above study suggests that the transverse energy serves as a good observable for the measurement of the excitation energy. It has a sharp correlation with the excitation energy and has no auto-correlation with the fragment and light charged

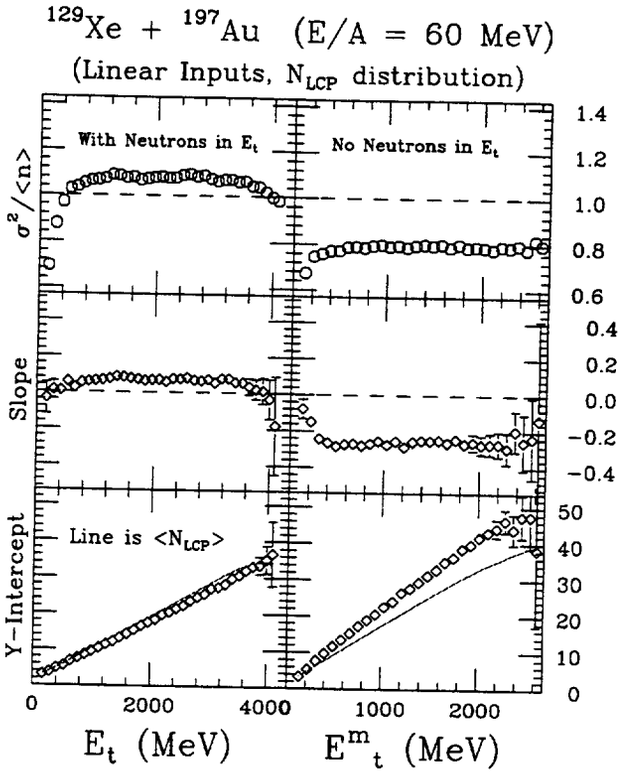

Fig. 46. For the $N_{\rm LCP}$ distribution generated from the Poisson simulation using the linear input: the ratio $\sigma^2/\langle n\rangle$ of the IMF distribution (top panel), the slope (middle panel) and the y-intercept (bottom panel) of $g(n)$ versus n are shown as a function of E_t (left column) and E_t^m (right column). The solid lines in the bottom panels indicate the values of $\langle N_{\rm IMF}\rangle$ as a function of E_t and E_t^m.

particle multiplicities being studied. On the other hand, if the measurement of the transverse energy is not perfect (possibly due to finite detection efficiency), an auto-correlation between $N_{\rm LCP}$ and the measured transverse energy E_t^m may be introduced. The experimental setup of Del Zoppo *et al.* [94] does not measure neutrons, and the geometric acceptance for charged particles is rather limited due to the lack of forward angular coverage. As a result, the auto-correlation effect in their analysis is likely to be strong and this might be the reason for their observation of binomial distributions characterized by flat Arrhenius plots for the light charged particles. On the other hand, IMF yields contribute 20% on average to the measured transverse energy E_t^m in multifragmentation studies at intermediate energies. Therefore, the auto-correlation between $N_{\rm IMF}$ and E_t^m is not sufficient to distort a Poisson distribution into a binomial distribution.

8.3.5 E_t-Arrhenius plots from binomial distributions

The correlation between E^* and E_t was simulated also with the binomial event generator, for a ^{197}Au source with excitation energies in the range 100 to 1500 MeV and binomial input parameters: $B_Z = (3 \cdot Z)$ MeV, $m_o(E^*) = 0.03 \cdot E^*$. The number of

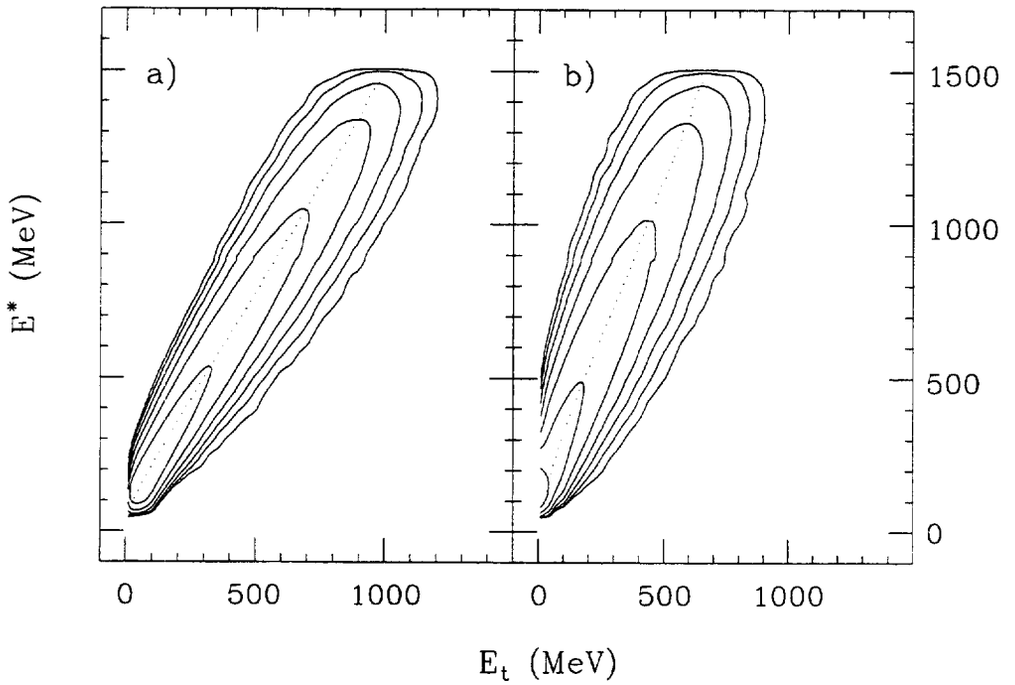

Fig. 47. Logarithmic contour plots of E^* versus E_t correlation from the binomial decay of a ^{197}Au source with excitation energies in the range 100 to 1500 MeV and binomial parameters $m_o(E^*) = 0.03 \cdot E^*$, $B_Z = (3 \cdot Z)$ MeV. Panel (a): E_t calculated from all particles including neutrons. Panel (b): E_t calculated from charged particles only. Dotted lines: mean value of E^* as a function of E_t.

events simulated at each excitation energy step was established according to a monotonic relationship between the excitation energy and the collision impact parameter [97]. The transverse energy E_t was calculated for each event from all emitted particles.

Panel (a) of Fig. 47 is a logarithmic contour plot of the correlation between E^* and E_t. The correlation is rather narrow and the mean value of E_t at each E^* is a nearly straight line passing nearly through zero, with proportionality constant approaching the expected value of $E_t = 2/3E^*$ (see Eq. (101)). Since the experimental data (Sec. 4) suffer a loss in sensitivity to the excitation energy deposition due to the lack of neutron detection capability, E_t was calculated also from the charged particles only, excluding the neutrons (E_t^m). Panel (b) of Fig. 47 shows that the linearity is preserved, although the proportionality constant between E^* and E_t^m is changed.

In panel (a) of Fig. 48, the value of $1/p$ is plotted as a function of $1/\sqrt{E_t}$. Due to the linear correlation between E^* and E_t, the effect of using E_t instead of E^* to construct the Arrhenius plot is simply a "stretching" of the x-axis. If the x-axis of the Arrhenius plot is rescaled with the linear relationship $E_t = 2/3E^*$ (solid squares in Fig. 48b), one observes nearly the same slope as the input to the calculation, with differences of about 10%. A similar result is obtained when E_t is calculated from only charged particles (circles in Fig. 48b) rescaling the x-axis with the relationship between E^* and E_t.

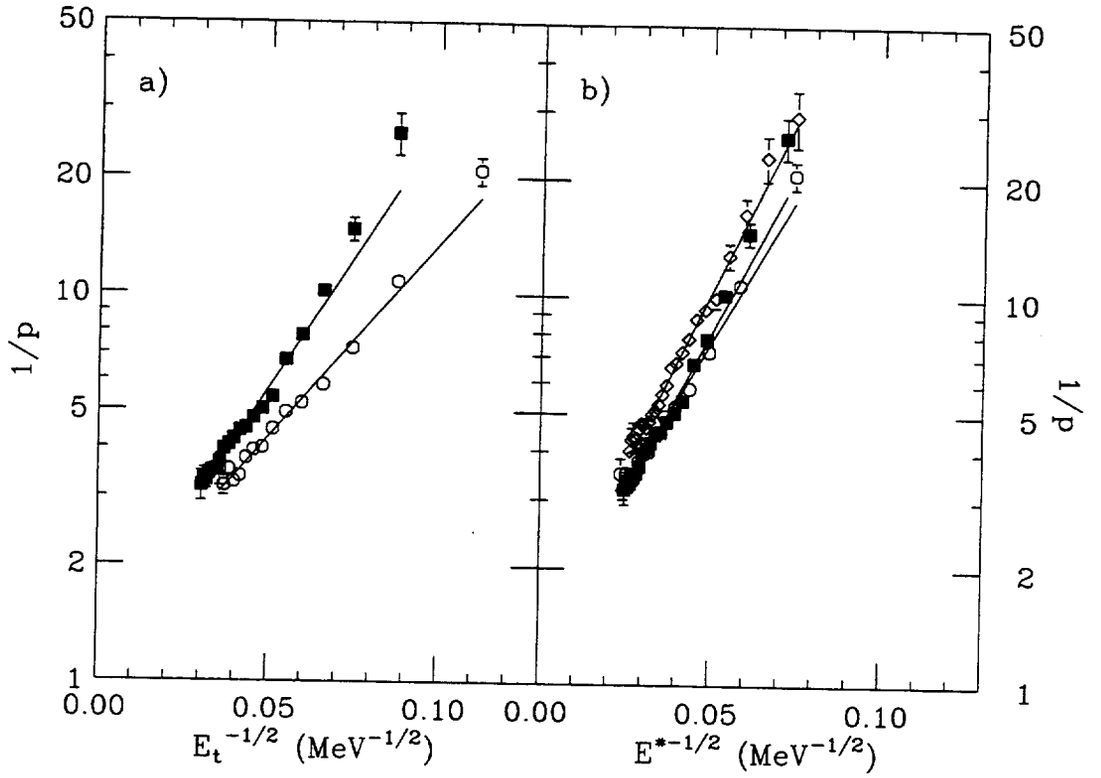

Fig. 48. Arrhenius plot from the simulated binomial decay of a ^{197}Au source. Panel (a): Squares: E_t-Arrhenius plot. Circles: E_t-Arrhenius plot with E_t from charged particles only. Solid lines: straight line fits to the plots. Panel (b): Diamonds: E^*-Arrhenius plot. Squares: rescaled x-axis E_t-Arrhenius plot. Circles: rescaled x-axis E_t-Arrhenius plot, E_t from charged particles only. Solid lines: straight line fits to the plots.

Events with a given E_t come from a rather narrow distribution of E^*. Distortions to the linearity of an Arrhenius plot (from using E_t instead of E^*) are small. For a typical ^{197}Au source simulation event, in the excitation energy range 500 - 1000 MeV, about 40% of E_t is contributed by neutrons, 50% by light charged particles and only 10% by IMFs. The IMFs' contribution drops to less than 5% at excitation energies below 250 MeV and rises to 20% at excitation energies larger than 1250 MeV. These values demonstrate that the IMFs, whose emission probabilities we want to study, do not contribute significantly to the running variable E_t in the simulation. Therefore fluctuations in the number of IMFs do not affect the total E_t. The accuracy of the barrier extracted from the slope of the rescaled E_t-Arrhenius plot, improves when the analysis is repeated for progressively increasing values of the lower threshold $Z_{\rm th}$ in the IMF definition (as in Sec. 4.8.1). When the IMF definition is restricted to $7 \leq Z_{\rm IMF} \leq 20$, the IMFs' contribution to E_t drops to less than 2% and the value of the input barrier can be recovered from the slope of the Arrhenius plot to within 2% of the input value.

8.4 *Efficiency effects*

The above discussion demonstrates that E_t can serve as a useful observable for the measurement of E^* in multifragmentation studies. In particular, the mean and variance of the N_{IMF} distribution are reasonably well preserved, even when the measurement of E_t is imperfect and limited by detection efficiency. This gives us confidence that the experimentally observed binomial fragment multiplicity distributions, as a function of E_t, have indeed their origin from parent binomial distributions. However, it is still important to explore the effects of finite detection efficiency on the extraction of the binomial parameters m and p.

After a general discussion on how the results from a binomial decay (in particular the Arrhenius plot) are expected to be affected by a reduced detection acceptance, we shall proceed to study the effects of the specific experimental devices used to collect the data presented in Refs. [30,29,40].

8.4.1 *Geometric efficiency. E^*- and E_t-Arrhenius plots*

The reducibility of the n-fold probabilities to the 1-fold probability through the binomial equation introduces a great simplification in efficiency corrections. In fact, if the physical distribution is binomial, efficiency effects can be accounted for by correcting the binomial parameters p and m [29]. Disregarding details associated with anisotropies, multiple hits, energy thresholds etc., the true binomial probability p is expected to be related to the observed probability $p_{\rm obs}$ by the relationship [29]:

$$p_{\rm obs} = p \cdot \epsilon \tag{109}$$

where ϵ is the geometric efficiency. The number of trials m is independent of the geometric efficiency.

The consequences of a reduced geometric acceptance on the Arrhenius plot are straightforward. Since

$$\log \frac{1}{p_{\rm obs}} = \log \frac{1}{p \cdot \epsilon} = \log \frac{1}{p} + \log \frac{1}{\epsilon}, \tag{110}$$

one expects the Arrhenius plot to remain linear and conserve its slope, but to shift upwards by $\log(1/\epsilon)$. In other words, the extracted barrier for single fragment emission is unchanged by a reduced geometric detection efficiency, while the absolute probability $p_{\rm obs}$ is trivially modified.

In order to test these ideas and to investigate the effects of a finite acceptance on the experimental observables, angular cuts have been applied when counting the number of particles in a simulated binomial decay (Fig. 49).

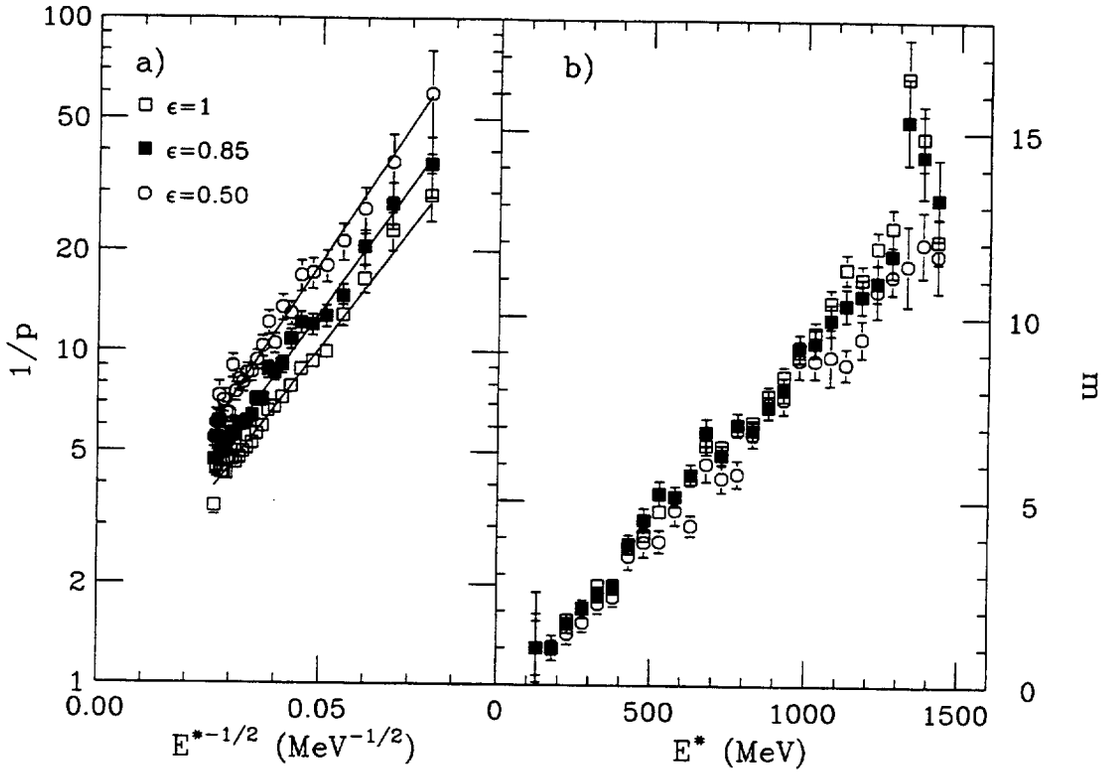

Fig. 49. Binomial decay of a ^{197}Au source with excitation energies and binomial parameters as in Fig. 48. Polar angle cuts $0-45°$ and $0-90°$ are applied, corresponding to geometric efficiencies 0.85 and 0.5 respectively. Panel (a): E^*-Arrhenius plots (solid lines: straight line fits to the plots). Panel (b): Extracted values of the binomial parameter m.

The effect of a reduced geometric efficiency on the E^*-Arrhenius plot is, as expected, an upwards shift of the intercept (panel (a)). The linearity, the slope of the plot, and the physical information on the fragment emission barrier associated with it are preserved. For a given value of the geometric efficiency ϵ, the intercept of the Arrhenius plot is shifted by $\log(1/\epsilon)$, indicating that Eq. (109) is valid as long as the geometric efficiency is independent of the excitation energy. The extracted values of m are not affected by a reduced geometric acceptance (panel (b)).

Experimentally the Arrhenius plot is constructed using E_t as an estimate of the system excitation energy. The effects of a reduced geometric efficiency when the transverse energy is involved are somewhat more complicated, since, by definition (Eq. (18)), the measured value of E_t is correlated with the number of detected fragments. Panel (a) of Fig. 50 shows the E_t-Arrhenius plots produced when angular cuts are applied, thereby reducing the number of detected particles, as well as the measured E_t. One can notice both a shift and a small change in the slope of the straight lines. However, the correct slope of the Arrhenius plot and the information on the emission barrier can still be recovered. A rescaling procedure is suggested by the experimental observation of a linear correlation between the upper limit of the measured transverse energy (E_t^{max}) and the available center of mass energy [30]. From the transverse energy spectra corresponding to progressive angular cuts (panel (c) of Fig. 50), the values

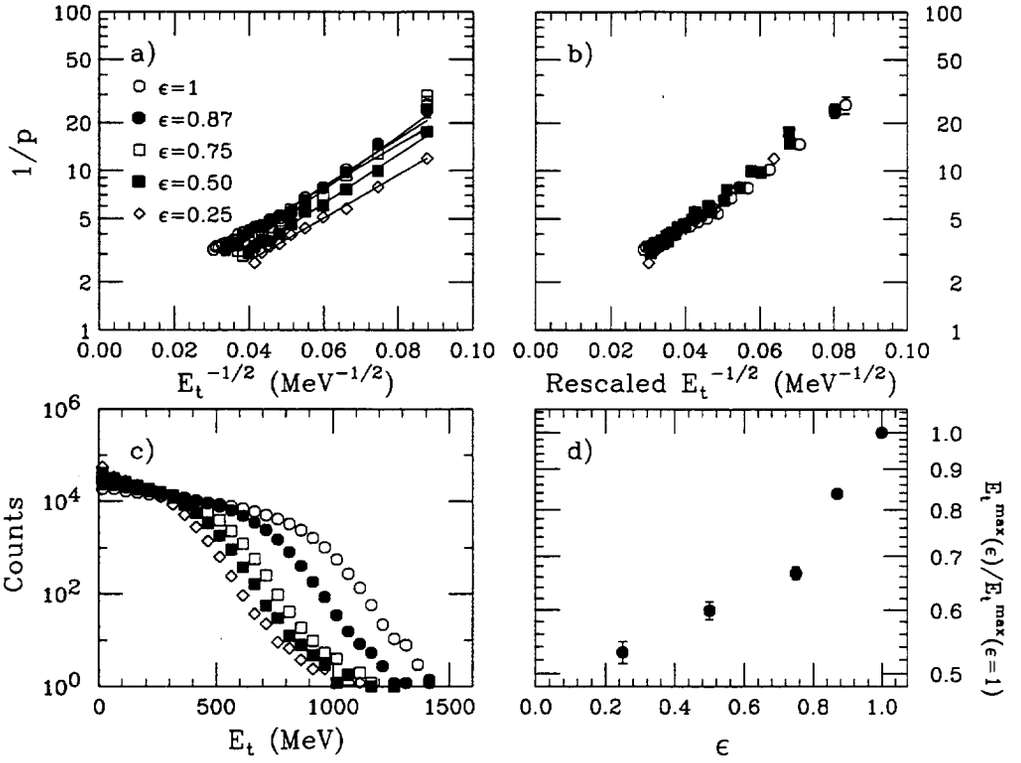

Fig. 50. Binomial decay of a ^{197}Au source with excitation energies and binomial parameters as in Fig. 48. Azimuthal angle cuts (45°, 90°, 180°, 270°) are progressively applied, reducing the number of fragments and the measured transverse energy of the events. Panel (a): E_t-Arrhenius plots. Panel (b): Plots of panel (a) rescaled as explained in the text. Panel (c): E_t spectra. Panel (d): Dependence of E_t^{max} on the geometric efficiency.

of E_t^{max} are deduced (by cutting 0.1% of the total integrated yield at the tail of the distributions) as a function of the geometric efficiency. Panel (d) of Fig. 50 shows these values of $E_t^{max}(\epsilon)$, normalized to $E_t^{max}(\epsilon = 1)$. The x-axes of the E_t-Arrhenius plots are rescaled using this ratio in panel (b) of Fig. 50. The rescaled Arrhenius plots collapse nicely on top of each other, and their slopes correspond to the value of the simulation input barrier if the relationship $E^* = 3/2E_t$ is taken into account.

A similar investigation of the efficiency effects on the Arrhenius plot has been performed with the experimental data of Ref. [30]. The detection efficiency has been artificially reduced by blocking, in software, some of the Miniball detectors according to their azimuthal angles. The results are qualitatively consistent with the simulation, strengthening our confidence in the reducibility approach and in the interpretation of the binomial parameters p and m. However, the extraction of the actual value of the barrier from the experimental data is not possible, since the experimental relationship between the system excitation energy and the measured transverse energy is not exactly known.

8.4.2 Filter response

The experimental data presented in Ref. [30] were collected with a multidetector system covering 89% of 4π, consisting of the MSU Miniball (MB) array [98] and the LBL forward array [99]. Charged particles ($Z = 1 - 20$) emitted in the angular range 16°-160° were detected by 171 fast phoswich MB detectors. Charged particles (Z=1-54) emitted at forward angles (2°-16°) were detected by 16 Si-Si-plastic telescopes of the LBL array. The data of Refs. [29,40] instead were detected with the Miniball only, covering polar angles ranging from 9° to 160°. Representative detection thresholds for the MB and LBL arrays were: 2, 3, 4 MeV/A for Z=3,10,18 and 6, 13, 21, 27 MeV/A for Z=2, 8, 20, 54 respectively. The detector system was transparent to neutrons.

In order to simulate the complete MB-LBL array response, the fragments generated from the binomial simulation were filtered through a software replica of the MB-LBL detection system. Since the simulated particles are emitted in the rest frame of the source, a source velocity was added in order to perform a transformation to the laboratory frame.

After determining which detector (if any) is struck by each of the particles, the program checks for energy thresholds and double hits. Therefore, contributions to the detection inefficiency can originate from geometric misses (either down the beam pipe at polar angles $< 2°$ or in the dead regions between detectors), particles with energies below the detection energy thresholds, and pairs of particles hitting simultaneously the same detector.

Simulations were performed for the decay of a ^{197}Au source (with input parameters $B_Z = (3 \cdot Z)$ MeV, $m_\circ(E^*) = 0.03 \cdot E^*$, $100 \leq E^* \leq 1500$ MeV) at various source velocities. The total efficiency for charged particles depends on the source velocity. A small source velocity causes a slight focusing of the events towards the forward LBL array, thereby increasing the losses due to energy thresholds, since the LBL array thresholds are higher than those of the Miniball. A high source velocity minimizes the energy thresholds problem, but increases geometric losses in the beam pipe (as high as 35% of the total IMF yield), due to the stronger forward focusing. The detection efficiency is also dependent on the multiplicity of the events, because of the increased probability of double hits in the same detector for high multiplicity events, and on the kinetic energies of the particles, through the detection energy thresholds. For these reasons the simulated detection efficiency is dependent on the excitation energy.

The filtered fold probabilities are still binomial and were analyzed with the standard procedures. In Fig. 51 we show two examples of filtered Arrhenius plots. In one case (solid squares, dashed line) a small source velocity increasing linearly with the temperature was added to the particles from a ^{197}Au source decay. When comparing the filtered E^*-Arrhenius plot to the input Arrhenius plot (open diamonds, solid line) one can notice both a shift upwards, as expected when the geometric efficiency is reduced (Eq. (110)) and a tilt softening the slope of the line. This tilt originates

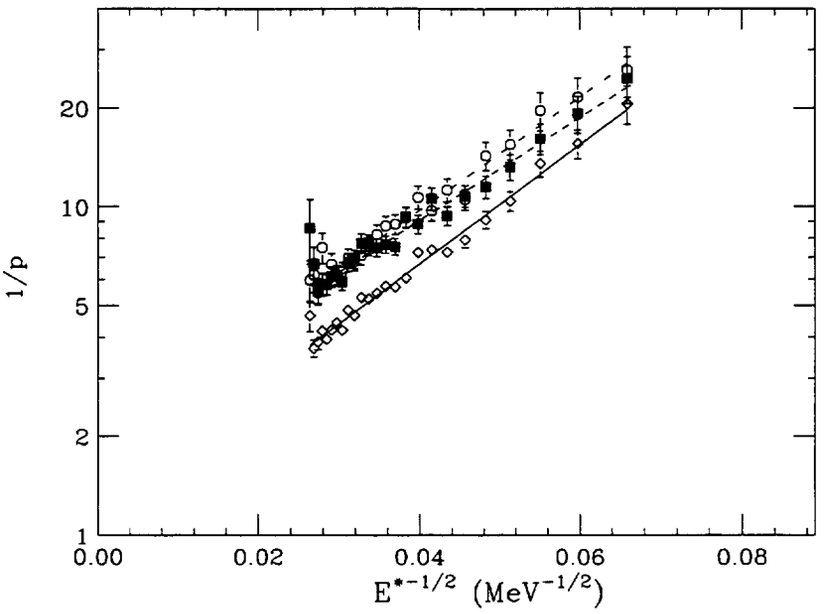

Fig. 51. Binomial decay of a ^{197}Au source with excitation energies and binomial parameters as in Fig. 48. Diamonds: input E^*-Arrhenius plot. Squares: filtered E^*-Arrhenius plot (v_{source} = 0 to 0.07 c). Circles: filtered E^*-Arrhenius plot (v_{source} = 0.2 c to 0.35 c). Lines: straight line fits to the plots.

from the dependence of the efficiency on the excitation energy, as discussed above. In this simulation, the total detection efficiency for IMFs, integrated over the excitation energy, was $\approx$ 75% (10% lower than the efficiency for light charged particles). The input barrier is recovered from the slope of the Arrhenius plot with an uncertainty of 15%.

In the other example of Fig. 51 (open circles, dash-dotted line), the source velocity is higher and decreasing linearly with the nuclear temperature. In this simulation, the total IMF efficiency drops to about 65%, due to high losses of fragments kinematically focused beyond the geometric acceptance. However, the high source velocity minimizes the energy threshold effects and the resulting detection efficiency is rather constant over the entire range of excitation energies. Thus, the input slope is recovered with higher accuracy than in the previous case.

The filter causes a weakening of the correlation between the transverse energy and the excitation energy, due to a mixing of events from different excitation energies corresponding to the same measured value of E_t. When the filtered E_t is used for the Arrhenius plot, the barrier extracted from the slope has large uncertainties. However, it is possible to extract values proportional to the barrier, by increasing the lower Z_{th} threshold in the IMF definition, as discussed in Sec. 4.8.1.

When the filtered E_t is used to produce Arrhenius plots (see Fig. 50), the extrapolated y-intercept is less than one, corresponding to values of p larger than one. This perhaps clarifies the puzzle of too small y-intercepts observed in the experimental Arrhenius

plots (see Figs. 12, 14, and 18), since one would expect the elementary probability to approach unity in the limit of infinite temperature (see Eq. (30)).

8.5 Summary

We have implemented binomial and Poisson decay simulations to address a number of issues connected with the experimental multifragmentation studies presented in Part A. For the binomial simulation, we have assumed that the n-fragment emission probability P_n is distributed according to the binomial distribution, and that multifragmentation is empirically reducible to a combination of nearly independent fragment emissions. Moreover, we have assumed a thermal dependence of the elementary emission probability p on the nuclear temperature.

By processing the simulated events we have tested the standard procedures utilized in the experimental data analysis. We have also verified that the simulation input can be recovered without significant loss of information, and determined how the final results reflect different input conditions.

The simulation results strengthen the validity of the reducibility approach presented in Sec. 4 and the physical meaning of quantities such as the elementary probability p. Reducibility is a valid approach even when multiple sources of fragment emission are created in the collision, especially if one of the sources is dominant.

The Arrhenius plot is a powerful tool to explore the thermal features of the elementary probability p, even though the determination of the actual fragment emission barrier B, proportional to the slope of the plot, can be hampered by the presence of source residues and by small size effects.

Introducing the total transverse kinetic energy as an estimate of the system excitation energy does not alter these results, since, in our simulation, the transverse energy E_t is linearly correlated with the system excitation energy. This is true also if the transverse energy is calculated from charged particles only, excluding the neutron contribution. Moreover, the transverse energy is weakly correlated with the IMF multiplicity, hence the observed features of binomiality and thermal scaling can not be generated by this weak auto-correlation of E_t.

We have tested the effects of a reduced geometric efficiency as well as the effects of a software replica of the detection device. We have shown that a reduced geometric efficiency preserves binomiality and that efficiency corrections can be applied through the binomial parameters p and m. We have explored the effects of a finite detection acceptance on the Arrhenius plot and have shown that when the geometric acceptance is reduced, it is still possible to recover the binomial input without significant loss of information. However, the introduction of an energy dependent efficiency, coupled with the use of E_t as a measure of the excitation energy, complicates the problem

so that only values *proportional* to the effective barrier for fragment emission can be extracted from experimental Arrhenius plots.

Finally, we have also shown that, in a binomial decay scenario, the n-fold charge distributions are reducible to the 1-fold, consistently with the experimental findings of Refs. [40,41]. In the binomial simulation, the n-fold charge distributions are independent of the fold number n as long as a sizeable remnant survives as a reservoir of mass, charge and excitation energy. A dependency on n arises when the entire system is consumed.

In summary, the results of the binomial decay simulations have made us more confident that the experimental procedures utilized in Sec. 4 are correct and that the empirical findings of reducibility and thermal scaling in multifragmentation are not artifacts of incomplete detection efficiency nor are they generated by the auto-correlation of the variable used to estimate the excitation energy.

9 Conclusions

The picture of multifragmentation, as it appears in the pages above, is still sketchy and incomplete. However, we believe we have succeeded in unveiling important features which may be the key to deeper understanding.

The pervasive aspect of *reducibility* indicates that, whatever the mechanism, the fragments are emitted essentially independent of one another. Thus we have shown that the probability P_n of emitting n fragments can be reduced to the probability of emitting a single fragment through the binomial equation. Similarly the n fragment charge distributions can be reduced to the one fragment charge distribution. Furthermore, the particle-particle angular correlation can be reduced to the individual particle angular distributions.

In all the above quantities, reducibility is somehow restricted by what we may call "dynamical constraints". For the emission probabilities, the constraint is the binomial parameter m, indicative either of a dynamical time window, or of the finite source size.

For the charge distributions, reducibility is restricted by the parameter c, which seems to indicate some special way of enforcing charge conservation. We speculated that its transition from near zero to a finite value with increasing energy could be an indication of a transition from phase coexistence (liquid-vapor) to single phase (vapor).

Finally, the angular correlations violate reducibility at small relative angle where particle-particle interactions become manifest.

These broad features of reducibility speak to the near independence of fragment

emission but not to its mechanism.

Thermal scaling instead makes a clear statement about the fact that the elementary probabilities entering in the n fragment emission probabilities, the n fragment charge distributions, and the two fragment angular correlations are *thermal*. In other words, these probabilities have the form of a Boltzmann factor and clearly portray its characteristic energy dependence (Arrhenius plots).

Thus the resulting picture is tantalizingly close, but not quite that of a compound nucleus emission. Apparently sources are dynamically generated which, within dynamical constraints of time and size, emit fragments in a thermal manner. Among the potential fruits that can be reaped from the pursuit of the analysis outlined so far are dynamical features of source formation, size and lifetime, as well as static features like barriers and source sizes and densities.

Appendix

A Z_{th} effect on the extraction of c

In the analysis of charge distributions (see Secs. 5.1 and 6.4), the scaling factor e^{-cnZ} used to account for the n dependence of the charge distributions was shown to arise naturally in the charge distribution obtained by the least biased breaking of an integer Z_o into n integers (Euler's problem): $P(Z) = cn^2e^{-cnZ}$ (Eq. (52)). In the context of the charge distribution, n is the IMF multiplicity which depends on the lowest threshold Z_{th} adopted. However, in the context of Euler's problem, n is the *total* number of integers. This raises the question of whether Z_{th} should be lowered to include light charged particles.

Experimentally, it is difficult to isolate and eliminate the pre–equilibrium contribution associated with light charged particle emission. This contamination overestimates the value of n associated with the number of particles emitted from the thermally equilibrated source, and it also distorts the shape of the charge distribution for the light charged particles. To reduce the effect of pre-equilibrium contamination, we have instead studied the charge distributions of intermediate mass fragments ($Z_{th} \leq Z \leq 20$) as a function of fragment multiplicity (N_{IMF}). The value of n in e^{-cnZ} then became N_{IMF}, and c was extracted by fitting the charge distributions of IMFs with $e^{-cN_{IMF}Z}$. If c_o is the value of c extracted from the charge distributions of all particles, it can be related to c by their common exponential fit parameters:

$$c_o \cdot n = c \cdot N_{IMF}. \tag{A.1}$$

This equation simply says that c extracted experimentally from the charge distributions of IMFs is different from c_o, since $n \neq N_{IMF}$ when a constraint is imposed on the partitioning of the source by setting a lower Z_{th} in the IMF definition. In fact, this was one of the reasons for the discrepancy between $1/Z_0$ and the value of c extracted from the percolation data. In this section, we study and account for the effect of Z_{th} on the extraction of c in order to obtain a value for c_o.

If the charge distribution $P_n(Z)$ of a given particle multiplicity n is normalized such that the total area under the curve $P_n(Z)$ is equal to n, then the number of fragments (N_{IMF}) is simply the integrated area bounded by $Z = Z_{th}$ and $Z = 20$. In other words, N_{IMF} can be calculated from n by integrating the charge distribution of Eq. (52) from $Z = Z_{th}$ to 20:

$$N_{IMF} = \int_{Z_{th}}^{20} c_o n^2 e^{-c_o nZ} dZ = n\left[e^{-c_o nZ_{th}} - e^{-c_o n(20)}\right]. \tag{A.2}$$

The exponential dependence on Z_{th} in the above equation suggests that it can be simplified if we restrict ourselves to values of Z_{th} that are much smaller than 20.

Under this condition, the above integral becomes independent of the upper limit of the IMF definition:

$$N_{IMF} \simeq \int_{Z_{th}}^{\infty} c_o n^2 e^{-c_o n Z} dZ = n e^{-c_o n Z_{th}}. \tag{A.3}$$

The above expression shows that N_{IMF} is related to n with a strong dependence on the lower Z_{th} of the IMF definition. In the limit of small Z_{th}, the exponential term of Eq. (A.3) approaches one and N_{IMF} approaches the value of n. However, as Z_{th} increases, N_{IMF} becomes less than n and this deviation becomes progressively larger.

Since N_{IMF} can be determined experimentally, it would be more useful to express n in terms of N_{IMF}. An approximation by a Taylor expansion of Eq. (A.3) up to second order yields the following expression:

$$n(N_{IMF}) = N_{IMF} + c_o Z_{th} N_{IMF}^2 + 1.5(c_o Z_{th})^2 N_{IMF}^3. \tag{A.4}$$

To study the effect of Z_{th} on the extraction of c, the variable n in Eq. (A.1) is expressed in terms of N_{IMF} according to Eq. (A.4):

$$\begin{aligned} c \cdot N_{IMF} &= c_o \cdot \left[N_{IMF} + c_o Z_{th} N_{IMF}^2 + 1.5(c_o Z_{th})^2 N_{IMF}^3 \right] \\ c &= c_o \cdot \left[1 + c_o Z_{th} N_{IMF} + 1.5(c_o Z_{th} N_{IMF})^2 \right]. \end{aligned} \tag{A.5}$$

The above equation clearly indicates that an N_{IMF} dependence is introduced into the quantity c by setting a lower Z_{th} in the definition of IMF. The resulting value of c will always be larger than c_o, and this deviation increases with increasing values of N_{IMF} and Z_{th}. To verify these ideas experimentally, we have extracted c by the χ^2 method from the charge distributions associated with different values of N_{IMF} and Z_{th}. These extracted values of c are plotted in Fig. A.1 as a function of E_t for the reaction ^{129}Xe + ^{197}Au at a bombarding energy of $E/A = 60$ MeV. In the top panel, we have extracted average values of c over several consecutive fragment multiplicities in order to minimize statistical uncertainties. Clearly, the extracted values of c associated with events of higher fragment multiplicity are larger at all values of E_t. In the bottom panel, the average value of c (over all fragment multiplicities), is found to increase with increasing Z_{th}. These results demonstrate the expected N_{IMF} and Z_{th} dependence of c.

In an attempt to eliminate the N_{IMF} dependence of c in order to extract c_o, we have expressed n of e^{-cnZ} in terms of N_{IMF} and Z_{th} following Eq. (A.4). The reduced quantity $F(Z)$ of Eq. (43) then becomes:

$$F(Z) = [\ln P_{N_{IMF}}(Z) + c_o n(N_{IMF}) Z] \sqrt{E_t}, \tag{A.6}$$

where the variable c is replaced with c_o since the Z_{th} effect has been properly considered in the expression of n. A χ^2 is then constructed with this new functional form

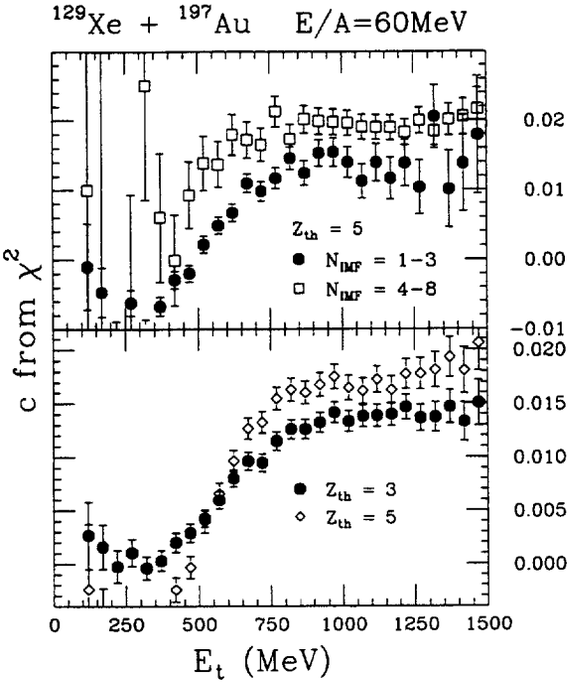

Fig. A.1. The coefficient c extracted by the χ^2 method as a function of E_t for the reaction ^{129}Xe + ^{197}Au at a bombarding energy of $E/A = 60$ MeV. Values of c are extracted from the charge distributions associated with indicated values of N_{IMF} (top panel) and Z_{th} (bottom panel).

and c_o can be extracted using the same procedure. The top panel of Figure A.2 shows that c_o is now independent of the various N_{IMF} cuts over a large range of measured E_t. However, a slight increase in c_o with increasing Z_{th} is observed in the bottom panel indicating that the effect of Z_{th} has not been completely accounted for. This residual Z_{th} dependence may be related to the Z dependence of the detection efficiency in our experimental device which has not been accounted for. It is well known that the detection thresholds for the MSU Miniball phoswich array [98] and the LBL silicon array [99] depend strongly on the charge of the incident particles detected experimentally.

We notice that the extracted values of c remain constant over a large range of E_t in Figure A.2. Therefore, it may be statistically feasible to extract values of c associated with individual N_{IMF} if we bin together events of different E_t in this saturation region. For example, events with E_t ranged from 800 to 1500 MeV are binned together to extract c using the χ^2 method. The diamonds in Figure A.3 show the expected N_{IMF} dependence of c for $Z_{th} = 3$ (upper) and 5 (lower) as well. The result also illustrates the Z_{th} dependence, since the extracted value of c is always larger for $Z_{th} = 5$ at a given N_{IMF}. However, when n is expressed in terms of N_{IMF} following Eq. (A.4) in the χ^2 construction, the above N_{IMF} dependence is eliminated as shown by the circles in Figure A.3. The circles scatter around the weighted average (dashed lines) of $c_o = 0.081 \pm 0.0016$ and 0.0098 ± 0.0015 for $Z_{th} = 3$ and 5 respectively. Similarly, the discrepancy in the values of c_o for two different Z_{th} may be due to other residual

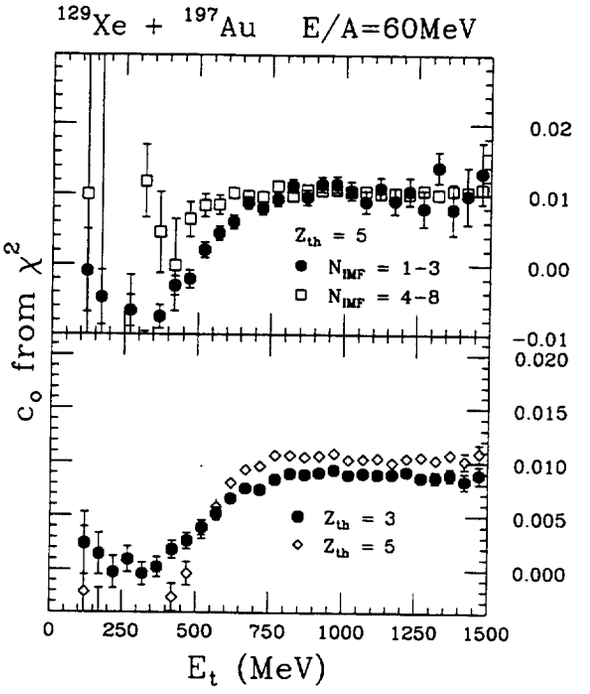

Fig. A.2. The coefficient c_o extracted by the χ^2 method as a function of E_t for ^{129}Xe + ^{197}Au reaction at a bombarding energy of $E/A = 60$ MeV. In this extraction, n is expressed in terms of N_{IMF} using Eq. (A.4). Values of c_o are extracted from the charge distributions associated with the indicated values of N_{IMF} (top panel) and Z_{th} (bottom panel).

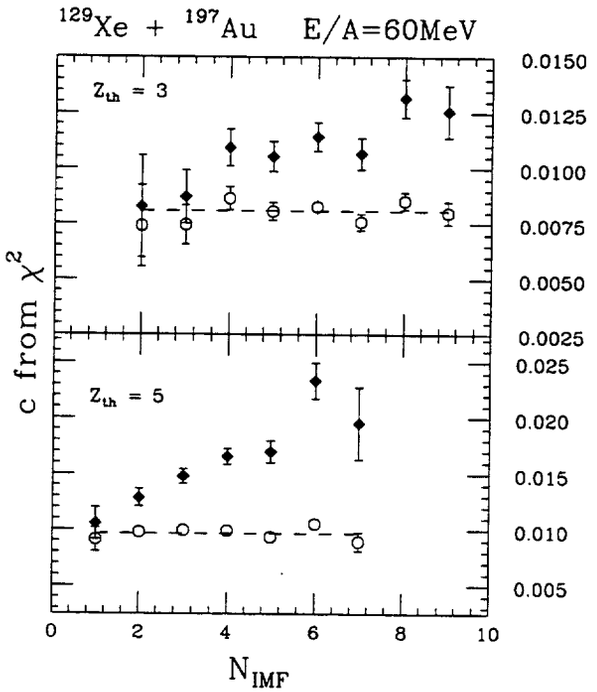

Fig. A.3. The coefficients c (diamonds) and c_o (circles) extracted by the χ^2 method as a function of N_{IMF} for charge distributions of $Z_{th} = 3$ (top panel) and $Z_{th} = 5$ (bottom panel).

effects that have not been considered.

Thus far, we have investigated in detail the fragment multiplicity (N_{IMF}) dependence of the charge distributions in the reaction ^{129}Xe + ^{197}Au at a bombarding energy of E/A = 60 MeV. The empirically observed N_{IMF} dependence of c is shown to be related to the lower Z_{th} of the IMF definition. To account for the effect of Z_{th}, the number of partitioned fragments n in Euler's problem is expressed in terms of the experimental fragment multiplicity defined by Z_{th}. A constant value of c_o is then extracted independent of the fragment multiplicity. This correction for the effect of Z_{th} may help to relate the value of c_o extracted from the experiment to the size of the emission source.

Acknowledgements

This work was supported by the Director, Office of Energy Research, Office of High Energy and Nuclear Physics, Nuclear Physics Division of the US Department of Energy, under contract DE-AC03-76SF00098 and by the National Science Foundation under Grant Nos. PHY-8913815, PHY-90117077, and PHY-9214992.

References

[1] D.H.E. Gross, Rep. Prog. Phys. **53**, 605 (1990).

[2] B. Borderie, Ann. de Phys. **17**, 349 (1992).

[3] L.G. Moretto and G.J. Wozniak, Ann. Rev. of Nucl. & Part. Sci., **43**, 379 (1993).

[4] H. Fuchs and K. Möhring, Rep. Prog. Phys. **57**, 231 (1994).

[5] J.P. Bondorf *et al.*, Phys. Reports **257**, 133 (1995).

[6] A. Meibom and I. Balslev, Phys. Rev. Lett. **76**, 2492 (1996).

[7] M. Daoud, Proc. of the Workshop on Fragmentation Phenomena, (Les Houches 1993), pp. 94, ed. D. Beysens, X. Campi and E. Pefferkorn (New Jersey: World Scientific).

[8] C. Frances *et al.*, Proc. of the Workshop on Fragmentation Phenomena, (Les Houches 1993), pp. 3, ed. D. Beysens, X. Campi and E. Pefferkorn (New Jersey: World Scientific).

[9] E.V. Ryan *et al.*, Icarus **94**, 283 (1991).

[10] R.D. Cohen, Proc. R. Soc. London **435**, 483 (1991).

[11] P.J. Siemens, Nature **305**, 410 (1983).

[12] Lord Rayleigh, article 58, "Scientific Papers", Dover Publication, Inc., New York, p. 361 (1964).

[13] L.G. Moretto, Kin Tso, N. Colonna, and G.J. Wozniak, Phys. Rev. Lett. **69**, 1884 (1992).

[14] R.J. Charity *et al.*, Nuc. Phys. A **483**, 371 (1988).

[15] L.G. Moretto *et al.*, Phys. Rev. Lett. **71**, 3935 (1993).

[16] N. Colonna *et al.*, Phys. Rev. Lett. **62**, 1833 (1989).

[17] Y. Blumenfeld *et al.*, Phys. Rev. Lett. **66**, 576 (1991).

[18] D.R. Bowman *et al.*, Phys. Rev. **C46**, 1834 (1992).

[19] J. Hubele *et al.*, Phys. Rev. C **46**, R1577 (1992).

[20] A. Schüttauf *et al.*, Nucl. Phys. A (in press).

[21] L.G. Moretto and J. Huizenga, Ann. Rev. of Nucl. Sci. **22**, 427 (1972) and Refs. therein.

[22] L.G. Moretto *et al.*, Phys. Rev. Lett. **75**, 4186 (1995).

[23] L.G. Moretto, K.X. Jing and G.J. Wozniak, Phys. Rev. Lett. **74**, 3557 (1995).

[24] L.G. Moretto *et al.*, Phys. Rev. **179**, 1176 (1969).

[25] K.J. Laidler, Journal of Chemical Education **49**, 343 (1972).

[26] J.A. Lopez and J. Randrup, Nucl. Phys. A **503**, 183 (1989).

[27] J.A. Lopez and J. Randrup, Nucl. Phys. A **512**, 345 (1990).

[28] K. Tso, Ph. D. Thesis, **LBNL-38884**, University of California at Berkeley (1996).

[29] L.G. Moretto *et al.*, Phys. Rev. Lett. **74**, 1530 (1995).

[30] K. Tso *et al.*, Phys. Lett. B **361**, 25 (1995).

[31] P. Roussel-Chomaz *et al.*, Nucl. Phys. **A551**, 508 (1993).

[32] L.G. Moretto and G.J. Wozniak, Prog. Part. & Nucl. Phys. **21**, 401 (1988) and Refs. therein.

[33] R.J. Charity *et al.*, Nucl. Phys. A **511**, 59 (1990).

[34] D. Fox *et al.*, Phys. Rev. C **47**, R421 (1993).

[35] D. Bowman *et al.*, Phys. Rev. Lett. **70**, 3534 (1993).

[36] E. Bauge *et al.*, Phys. Rev. Lett. **70**, 3705 (1993).

[37] D. Durand *et al.*, Phys. Lett. B **345**, 397 (1995).

[38] W.A. Friedman, Phys. Rev. C **42**, 667 (1990).

[39] Y.D. Kim *et al.*, Phys. Rev. **C45**, 338 (1992).

[40] L. Phair *et al.*, Phys. Rev. Lett. **75**, 213 (1995).

[41] A. Ferrero *et al.*, Phys. Rev. C **53**, R5 (1996).

[42] L.G. Sobotka and L.G. Moretto, Phys. Rev. **C31**, 668 (1985).

[43] J. Pochodzalla *et al.*, Phys. Rev. C **35**, 1695 (1987).

[44] F. Zhu *et al.*, Phys. Lett. B **282**, 299 (1992).

[45] D.J. Morrissey, W. Benenson and W.A. Friedman, Annu. Rev. Nucl. Part. Sci **44**, 27 (1994) and Refs. therein.

[46] B.V. Jacak *et al.*, Phys. Rev. Lett. **51**, 1846 (1983).

[47] J.E. Finn *et al.*, Phys. Rev. Lett. **49**, 1321 (1982).

[48] R.W. Minich *et al.*, Phys. Lett. B **118**, 458 (1982).

[49] C.B. Chitwood *et al.*, Phys. Lett. B **131**, 289 (1983).

[50] A.D. Panagiotou *et al.*, Phys. Rev. Lett. **52**, 496 (1984).

[51] A. Bujak *et al.*, Phys. Rev. C **32**, 620 (1985).

[52] W.G. Lynch, Ann. Rev. Nucl. Part. Sci. **37**, 493 (1987).

[53] M. E. Fischer, Rep. Prog. Phys. **67**, 615 (1967).

[54] M. L. Gilkes *et al.*, Phys. Rev. Lett. **73**, 1590 (1994).

[55] J. Pochodzalla *et al.*, Phys. Rev. Lett. **75**, 1040 (1995).

[56] S. Albergo *et al.*, Nuovo Cimento A **89**, 1 (1985).

[57] J. Natowitz *et al.*, Phys. Rev. C **52**, R2322 (1995).

[58] M.B. Tsang *et al.*, Phys. Rev. C **53**, R1057 (1996).

[59] X. Campi, H. Krivine and E. Plagnol, Phys. Lett. B, in press.

[60] L.G. Moretto *et al.*, Phys. Rev. Lett. **76**, 2822 (1996).

[61] L.G. Moretto, L. Phair, G.J. Wozniak, to appear in *Proceedings of the 1st Catania Relativistic Ion Studies: Critical Phenomena and Collective Observables*, Acicastello, May 27-31, 1996, LBL-39105.

[62] L.G. Moretto *et al.*, Phys. Rev. Lett. **76**, 372 (1996).

[63] R. Ghetti *et al.*, to be published, LBL-39196.

[64] W. Bauer, Phys. Rev. **C38**, 1297 (1988).

[65] V.M. Strutinskii, Sov. Phys. JETP **13**, 1261 (1961).

[66] S.M. Vydrug-Vlasenko, V.F. Zavarzin and S. Yu. Kun, Sov. J. Nucl. Phys. **41**, 394 (1985).

[67] M.B. Tsang *et al.*, Phys. Lett. B **148**, 265 (1984).

[68] C.B. Chitwood *et al.*, Phys. Rev. C **34**, 858 (1986).

[69] D.J. Fields *et al.*, Phys. Rev. C **34**, 536 (1986).

[70] M.B. Tsang *et al.*, Phys. Rev. C **42**, R15 (1990).

[71] D. Ardouin *et al.*, Nucl. Phys. **A514**, 564 (1990).

[72] S. Wang *et al.*, Phys. Rev. C **44**, 1091 (1991).

[73] L. Phair *et al.*, Nucl. Phys. **A564**, 453 (1993).

[74] R.A. Lacey *et al.*, Phys. Rev. Lett. **70**, 1224 (1993).

[75] This software threshold is sufficiently low to integrate nearly all of the measured energy spectra. For larger thresholds (up to 5 MeV), the stated conclusions remain unchanged but the azimuthal anisotropies become more pronounced.

[76] L.G. Moretto, Nucl. Phys. **A242**, 211 (1975) and Refs. therein.

[77] M.B. Tsang *et al.*, Phys. Rev. C **44**, 2065 (1991).

[78] J. Lauret *et al.*, Phys. Lett. B **339**, 22 (1994).

[79] T. Ethvignot, *et al.*, Phys. Rev. C **48**, 618 (1993).

[80] M.B. Tsang *et al.*, Phys. Rev. Lett. **52**, 1967 (1984).

[81] M.B. Tsang *et al.*, Phys. Rev. Lett. **57**, 559 (1986).

[82] M.B. Tsang *et al.*, Phys. Rev. Lett. **60**, 1479 (1988).

[83] W.K. Wilson *et al.*, Phys. Rev. C **41**, R1881 (1990).

[84] Note that the observed mass scaling is *independent* of the thermal scaling observed in Fig. 34. We merely use the linear slopes there to simplify our analysis of the mass scaling.

[85] U. Brosa, S. Grossmann, A. Müller and E. Becker, Nucl. Phys. **A502**, 423c (1989).

[86] U. Brosa, S. Grossmann, and A. Müller, Phys. Rep. **197**, 167 (1990).

[87] P. Chomaz, M. Colonna, A. Guarnera, B. Jacquot, Nucl. Phys. **A583**, c305 (1995).

[88] A.S. Botvina and D.H.E. Gross, Phys. Lett. **B344**, 6 (1995).

[89] L. Phair *et al.*, Nucl. Phys. **A548**, 489 (1992).

[90] L.G. Moretto *et al.*, LBL Annual Report **LBL-35768**, 89 (1993).

[91] R.J. Charity *et al.*, Nucl. Phys. **A476**, 516 (1988).

[92] W.D. Myers, Nucl. Phys. **A204**, 465 (1973).

[93] C.P. Montoya *et al.*, Phys. Rev. Lett. **73**, 3070 (1994).

[94] A. Del Zoppo *et al.*, Phys. Rev. Lett. **75**, 2288 (1995).

[95] W. Skulski *et al.*, Nuclear Chemistry Progress Report, August 1995, Univ. of Rochester, DOE/ER/40414-8, p. 75.

[96] A. Giovannini and L. Van Hove, Z. Phys. C, **30**, 391 (1986).

[97] C. Cavata *et al.*, Phys. Rev. **C24**, 1760 (1990).

[98] R.T. De Souza *et al.*, Nucl. Inst. Meth. **A295**, 109 (1990).

[99] W.L. Kehoe *et al.*, Nucl. Inst. Meth. **A311**, 258 (1992).